

**DOCTORAL THESIS**

# Growth and Optical Properties of Two-Dimensional Transition Metal Dichalcogenides

Reelika Kaupmees

TALLINN UNIVERSITY OF TECHNOLOGY  
DOCTORAL THESIS  
25/2021

# **Growth and Optical Properties of Two-Dimensional Transition Metal Dichalcogenides**

REELIKA KAUPMEES



TALLINN UNIVERSITY OF TECHNOLOGY

School of Engineering

Department of Materials and Environmental Technology

This dissertation was accepted for the defence of the degree 23/04/2021

**Supervisor:**

Dr. Jüri Krustok, Professor  
Division of Physics  
Tallinn University of Technology  
Tallinn, Estonia

**Co-supervisor:**

Dr. Maarja Grossberg, Professor  
Department of Materials and Environmental  
Technology Tallinn University of Technology  
Tallinn, Estonia

**Opponents:**

Dr. Levent Gütay, Senior Scientist  
Institute of Physics  
Carl von Ossietzky University of Oldenburg  
Oldenburg, Germany

Dr. Toomas Rõõm, Research Professor  
National Institute of Chemical Physics and Biophysics  
Tallinn, Estonia

**Defence of the thesis:** 11/06/2021, Tallinn

**Declaration:**

Hereby I declare that this doctoral thesis, my original investigation and achievement, submitted for the doctoral degree at Tallinn University of Technology has not been submitted for doctoral or equivalent academic degree.

Reelika Kaupmees

-----  
signature



European Union  
European Regional  
Development Fund



Investing  
in your future

Copyright: Reelika Kaupmees, 2021

ISSN 2585-6898 (publication)

ISBN 978-9949-83-695-6 (publication)

ISSN 2585-6901 (PDF)

ISBN 978-9949-83-696-3 (PDF)

Printed by Spin Press

TALLINNA TEHNIKAÜLIKOO  
DOKTORITÖÖ  
25/2021

# **Kahedimensionaalsete siirdemetallide dikalkogeniidide kasvatus ning optiliste omaduste uurimine**

REELIKA KAUPMEES





# Contents

List of Publications .....	6
Author's Contribution to the Publications .....	7
Introduction .....	8
Abbreviations, Terms and Symbols.....	10
1 Literature review.....	11
1.1 General properties .....	15
1.1.1 Molybdenum disulfide – MoS <sub>2</sub> .....	15
1.1.2 Tungsten disulfide – WS <sub>2</sub> .....	16
1.2 Aging of TMD.....	17
1.3 TMD properties at low temperatures .....	17
1.4 TMD properties at high temperatures .....	17
1.5 Summary of literature review and aim of the study .....	18
2 Experimental .....	20
2.1 Chemical vapor deposition of TMD monolayers.....	20
2.1.1 CVD of WS <sub>2</sub> monolayer.....	20
2.1.2 CVD of MoS <sub>2</sub> monolayer.....	21
2.2 Characterization .....	21
3 Results and discussion.....	23
3.1 Photoluminescence study of B-Trions in MoS <sub>2</sub> monolayers with high density of defects.....	23
3.2 Local strain-induced band gap fluctuations and exciton localization in aged WS <sub>2</sub> monolayers .....	27
3.3 Tailoring of bound exciton photoluminescence emission in WS <sub>2</sub> monolayer .....	35
3.4 The effect of elevated temperatures on excitonic emission and degradation processes of WS <sub>2</sub> monolayer .....	40
Conclusion.....	47
References .....	48
Acknowledgements.....	59
Abstract.....	60
Lühikokkuvõte.....	62
Appendix .....	65
Curriculum vitae.....	105
Elulookirjeldus.....	108

## List of Publications

The list of author's publications, on the basis of which the thesis has been prepared:

- I Krustok, J., **Kaupmees, R.**, Jaaniso, R., Kiisk, V., Sildos, I., Li, B., Gong, Y. (2017). Local strain-induced band gap fluctuations and exciton localization in aged WS<sub>2</sub> monolayers. *AIP Advances*, 7, 065005
- II **Kaupmees, R.**, Komsa, H.-P., Krustok, J. (2019). Photoluminescence study of B-trions in MoS<sub>2</sub> monolayers with high density of defects. *Physica Status Solidi B*, 256, 1800384
- III **Kaupmees, R.**, Grossberg, M., Ney, M., Asaithambi, A., Lorke, A., Krustok, J. (2020). Tailoring of bound exciton photoluminescence emission in WS<sub>2</sub> monolayers. *Physica Status Solidi (RRL)*, 14, 1900355
- IV **Kaupmees, R.**, Walke, P., Madauß, L., Maas, A., Pollmann, E., Schleberger, M., Grossberg, M., Krustok, J. (2020). The effect of elevated temperatures on excitonic emission and degradation processes of WS<sub>2</sub> monolayers. *Physical Chemistry Chemistry Physics*, 22, 22609

The copies of the papers are included in Appendix.

## **Author's Contribution to the Publications**

Contribution to the papers in this thesis are:

- I Characterization of  $WS_2$  monolayer by low temperature photoluminescence and Raman spectroscopy, analysis of the results, and minor part of the writing
- II Chemical vapor deposition of  $MoS_2$  monolayer, characterization of the monolayer by photoluminescence and Raman spectroscopy, analysis of the results, and major part of the writing
- III Chemical vapor deposition of  $WS_2$  monolayer, part of characterization of the monolayer by photoluminescence and Raman spectroscopy, analysis of the results, and major part of the writing
- IV Characterization of the  $WS_2$  monolayer by Raman, high temperature photoluminescence, analysis of the results and major part of writing.



## Introduction

Two-dimensional (2D) materials have been attracting researchers interest from 2004, when the first graphene monolayer was isolated [1]. Since then, numerous other 2D materials have been discovered, a large and interesting 2D material family of transition metal dichalcogenides (TMDs) among them. One of the pioneers and most well-studied monolayered TMD is MoS<sub>2</sub>, however, also WS<sub>2</sub> monolayer has recently gathered a lot of attention. Monolayered TMDs are semiconductors with direct band gap in the visible or near infrared spectral range, while the thickness of these monolayers is less than a nanometer [2]. These materials have many desirable properties for future flexible optoelectronic and electronic applications.

One exceptional aspect about TMDs is the excitonic emission, that is observable at room temperature and even above, due to the high exciton binding energy  $E_B$  [3], [4]. TMDs can be characterized by two excitonic bands (A- and B-band), due to the spin-orbit coupling of the valence band. Moreover, these exciton bands involve different types of excitons including neutral excitons, trions, and biexcitons [5].

There are many different methods to obtain monolayered TMDs. One of the most popular is chemical vapor deposition (CVD), which has been used to produce large areas (recent results are around from 500  $\mu\text{m}$  to 2.5 mm) of TMD monolayers with high quality [6]–[8]. Large areas of TMD are important for applications, however, these areas have to also be of high quality, homogeneous, and stable under operating conditions. It is important to note that most optoelectronic devices operate at higher temperatures than room temperature.

Therefore, before these materials can be used in future electronics and optoelectronics, many issues must be addressed, such as the growth of homogeneous and large area monolayers, electrical and optical properties at various conditions including different temperatures and different excitation powers. Moreover, the stability of the materials in ambient and working conditions is an important factor. Although MoS<sub>2</sub> and WS<sub>2</sub> have been studied thoroughly with various spectroscopy methods, these have mostly been conducted on fresh and good quality samples. It is not well known how high concentration of defects or aging affects the optoelectronic properties of TMDs.

The aim of this doctoral thesis was to grow monolayered TMDs (MoS<sub>2</sub> and WS<sub>2</sub>) by CVD and study them by photoluminescence (PL) spectroscopy at different temperatures and different laser powers. PL spectroscopy was chosen as the main characterization method because it allows to study the excitonic emissions at different conditions and enables to gain new knowledge about the defect structure, stability, and homogeneity of these materials.

To achieve the aims of this thesis, the following issues were investigated during this work. Firstly, a monolayered MoS<sub>2</sub> with high density of defects was studied and the presence of the B trion was detected. Secondly, the properties of an aged WS<sub>2</sub> monolayer on Si/SiO<sub>2</sub> substrate were studied and the exciton localization routes in this material were determined. Thirdly, the properties of the defect-bound exciton band in WS<sub>2</sub> monolayer at low temperatures were thoroughly studied. Finally, the PL properties of a WS<sub>2</sub> monolayer at elevated temperatures and the temperature-induced degradation were investigated.

The present thesis is based on four published peer-reviewed papers and divided into three main chapters. Chapter 1 presents a literature overview of the main methods and known optoelectronic properties of the TMDs. In the end of chapter 1, the literature

overview is summarized, and the aims of the thesis are formulated. In chapter 2, the experimental details are described, including the growth conditions for TMDs and the characterization tools. The results and discussion are presented in chapter 3. Chapter 3 is subdivided into four sections, each based on a separate paper that are the basis of this thesis. In conclusion, the main results are summarized. Some results of this thesis have been presented by the author at different conferences.

This work was financially supported by European Union through the European Regional Development Fund, Project TK141, by the institutional research funding IUT 19-28, by the Estonian Research Council grant PRG1023, and by FP7 project CHEETAH, EC grant agreement no. 609788. Part of the equipment used in this work was financed by ASTRA 5-7 programme. This work was partially supported by the ASTRA “TUT Institutional Development Programme for 2016-2022” Graduate School of Functional Materials and Technologies (2014-2020.4.01.16-0032).

## Abbreviations, Terms and Symbols

2D	Two-dimensional
$\alpha$	Absorption
$A_1$	Process rate parameter
AFM	Atomic force microscope
$\beta$	Coefficient for the interaction of excitons with acoustic phonons
CBM	Conduction band minimum
CVD	Chemical vapor deposition
$E_a$	Activation energy
$f(E, T)$	Distribution function
FWHM	Full width at half maximum
$\hbar\omega$	Average phonon energy
$\hbar\omega_{LO}$	Longitudinal optical phonon energy
LSE	Localized-state ensemble
$n_s$	Refraction index of the SiO <sub>2</sub> layer
PL	Photoluminescence
$\rho(E)$	Density of states function
RC	Reflectance contrast
$R_L$	Reflectance spectrum from the WS <sub>2</sub> monolayer
$R_S$	Reflectance spectrum from the Si/SiO <sub>2</sub> substrate
$\sigma$	Width of the density of states function
$S$	Electron-phonon coupling strength
SEM	Scanning electron microscope
TMD	Transition metal dichalcogenide
$1/\tau_r$	Rate of radiative recombination
$1/\tau_{tr}$	The attempt-to-escape rate of localized carriers
VBM	Valence band maximum
$\phi$	Integral intensity of the PL band

# 1 Literature review

With the discovery of the first two-dimensional (2D) material – graphene [1] in the year 2004, a new path in material science was discovered. Other new 2D materials with equally interesting properties, have followed the success of graphene. All monolayers of these materials are less than a nanometer thick [2], [9]. A small part of the ever-growing family of 2D materials is illustrated in Fig. 1.1. One large group in the 2D material family is 2D semiconductors, also known as transition metal dichalcogenides (TMDs). TMDs have opened new possibilities for various electronic and optoelectronic applications that are based on atomically thin layers [10]–[12]. The list of applications that can be potentially improved using different TMDs include field-effect transistor sensors [13], field-effect transistors [14], valleytronic based devices [15] and photodetectors [16].

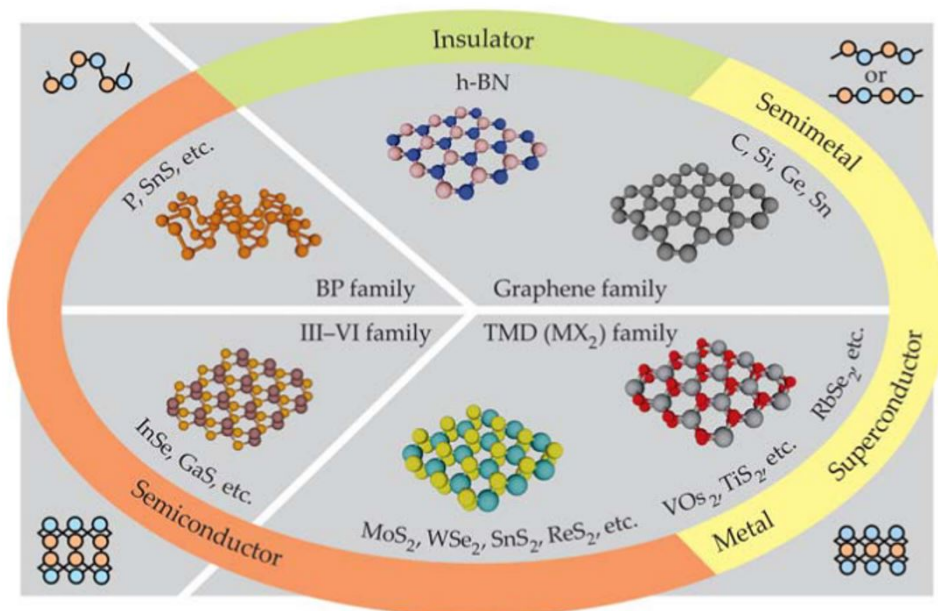


Figure 1.1: In the family of 2D materials are graphene (semimetal) and other analogues such as hexagonal boron nitride (insulator), semiconductor transition metal dichalcogenides (TMDs), and the black phosphorus (BP) family. 2D materials cover the full range of electronic properties. In the corners of the figure, the materials' cross-sectional structure is shown. [17]

Bulk TMDs are layered semiconductors composed of stacked sheets of atomically thin layers held together by van der Waals forces [18]. As van der Waals forces are weak, these layers can be exfoliated into monolayers or few-layer systems. The monolayers themselves have strong covalent bonds between cations and anions [19].

A monolayer consists of three atomic layers, where a layer of transition metal atoms is sandwiched between two chalcogen atom layers. An illustration of the atomic structure of two-layered TMDs is given in Fig. 1.2. TMD monolayers usually appear in the 2H phase, where the metal atoms are characterized by a trigonal prismatic geometry and the chalcogen layers are in an eclipsing configuration [20]. When either the top or bottom chalcogen layer is shifted, TMD monolayers are in another polymorph known as the 1T phase, which has tetragonal symmetry and corresponds to an octahedral coordination of the metal atoms [20]. Density functional theory calculation on the 1T phase freestanding

monolayer is unstable in the absence of external stabilizing influences and transforms into the 1T' phase [21], [22]. Phase transition from the stable 2H phase to the 1T phase, however, requires a considerable amount of energy [23]. The 2H phase is semiconducting and is often referred to as the trigonal prismatic structure, while the 1T and 1T' phases are metallic and are called octahedral and distorted octahedral, respectively [22]. The 1T' phase is the 1T phase after a symmetry-reducing distortion [22].

Layered TMDs can be distinguished by their different stacking orders. The 2H structure has two layers per unit cell stacked in hexagonal symmetry, while the 3R structure has three molecular layers in rhombohedral symmetry [19], [24].

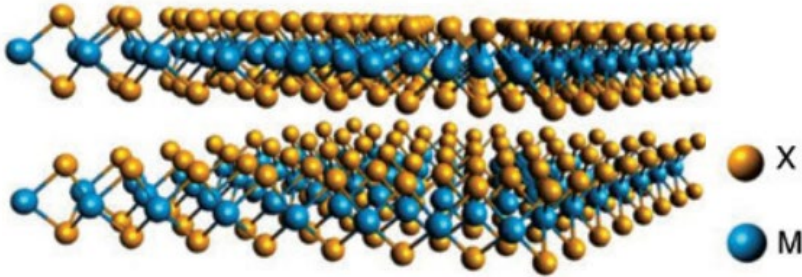


*Figure 1.2: A three-dimensional schematic of a two-layered TMD structure, where the atomic structure of a monolayer is in the form of  $MX_2$  ( $M = Mo, W$ ;  $X = S, Se, Te$ ). Modified image from [25]*

Best known TMDs are  $MoS_2$ ,  $MoSe_2$ ,  $WS_2$ ,  $WSe_2$ . In the form of a monolayer, these materials have desirable semiconductor properties for optoelectronic applications, such as direct band gap in the visible or near infrared spectral range. Due to the layered stacking features, individual layers of the TMDs can be obtained by several exfoliation or vapor deposition methods [26]. First, TMD monolayers were obtained via mechanical exfoliation [10]. After that, a number of different methods have been used to get TMD monolayers and other 2D materials, such as the mechanical exfoliation method [27], liquid exfoliation method [28]–[30], chemical vapor deposition (CVD) [31]–[33], wet chemical method [34] and many more innovative methods. Among these, the CVD method is the most popular one, especially for producing large areas (around 100  $\mu m$  and more in diameter) of high-quality TMD monolayers compatible with industry standards [26].

These previously listed methods can be divided into two general types of approaches – “top-down” and “bottom-up” methods [35]. Exfoliation methods are part of “top-down” approaches, while CVD can be classified as a “bottom-up” approach [26], [35].

With “bottom-up” method, the monolayers are grown from smaller atomic or molecular components. One of the most commonly used CVD synthesis routes involves two different processes, the evaporation of the precursors, which is followed by decomposition or further reactions to form the desired products [36], [37]. Only two precursors, which react in the vapor phase, are required for this approach – transition metal oxides/halides and chalcogen precursors. One important factor is the carrier gas, most commonly inert gases, such as Ar or  $N_2$ , that transport the vaporized precursors to the substrate during the growth process. However, several studies have found that the incorporation of  $H_2$  into carrier gas is important when Se is used as a chalcogen source [38], [39] or  $WO_3$  is the transition metal source [40], [41].  $H_2$  incorporation (forms  $H_2S$ )

can efficiently accelerate the reduction of  $\text{WO}_3$  powder and optimize the flake shape [42]. By the CVD method, TMD monolayer flakes have exhibited many different shapes [20], [43]–[46], such as triangles, hexagons, truncated triangles, six-point stars, and butterfly-like shapes.

The TMD monolayers by the CVD method are grown at elevated temperatures ( $T > 700$  °C), which makes the choice of the substrate of crucial importance. Thermally stable and rigid silicon substrate covered with a thin ( $\sim 300$  nm)  $\text{SiO}_2$  layer ( $\text{Si}/\text{SiO}_2$ ) is the most commonly used [42], [47]. More recently, alternative substrates, such as sapphire ( $\text{Al}_2\text{O}_3$ ), mica, molten glass, and Au foil have been widely implemented [42]. Sapphire and mica single crystal substrates offer atomically flat surfaces, good stability, perfect lattice matching, while molten glass can provide a flat liquid surface and lower nucleation density, promoting large crystal domain size and Au foils have a lower energy barrier, enabling ultrafast growth [42]. The possibility to transfer TMD films from the growth substrate to another substrate makes these materials even more promising for applications. Different potential applications need a more diverse selection of substrates, such as flexible substrates for flexible electronic and optoelectronic devices or substrates with dielectric properties to modify excitonic properties [47].

Over the years, the size of TMD flakes grown by the CVD method has progressed from a couple of micrometers to tens and hundreds of micrometers. The latest progress in the CVD growth has resulted in TMD flakes with sizes from  $500\ \mu\text{m}$  to  $2.5\ \text{mm}$  [6]–[8].

Bulk TMD has been shown to have an indirect band gap, while TMD isolated to a monolayer has a direct band gap. For example, bulk  $\text{MoS}_2$  has an indirect band gap with the value of around  $1.2\ \text{eV}$  that transfers to a direct band gap with the value around  $1.9\ \text{eV}$  for a  $\text{MoS}_2$  monolayer [48], [49]. In  $\text{WS}_2$ , the corresponding values have been found to be around  $1.3\ \text{eV}$  and  $2.0\ \text{eV}$ , respectively [48].

The phase diagram of a bulk TMD normally shows an indirect band gap from  $\Gamma$  point to an intermediate point in the Brillouin zone ( $\Gamma - \text{I}$ ). Monolayered TMD has a direct band gap at the K point in the Brillouin zone, which results in a strong photoluminescence (PL) emission. If a TMD has two layers, the indirect band gap ( $\Gamma - \text{I}$ ) becomes significant and the direct band gap character is reduced. Furthermore, the intensity of the PL emission is significantly reduced.

One nondestructive and quick method to identify monolayered TMDs from bulk TMDs is Raman spectroscopy. Raman spectra of the TMDs include first-order modes at the Brillouin zone center - in-plane mode  $E_{2g}^1(\Gamma)$  and the out-of-plane mode  $A_{1g}(\Gamma)$ . It has been found that the separation of these Raman peaks decreases with the decreasing thickness of the TMD. In the monolayered  $\text{WS}_2$ , the in-plane mode  $E_{2g}^1(\Gamma)$  was found at  $355.2\ \text{cm}^{-1}$  and the out-of-plane mode  $A_{1g}(\Gamma)$  at  $417.2\ \text{cm}^{-1}$ , resulting in the separation of these peaks  $\Delta = 22.0\ \text{cm}^{-1}$ , while the separation in bulk  $\text{WS}_2$  was  $\Delta = 25.2\ \text{cm}^{-1}$  [50]. In monolayered  $\text{MoS}_2$ , the corresponding separation was found to be  $\Delta = 18.0\ \text{cm}^{-1}$  ( $E_{2g}^1(\Gamma)$  at  $384.7\ \text{cm}^{-1}$  and  $A_{1g}(\Gamma)$  at  $402.7\ \text{cm}^{-1}$ ), while for bulk  $\text{MoS}_2$   $\Delta = 24.8\ \text{cm}^{-1}$  was obtained [51]. However, these values do not only depend on the thickness of the material, but also on other external properties or conditions that can affect the Raman spectra of the TMDs. These external perturbations can be strain, pressure, electric field, charge transfer, temperature, and substrate under the TMD [52].

Another Raman mode that can be used to identify  $\text{WS}_2$  monolayers is a zone-edge mode, which is identified as the longitudinal acoustic mode at the M point ( $\text{LA}(\text{M})$ ). This mode is activated by disorder and has the strongest intensity with laser excitations that meet the resonance requirements (for example, a laser with  $514\ \text{nm}$  wavelength).

However, in the case of resonance, 2LA(M) is the dominating mode only in the monolayer and it loses its relative intensity with the increasing number of layers [50]. This means that both frequency shifts and changes in relative intensity can be used to identify monolayered WS<sub>2</sub>.

Another method to study the TMDs is photoluminescence spectroscopy (PL). PL method is a useful method for the identification of different excitonic emissions in TMDs at low-, room-, and high-temperatures. Excitons in TMDs are observable at higher temperatures due to high exciton binding energy  $E_B$  reaching almost a hundred meV. TMDs can often be characterized by two exciton peaks, called the A-exciton and B-exciton, respectively. Due to the spin-orbit coupling, the valence band maximum (VBM) at the K point is split into two bands with distinct spin orientation and the conduction band minimum (CBM) is nearly degenerate. The A-exciton arises from vertical transition at the K point, while B-exciton is the vertical transition between the split valence band and the conduction band (illustrated in Fig. 1.3) [4], [53].

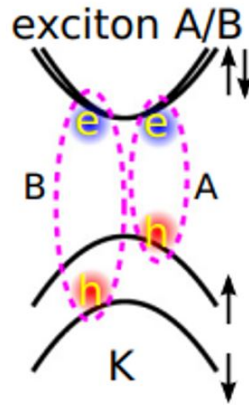


Figure 1.3: Illustration of the A and B exciton systems constructed from the electrons in the conduction band and holes in the A and B valence bands, respectively. Modified image from [53]

A- and B-excitons are charge-neutral excitons (a bound state of an electron and a hole), however the A-exciton emission has often higher PL intensity than the B-exciton emission and is therefore more extensively studied. Besides A- and B-excitons, other excitonic quasiparticles also exist in TMDs, such as charged excitons, also known as trions. Trion emission can be found at lower energy compared to exciton emissions (either A or B) and can be excited in the presence of residual excess charge carriers. Trions either consist of two holes and one electron or two electrons and one hole (see Fig. 1.4 (c)) [54]. The formation of a quasiparticle consisting of two excitons (biexcitons) is also expected in monolayered TMDs due to the large exciton binding energy. Biexcitons can either be bound or unbound (see Fig. 1.4(d)). Biexciton PL emission is at energies below the exciton and trion emission due to the additional binding energy [5], [54]. An extensive list of different exciton types in TMDs is illustrated in Fig. 1.4.

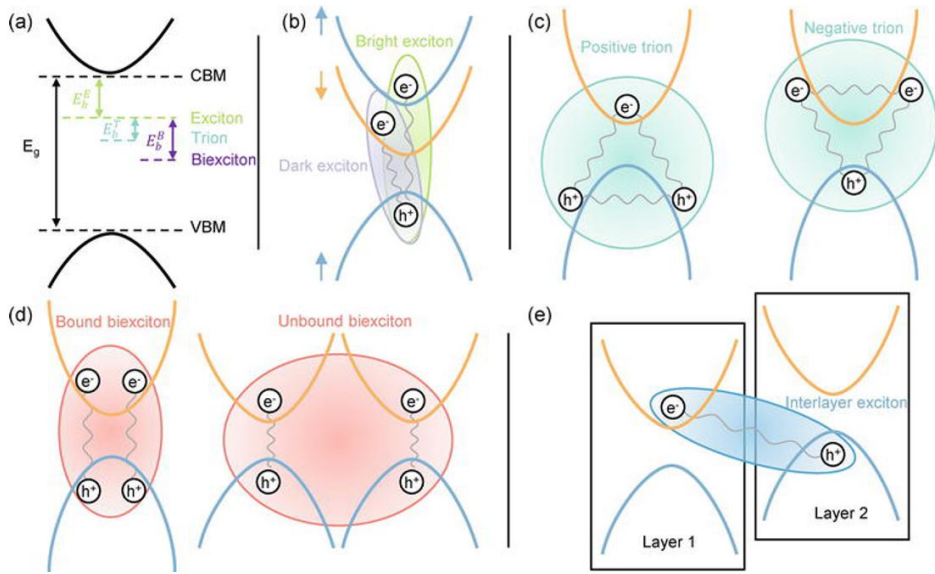


Figure 1.4: Different exciton types in TMDs (a) Schematic of the energy levels containing binding energies of excitons, trions, and biexcitons. (b) Excitons are Coulomb-bound electron-hole pairs (illustrated as ovals in the figure): Bright excitons consist of electrons and holes with antiparallel spins, while dark excitons consist of electrons and holes with parallel spins. (c) Trions emerge when an additional electron or hole joins the exciton, forming negative or positive trions, respectively. (d) Biexcitons are created from two free excitons with different total momenta. (e) Interlayer excitons appear when electrons and holes are located in different layers. [5]

## 1.1 General properties

### 1.1.1 Molybdenum disulfide – MoS<sub>2</sub>

MoS<sub>2</sub> is one of the first discovered and the most studied monolayered TMD. Monolayered MoS<sub>2</sub> has a direct band gap, while the bulk MoS<sub>2</sub> has an indirect band gap. With the decreasing thickness of the MoS<sub>2</sub> layer, the PL intensity increases remarkably. The room temperature PL spectrum of monolayered MoS<sub>2</sub> is characterized by two excitonic bands at around 1.8 and 1.95 eV and they are called A and B exciton bands, respectively. The presence of two excitonic bands is related to the spin-orbit splitting of the valence band ( $\Delta_{SO}$ ). For MoS<sub>2</sub>  $\Delta_{SO} \sim 160$  meV (148 meV [55],  $170 \pm 2$  meV [56]) has been determined. Concurrently the splitting of the conduction band was found to be smaller than 5 meV [55], [57].

However, the actual peak position of A and B bands depends on the type of the substrate and on the quality of the monolayer. Namely, it has been shown that CVD grown monolayers on Si/SiO<sub>2</sub> substrates usually exhibit PL emission at lower energy than in exfoliated monolayers [58], [59]. The redshift of the PL bands is caused by intrinsic tensile strain [60], [61]. The strain and the presence of lattice defects do not only affect the properties of PL bands, but also the position of Raman peaks of the monolayer [62]–[65]. The A excitonic band is often a sum of neutral exciton (A<sup>0</sup>) and trion (A<sup>-</sup>) emissions [66]–[70]. A trion is a charged exciton that can be either negative (A<sup>-</sup>) or positive (A<sup>+</sup>) depending on the type of majority carrier and its emission is at lower energy than neutral excitonic emission. The theoretical calculations have predicted the double



peak structure also for the B band [53], [71], [72]. Indeed, the negative B trion ( $B^-$ ) has been experimentally observed by reflectance contrast measurements in both  $WSe_2$  and  $MoSe_2$  [73], however, it has not been detected in PL studies.

### 1.1.2 Tungsten disulfide – $WS_2$

Among TMDs, the 2D semiconductor monolayered  $WS_2$  is particularly promising for a variety of future optoelectronic applications, as it has the largest band gap in the visible spectral range, at around 2.0 eV, and it usually also exhibits the most intense photoluminescence emission. Similarly to  $MoS_2$ , the characteristic PL spectrum of  $WS_2$  monolayer consists of two excitonic peaks – A- and B-excitons, with peak positions near 2.0 and 2.4 eV, respectively. The two exciton peaks are the result of the spin-orbit splitting of the valence band by  $\Delta_{SO} \sim 430$  meV (430 meV [55],  $425 \pm 18$  meV [56]). The large difference between the valence band splitting for  $WS_2$  than  $MoS_2$  can be explained by the larger intrinsic spin-orbit coupling of tungsten compared to that of molybdenum [56].

The peak position of the A-exciton peak is very sensitive to the preparation method and to the substrate properties. An A-exciton peak at around 2.0 eV has been found in mechanically exfoliated  $WS_2$  monolayer [74]. In the case of CVD grown  $WS_2$  monolayers on Si/SiO<sub>2</sub> substrate, the built-in strain and altered charge-carrier concentration causes the A exciton PL peak to redshift [75]–[77]. This strain will be relaxed when such monolayers are transferred to another substrate [47]. Defects in monolayers are another factor, which can affect the PL emission, namely, PL intensity. Two types of defects, radiative and non-radiative, have been proposed [78], however, their precise influence is complex. Still, it seems that the radiative defects are concentrated at the edges (see Fig. 1.5) and at the grain boundaries [79].

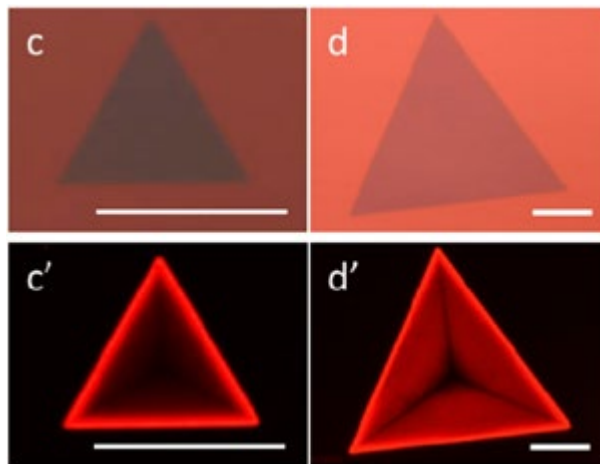


Figure 1.5 (c,d) Optical microscope images of triangular  $WS_2$  monolayers. (c',d') PL images of the same triangles illustrating higher PL intensity at the edges. Scale bars = 20  $\mu m$ . Modified image form [79]

## 1.2 Aging of TMD

For applications, it is important that materials have high thermal and chemical stability. As 2D materials are extremely thin, stability is even more important, otherwise monolayers can corrode, decompose, and have degenerative issues. As of 2013, according to Geim *et al.* TMDs were considered air-stable semiconductors in ambient conditions. However, recent studies show that TMD monolayers do not exhibit so good long-term stability in air as expected [80]–[82]. Gao *et al.* [81] have detected that CVD grown WS<sub>2</sub> and MoS<sub>2</sub> monolayers have large-scale structural and morphological changes after about 1 year storage at ambient conditions. Environmental degradation occurs due to the presence of oxygen and moisture in the air, resulting after a year of storage in oxidized metal states and organic adsorbates in both aged MoS<sub>2</sub> and aged WS<sub>2</sub> monolayers. The oxidation and eventually degradation starts at the defects, grain boundaries, and edges of the TMD flakes [81], [83] and these processes can be accelerated by using higher temperatures [83]. However, the optical properties of aged TMD monolayers have not been studied in detail yet. It has been shown that the surface roughness of the aged MoSe<sub>2</sub> monolayers is increased [84], causing a random distribution of tensile strain in the monolayer. This can lead to spatial optical band gap fluctuations in the material, which in turn are capable of localizing excitons.

## 1.3 TMD properties at low temperatures

At room temperature, the PL spectrum of WS<sub>2</sub> is dominated by charge-neutral A-exciton peak that is often accompanied by the charged trion A<sup>-</sup> peak at about 43 meV lower energy [54]. At lower temperatures ( $T \approx 10$  K), the PL spectrum of WS<sub>2</sub> monolayer is found to be dominated by a broad defect-bound exciton band ( $X_D$ ) at around 1.9 eV [85]. In addition single-photon emission has been detected in the same spectral region of the low temperature PL spectra of WS<sub>2</sub> monolayer [86] and WSe<sub>2</sub> monolayer [60], [87], [88]. Single-photon emission is a series of sharp peaks in the defect band spectral region. At low temperature, the PL spectrum of MoS<sub>2</sub> monolayers is characterized by the A-band (A<sup>-</sup> trion at around 1.92 eV and A-exciton at around 1.96 eV) and the B-band at around 2.1 eV.

The origin of excitons in the defect band is not fully known. One suggestion is that the excitons in the defect band region can be bounded to lattice defects [89], [90]. In addition to lattice defects, Venanzi *et al.* [91] have shown that the excitons in defect-bound exciton band are localized by physisorbed gas molecules on the MoSe<sub>2</sub> monolayer surface. This phenomenon can appear in other TMDs like WS<sub>2</sub>.

## 1.4 TMD properties at high temperatures

Exceptionally high exciton binding energy  $E_B$  values such as 0.71 eV [3] and 0.83 eV [4] have been determined for monolayered WS<sub>2</sub>. High exciton binding energy has also been found in other TMDs, thus making excitonic emission observable in these materials at room temperature and even above that. Due to this interesting feature, it has been proposed by Li *et al.* [92] that MoS<sub>2</sub> monolayers can be used in opto-electronic devices that work in elevated temperatures.

To establish operating conditions in future applications, which may involve elevated working temperatures, high temperature measurements are necessary. Until now, several high-temperature PL studies of A exciton peak have been conducted with a variety of

contrasting results. An increase in the PL intensity with temperature has been reported in monolayered MoS<sub>2</sub> [92], [93]. Moreover, an initial increase in the PL intensity of monolayered MoS<sub>2</sub> was followed by the subsequent decrease with further increase in the temperature [92]. Contradicting previous results, a monotonic decrease of PL intensity with temperature has also been observed in MoS<sub>2</sub> monolayers [94].

Contradictory behavior of the PL emission at elevated temperatures has been seen also in other TMDs besides monolayered MoS<sub>2</sub>. Zhu *et al.* [95] observed PL enhancement at temperatures above 300 K in few-layer WSe<sub>2</sub>, but a monotonic decrease in single-layer WSe<sub>2</sub>. Increasing PL intensity above room temperature has been also observed in multilayered WS<sub>2</sub> [96], while Chen *et al.* [93] reported that in WS<sub>2</sub> monolayers they observed an initial decrease of PL intensity above room temperature, which was followed by an increase of PL intensity and then followed again by a subsequent decrease with further increase in temperature. These previous results are quite unusual, because typically the reduction of PL intensity in semiconductors at elevated temperatures is observed. In contrast, Gaur *et al.* [97] have shown that PL intensity indeed decreases constantly in the temperature range of 83–473 K for single-layer WS<sub>2</sub> grown on sapphire. Similar results were reported also by Su *et al.* [77], who showed that the PL peak has a redshift and a decrease in intensity with increasing temperature for both irregularly shaped WS<sub>2</sub> monolayer grown on Si/SiO<sub>2</sub> and a triangular WS<sub>2</sub> monolayer grown on sapphire. Integrated PL intensity has also been observed to decrease in vertically stacked WS<sub>2</sub>/MoS<sub>2</sub> monolayer heterostructure at temperatures above room temperature [98]. The latter was attributed to a thermally activated non-radiative recombination mechanism.

PL intensity is not the only photophysical parameter that can be affected by elevated temperatures. Additionally, degradation of TMDs has been observed at elevated temperatures. In single-layer MoS<sub>2</sub> degradation has been seen in different environments. Namely, the appearance of small triangular holes in a hydrogen and argon gas mixture at around 773 K has been reported [99] and grain boundary degradation has been seen when heated in air [100].

## 1.5 Summary of literature review and aim of the study

2D semiconductors, such as TMDs, are less than a nanometer-thick semiconductors with interesting and useful properties for future optoelectronic and electronic devices. As this new class of materials are relatively new and emerging, there are still many fundamental aspects that need to be studied before these materials can be used in applications. Some of the well-known TMDs are MoS<sub>2</sub>, MoSe<sub>2</sub>, WS<sub>2</sub>, WSe<sub>2</sub>.

According to the literature, among many different TMD obtaining methods, the CVD method is the most popular one. The CVD method has been used to produce large areas of TMD monolayers with high quality, also showing promising results to be compatible to industry standards, as the latest progresses have resulted in TMD flakes with sizes from 500 μm to 2.5 mm.

A great method to study the optical properties and excitonic emissions in TMDs is PL spectroscopy. Due to the high exciton binding energy  $E_B$ , excitons are observable in TMDs at room temperature and even higher. At room temperature, TMDs can be characterized by two exciton peaks (A- and B-excitons), due to the spin-orbit splitting of the valence band. The A excitonic band is often a sum of neutral exciton (A<sup>0</sup>) and trion (A<sup>-</sup> or A<sup>+</sup>) emissions. It has been shown by theoretical calculations, that the B band is expected to have the same double peak structure as A excitonic band. However, the B trion emission has not yet been observed by PL spectroscopy.

Before TMDs can be used in applications, high thermal and chemical stability is important. Environmental degradation can occur due to the presence of oxygen and moisture in the air. After a year of storage, oxidized metal states and organic adsorbates have been detected in both aged MoS<sub>2</sub> and aged WS<sub>2</sub> monolayers. Oxidation and eventually degradation starts at defects, grain boundaries and at the edges of the TMD flakes, high temperatures can accelerate these processes. Aging in TMDs can also lead to the increase of the surface roughness that can lead to localized excitons.

At lower temperatures ( $T \approx 10$  K), the PL spectrum of a WS<sub>2</sub> monolayer is found to be dominated by a broad defect-bound exciton band ( $X_D$ ). The peak position of  $X_D$  has been found to be around 1.9 eV at low temperatures. The origin of excitons in the defect band is not fully known. It has been suggested that the excitons in the defect band region can be bounded to lattice defects or are localized by physisorbed gas molecules on the monolayer surface.

As monolayered WS<sub>2</sub> has exceptionally high exciton binding energy (0.71 eV or 0.83 eV), several high-temperature PL studies of A exciton peak have been conducted. However, the studies have had a variety of contrasting results so far. PL intensity is not the only photophysical parameter that can be affected by elevated temperatures. Additionally, degradation of TMDs has been observed at elevated temperatures and different environments. Namely, the appearance of small triangular holes in a hydrogen and argon gas mixture at around 773 K has been reported and grain boundary degradation has been seen when heated in air.

Based on the literature summary, this work aims to grow monolayered TMDs by chemical vapor deposition (CVD) and study them by photoluminescence spectroscopy (PL) at different temperatures and different laser powers. Photoluminescence spectroscopy allows to study the excitonic emissions at different conditions, in order to get a better understanding of the stability and homogeneity of these materials. The aim is divided into the following objectives:

- to grow MoS<sub>2</sub> and WS<sub>2</sub> monolayers by chemical vapor deposition method.
- to study single-layer MoS<sub>2</sub> with a high density of defects to detect the presence of the B trion.
- to study the properties of aged WS<sub>2</sub> monolayers on Si/SiO<sub>2</sub> substrate and to understand the exciton localization routes in this material.
- to study the properties of defect-bound exciton band in WS<sub>2</sub> monolayer at low temperatures.
- to study the properties of WS<sub>2</sub> monolayer at elevated temperatures and to identify how these temperatures consequently affect the degradation of the flake.

## 2 Experimental

This section is an overview of all experiments conducted in the frame of this thesis. Section 2.1 is about the CVD growth of  $WS_2$  and  $MoS_2$  monolayers. Section 2.2 is about the characterization methods used to study these monolayers. More details can be found in [I-IV].

### 2.1 Chemical vapor deposition of TMD monolayers

#### 2.1.1 CVD of $WS_2$ monolayer

The  $WS_2$  monolayers on Si/SiO<sub>2</sub> substrate studied in [I] were synthesized by an original tellurium-assisted CVD method at Rice University in Houston, USA. This synthesis was used to grow  $WS_2$  layers at a lower temperature (compared to synthesizes in [III, IV]) and under atmospheric pressure in a quartz reaction tube (inner diameter ~ 5 cm). W and Te powders were mixed and scattered on a Si/SiO<sub>2</sub> substrate, and the quartz tube was heated to 500 °C at a rate of 50 °C/min and was then kept at 500 °C for 15 min before cooling. The sulfur powder was loaded at the upstream zone inside the same quartz tube with a temperature of about 200 °C. Argon was used as carrier gas (100 sccm) and for protection from oxidation. No tellurium containing phases were detected in the resulting  $WS_2$  layers after growth. The samples were stored at room temperature in a container for about 1 year before the study.

$WS_2$  monolayers studied in [III] were grown by the CVD method in Tallinn University of Technology. For growth,  $WO_3$  and S precursors and a Si/SiO<sub>2</sub> substrate were used. A two-zone furnace with separated heating zones (MTI Corporation, OTF-1200X) was used and the temperatures for the zone with sulfur (Zone 1) and the zone with  $WO_3$  powder (Zone 2) were 200 °C and 850 °C, respectively (See Fig. 2.1). A mixture of  $N_2$  and  $H_2$  (9%) gases was used as the carrier gas with a flow rate of 132 sccm. The Si/SiO<sub>2</sub> substrate was placed face down next to the  $WO_3$  precursor. The  $WO_3$  powder zone reached 850 °C 15 min before the sulfur zone reached its maximum temperature of 200 °C, the system was held at both maximum temperatures for 15 minutes. After that  $WO_3$  powder zone was let to cool down, the cooling of the sulfur zone started after additional 15 minutes.

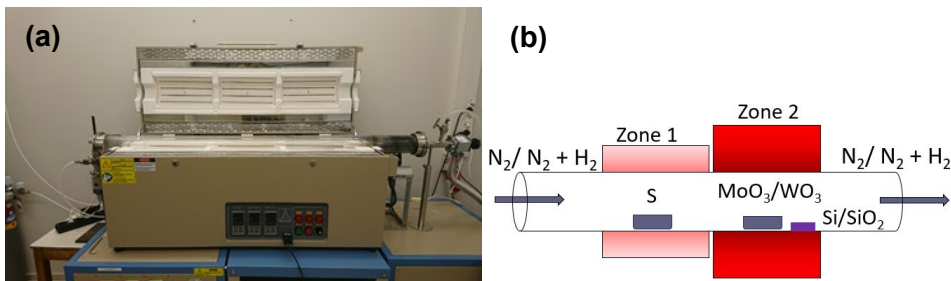


Figure 2.1 (a) Image of the experimental setup of the CVD system at Tallinn University of Technology. (b) Schematic view of the CVD method setup used in [II] and [III].

$WS_2$  monolayers studied in [IV] were synthesized by the CVD method at University of Duisburg-Essen in Duisburg, Germany. For fabrication, a multizone split tube furnace with thermally separated heating zones (ThermConcept, ROK 70/750/12-3z) was used. The substrates were Si/SiO<sub>2</sub> wafers. First, ammonium tungsten oxide hydrate (ATH) was

dissolved in deionized water. The solution with 1000 g/l was transferred onto the first substrate in several little droplets of ~1 mm in diameter. Subsequently, the substrate was heated under ambient atmosphere at 500 °C for 30 min to convert ATH into the tungsten source  $WO_3$ . Afterwards, cholic acid sodium salt (CAS) was spin coated as the seeding promoter onto the substrate containing  $WO_3$  as well as onto a second otherwise clean substrate. The substrate with  $WO_3$  was put into a crucible, the second substrate – only with seeding promoter – was flipped and put upside down onto the first one. The crucible containing the substrate and the tungsten source was put into the center heating zone and a second crucible filled up with 100 mg sulfur was put into the heating zone upstream. After sealing, the tube was purged with Ar gas. For the CVD process, the Ar flow rate was set to 50 sccm. The central heating zone was heated to 825 °C in 20 min and the sulfur heating zone to 150 °C in 10 min after a delay of 10 min. After holding the maximum temperatures for 30 min, the furnace was opened for rapid cooling.

### **2.1.2 CVD of $MoS_2$ monolayer**

$MoS_2$  monolayers on Si/SiO<sub>2</sub> substrate studied in [II] were grown by a CVD method in Tallinn University of Technology, in a two-zone furnace (MTI Corporation, OTF-1200X).  $MoO_3$  powder (Zone 2) and sulfur (Zone 1) precursors were used and their zones were heated up to 790 °C and 200 °C, respectively (See Fig. 2.1).  $N_2$  was used as a carrier gas with a gas flow of 100 sccm. The Si/SiO<sub>2</sub> substrate was positioned face-down at about 2 cm from  $MoO_3$  precursor. Similarly to the  $WS_2$  growth in [III], the  $MoO_3$  powder zone reached 790 °C 15 min before the sulfur zone reached its maximum temperature of 200 °C, the system was held at both maximum temperatures for 15 minutes. After that  $MoO_3$  powder zone was let to cool down, the cooling of the sulfur zone was started after additional 15 minutes. This growth process produced uniform  $MoS_2$  domains and the size of these areas ranges from several tens to more than a hundred micrometers.

## **2.2 Characterization**

Raman spectroscopy is a nondestructive method that gives information about the compositional and structural state of the sample and additionally it provides information about intrinsic strain and impurities. Raman spectroscopy is a method that is based on inelastic scattering of the light by the sample, which leads a small amount of scattered light to have different wavelengths, which depend on the chemical structure of the sample. Raman spectroscopy is a great method to determine the number of layers in TMDs.

Raman measurements were carried out using a confocal Horiba LabRAM HR800 Micro-Raman system equipped with a multichannel CCD detection system in the backscattering configuration with a spectral resolution better than 1  $cm^{-1}$ . For excitation, a continuous wave Nd-YAG laser (wavelength 532 nm) was used. The 50x and 100x objective lenses in the microscope were used for the measurements. Most measurements were carried out at room temperature and in ambient air. For temperature-dependent Raman measurements ( $T = 80 - 300$  K), Linkam THMS600 heating/cooling stage with liquid nitrogen was used.

Photoluminescence spectroscopy (PL) is a noncontact and nondestructive method to study materials. PL can be used to determine the recombination mechanisms, defects and impurities in the material and the quality of the material.

During this thesis, different micro-PL systems were used to carry out PL measurements. Room-temperature PL measurements were carried out using a confocal Horiba LabRAM

HR800 Micro-Raman. For excitation, a continuous wave Nd-YAG laser (wavelength 532 nm) was used. A Linkam THMS600 heating/cooling stage was used for high temperature PL measurements ( $T = 298 - 723$  K) and for low-temperature measurements ( $T = 80$  K).

In [I], PL measurements were carried out at University of Tartu using a Renishaw inVia Raman microscope (using 50x or 100x objective lenses) equipped with a multichannel CCD detection system in the backscattering configuration with a spectral resolution better than  $1 \text{ cm}^{-1}$  and an Ar laser (wavelength 488 nm) for excitation. For the low temperature ( $T = 10 - 300$  K) PL and reflectance contrast (RC) measurements, the UTREKS-LSO cryosystem with the helium bath cryostat was used.

In [III], a continuous-flow liquid helium cryostat Janis ST-500 was used for the temperature-dependent ( $T = 15 - 295$  K) PL measurements. PL measurements were carried out using a 0.50m focal length monochromator ACTON 2500i and an Oxxius - LMX-532 laser (wavelength of 532 nm) with different powers. For PL detection, a liquid nitrogen-cooled CCD camera was used. Measurements were carried out during a research visit at University of Duisburg-Essen in Duisburg, Germany.

In [IV], PL measurements were carried out at high temperatures in an inert atmosphere. Before the measurements, several steps had to be followed. The cryostat was flushed with Ar gas for approximately 10 minutes and after that the valves were closed. The pressure at room temperature was around 2 atm. While the sample was heated, the cryostat housing had a water-cooling system. Samples were heated with a 10 K/min rate and were held at the desired temperatures for at least 5 min to let the sample temperature to stabilize. Measurements were performed in an argon atmosphere, preventing  $\text{WS}_2$  flakes from oxidizing.

PL imaging was carried out on a microscope unit with a high-power 420 nm light emitting diode (Thorlabs M420L3) for wide-field excitation and for detection through a 50x objective with a cooled Atik 414EX CCD camera (filters to remove excitation emission were employed) was used.

For reflectance contrast measurements (RC), a modified setup of the Raman system was used, where the laser was replaced with a halogen light source (Euromax Illuminator EK-1). To ensure constant light intensity, the light source was connected to a power source with a constant current. It has been shown [101], [102], that the absorption spectrum is directly related to the reflectance contrast spectrum. Two reflectance spectra  $R_L(E)$  and  $R_S(E)$  were measured from the  $\text{WS}_2$  monolayer and from the Si/SiO<sub>2</sub> substrate, respectively, as a function of the photon energy  $E$ ,  $n_s$  is the index of refraction of the SiO<sub>2</sub> layer and  $\alpha$  is the absorption of the sample. RC spectrum is defined as follows [101]:

$$RC(E) = \frac{\Delta R}{R}(E) = \frac{R_L - R_S}{R_S} = \frac{4}{n_s^2 - 1} \alpha(E) \quad (1)$$

An atomic force microscope (AFM; Bruker Multimode) with a Nanoscope V controller was used to determine the surface roughness and the thickness of the layers.

The high-resolution scanning electron microscope (SEM) HR-SEM Zeiss Merlin was used to study the morphology of some monolayers.

## 3 Results and discussion

### 3.1 Photoluminescence study of B-Trions in MoS<sub>2</sub> monolayers with high density of defects

In this section, CVD grown MoS<sub>2</sub> monolayers were studied by photoluminescence spectroscopy to detect B-trions. All following results have been published in the paper [II]. In Fig. 3.1, a SEM picture of the MoS<sub>2</sub> monolayer and the Raman spectrum from the marked red circle is presented. The Raman peaks associated with MoS<sub>2</sub>, namely, the in-plane mode  $E_{2g}^1(\Gamma)$  (381.7 cm<sup>-1</sup>) and the out-of-plane mode  $A_{1g}(\Gamma)$  (405.0 cm<sup>-1</sup>) are clearly seen in Fig. 3.1(b) [51], [103]. The separation between these peaks is  $\Delta = 23.3$  cm<sup>-1</sup> and this value is higher than the usually observed separation in high-quality monolayers ( $\Delta \approx 19$  cm<sup>-1</sup> [51]). Vertical-dashed lines in Fig. 3.1(b) mark the peak positions of high-quality exfoliated monolayer and, with respect to these lines, our CVD-grown MoS<sub>2</sub> has peaks that are either softened ( $E_{2g}^1(\Gamma)$ ) or stiffened ( $A_{1g}(\Gamma)$ ), which can be attributed to the presence of substrate-induced tensile strain and charge doping [61], [104]. The origin of tensile strain in CVD-grown MoS<sub>2</sub> layers has been attributed to the mismatch of the thermal expansion coefficient between the layer and a Si/SiO<sub>2</sub> substrate [61] or/and to the surface roughness [84], [105]. It is known that the lattice tensile strain affects predominantly the in-plane vibration mode  $E_{2g}^1(\Gamma)$  while the  $A_{1g}(\Gamma)$  mode is relatively unaffected: -2.1 cm<sup>-1</sup> per % strain and -0.4 cm<sup>-1</sup> per % strain, respectively [63]. According to these estimations, our MoS<sub>2</sub> monolayer seems to have a tensile strain in the range of 1%. However, the shift of the  $E_{2g}^1(\Gamma)$  mode can be also related to the high defect (mostly sulfur vacancies) concentration as was shown in ref. [65]. The blue shift of the  $A_{1g}(\Gamma)$  peak is believed to be a result of hole doping, because, due to the strong interaction between  $A_{1g}(\Gamma)$  phonon and electrons, the  $A_{1g}(\Gamma)$  mode is very sensitive to the doping of MoS<sub>2</sub> [106]. High concentrations of sulfur vacancies and cracked regions are very active centers for molecular adsorption and, for example, adsorbed O<sub>2</sub> and/or H<sub>2</sub>O can introduce hole doping and thus reduce the electron concentration [106]. As it was shown in refs. [61], [107], reduced electron concentration leads to a blue shift of the  $A_{1g}(\Gamma)$  peak compared with the peak position in the exfoliated high-quality monolayer. It was also shown that nitrogen doping could be an effective way to produce hole doping in MoS<sub>2</sub> monolayers [108] by creating  $N_S$  acceptor defects. The presence of weak side peaks at about 409 and 378 cm<sup>-1</sup> (see Fig. 3.1(b)) also confirms a high defect concentration in our monolayer, because these peaks were previously assigned to the defect-induced modes [109], [110].



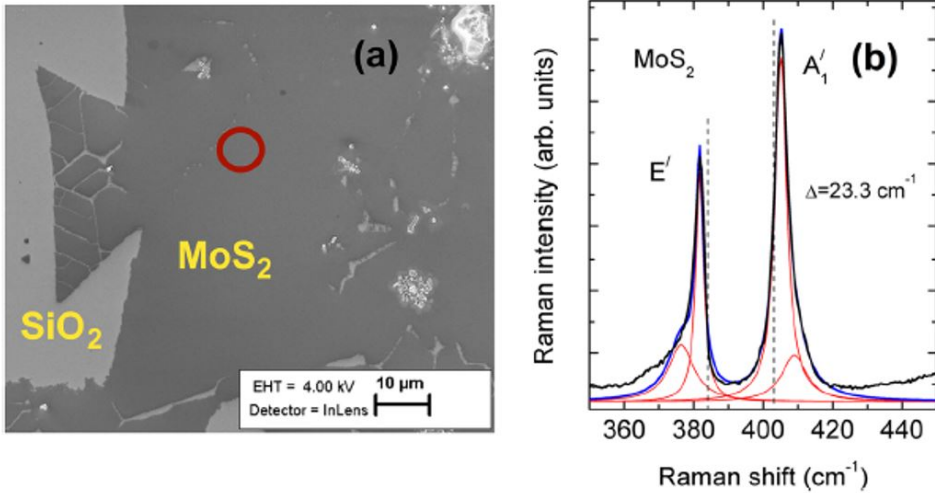


Figure 3.1: (a) SEM picture of our MoS<sub>2</sub> monolayer, the red circle indicates the location where Raman and PL spectra were measured. (b) Raman spectrum from the monolayer area of MoS<sub>2</sub>. Red lines show the result of spectral fitting with Lorentzian curves and the blue line is a cumulative fitting result. Vertical dashed lines represent the peak positions measured from high-quality exfoliated MoS<sub>2</sub> monolayers. [111] (Figure 1 in [II])

Room temperature PL spectra of MoS<sub>2</sub> show a clear presence of A and B bands at about 1.79 and 1.95 eV, respectively, see Fig. 3.2(a). Additional weak band X<sub>D</sub> at 1.69 eV is also visible and it is related to defect bound excitons [112]. The relative PL intensity of the B-band was higher than usually observed in high-quality MoS<sub>2</sub> monolayers, and the overall photoluminescence intensity was also rather weak. In addition, we noticed a faint continuous background emission and it was subtracted during further analysis. All PL bands are red-shifted with respect to the peak positions of high-quality exfoliated monolayers and this is typical for CVD grown strained MoS<sub>2</sub> on Si/SiO<sub>2</sub> substrates [61], [113]. At the same time, we did not observe any features corresponding to the indirect transition usually visible in multilayers at about 1.5 eV [114]. This fact confirms that the redshift of PL bands is caused by the strained and defective MoS<sub>2</sub> monolayer and not by the presence of multilayers. The effect of tensile strain on PL properties of MoS<sub>2</sub> monolayers is studied in many papers and it was found that the decrease in the optical band gap is approximately linear with strain,  $\approx 45$  meV per % of strain for monolayer MoS<sub>2</sub> [115]. Later studies showed even higher values,  $\approx 100$  meV per % of strain [61], [105], [116]. The peak position of the A-band in exfoliated MoS<sub>2</sub> monolayers is about 1.85 eV [117] and therefore we can expect to have  $\approx 0.6\%$  of strain in our monolayer. This strain is smaller than the estimated strain value from Raman measurements and therefore we expect that the shift of Raman peaks is partly caused also by charge doping.

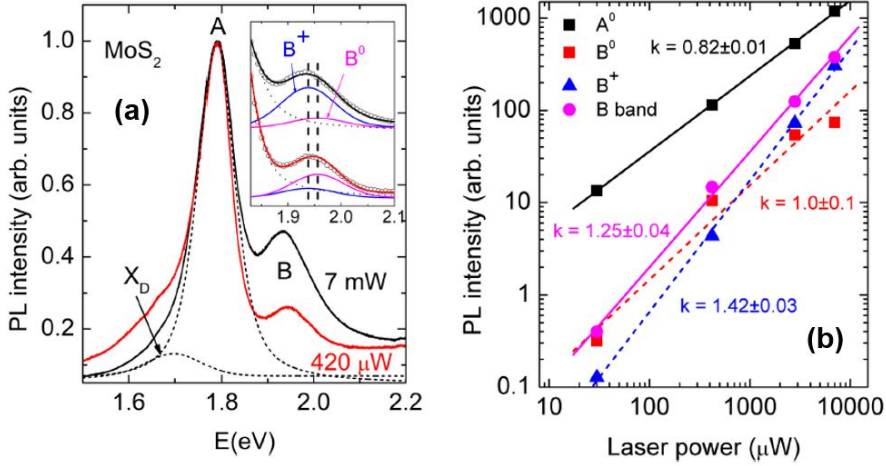


Figure 3.2: (a) Normalized room temperature PL spectra of MoS<sub>2</sub> monolayer measured at different laser power. The inset shows a magnified range of the B-band with fitting results using pseudo-Voigt peak shape function for exciton (B<sup>0</sup>) (magenta line) and trion (B<sup>+</sup>) (blue line) and A-band (dotted curve). Experimental points are presented as circles, fitting results are given with solid black and red lines. Peak positions of B<sup>0</sup> and B<sup>+</sup> are marked with dashed vertical lines. Fitting result for the A-band (at 7mW) is also shown as dashed lines. (b) Integrated photoluminescence intensity of different PL bands as a function of the laser power plotted on a log–log scale. The lines are least squares fit to the data. (A modified version of Figure 2 and Figure 3 in [II])

The increase of an excitation intensity leads to nearly linear increase of the A-band intensity, while the B-band shows a superlinear increase. Moreover, we noticed a redshift of the B-band with increasing laser power, but the shape and the peak position of the A-band did not change. All these facts confirm that the A-band does not contain additional trion emission and we observe only emission of neutral excitons A<sup>0</sup>. At the same time, the behavior of the B-band can be explained if both trions and neutral excitons are present. Different properties of A and B bands in our monolayer indicate that electrons in the conduction band play a minor role and holes in both valence bands determine the emission properties. Therefore, we probably have positive B-trions (B<sup>+</sup>) where two holes are paired with one electron. Accordingly, all PL spectra were fitted using a pseudo-Voigt line shape for A<sup>0</sup>, B<sup>+</sup>, and B<sup>0</sup>. The separation between our B<sup>0</sup> and B<sup>+</sup> bands was found to be 18 meV and it was kept constant in all fittings. Based on deterioration of the fit upon changing this separation, we estimate the uncertainty of the trion binding energy to be less than 2 meV. By changing the laser excitation intensity over a factor of 150, the peak positions and peak widths (FWHM) of these PL bands did not change, indicating no heating of the sample over the range of laser power used. An example of this fitting for the B band region is shown in Fig. 3.2 (a). At lower laser powers, the B<sup>0</sup> band dominates at 1.956 eV, but at higher laser powers, we clearly see a rapid increase of the B<sup>+</sup> band at 1.938 eV. The value of spin-orbit splitting in our monolayer is found to be  $\Delta E_{SO} = 166\text{meV}$  and it is slightly bigger than in high-quality monolayers. According to recent first-principle calculations [72], the binding energy of trions in MoS<sub>2</sub> monolayers somewhat depends on the substrate, and for Si/SiO<sub>2</sub> substrate values 35/32 and 18/17 meV were found for A<sup>-</sup>/A<sup>+</sup> and B<sup>-</sup>/B<sup>+</sup> trions, respectively. The latter agrees very well with our experimental value. Very small binding energy for

the B trion also explains why it is so difficult to resolve the B trion emission while the A trion is often visible even at room temperature.

In general, the excitation intensity dependence of the PL intensity is a good indicator of the nature of radiative recombination processes. Specifically, the integral PL intensity,  $I$ , shows a power law dependence on the laser excitation power,  $P$ , as  $I \sim P^k$ . A value of  $k \approx 1$  indicates an exciton-like transition and  $k \ll 1$  suggests a recombination path involving defects [118]. For trions, where the recombination involves three particles, the intensity should show a  $P^{1.5}$  dependence, i.e., superlinear increase with laser power [119]. If both trion and neutral excitons are present, then the increase of B-band intensity must have a superlinear dependence with  $1 < k < 1.5$ . The actual value of  $k$  for each PL band depends also on other conditions like type of a substrate, defect concentration, and crystal quality of monolayers. The dependence of the integral intensity of PL bands on laser power is presented in Fig. 3.2(b). Both neutral excitons ( $A^0$ ,  $B^0$ ) show a nearly linear increase with laser power (note that the  $B^0$ -band seems to have almost the same behavior as the  $A^0$ -band at higher laser power), but the  $B^+$  band increases with  $k = 1.42$ . This value correlates with the expected value for trions ( $k = 1.5$ ). The total intensity of the B-band increases with laser power as  $I \sim P^{1.25}$ .

All the properties of our  $\text{MoS}_2$  monolayer indicate that we have a very high concentration of defects and quite low carrier concentration. The reason for the fairly intense B-band emission, compared to those reported in the literature, is therefore assigned to defects. In particular, we assume that there is a non-radiative recombination channel that preferentially acts on the holes in the A-band. This can occur if the traps are energetically close to the valence band maximum, which is responsible for the A-band emission. For example, as it was shown in ref. [120], sulfur adatoms on the surface of  $\text{MoS}_2$  layer can introduce a very fast non-radiative recombination channel.

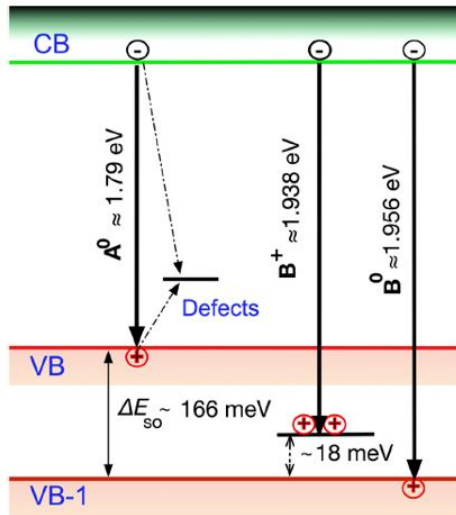


Figure 3.3: The band structure near the K-point of the Brillouin zone showing radiative and non-radiative emissions in  $\text{MoS}_2$  monolayer. (Figure 4 in [II])

The difference in the relative intensities of trions and excitons in the A and B bands also appears puzzling. After all, the presence of B-trions should imply the presence of free carriers and thereby also of A-trions. We speculate on two scenarios for this apparent discrepancy: either the density of A-trions or their emission intensity is suppressed. For the former, if there is fast recombination channel for the A-excitons, as also assumed above, they will recombine before they can find a free carrier and thereby form a trion. Thus, the A-trion formation is suppressed. In this scenario, it is irrelevant whether the free carriers are electrons or holes, as long as their concentration is low. The fast recombination channel does not need to be completely nonradiative, but it needs to be selective to A to keep the exciton density sufficiently low, while B-excitons live longer and form trions. In the latter scenario, the calculated lowest energy  $B^+$  trion has one hole in the highest valence band (VB) and one hole in the lower spin-orbit-split band (VB-1). This could in principle show up either as  $A^+$  trion or as  $B^+$  trion. However, due to the spin orientation in the relevant bands, it is expected to be dark in A, but bright in B, [72], [121] and thus shows up more strongly as  $B^+$ . The reason for the enhancement of this type of trions over “normal”  $A^+$  trions could be ascribed to the same process as in the previous scenario. Alternatively, we could assume that there is a fast non-radiative recombination mechanism that affects similarly both conduction band states, but preferentially the VB holes over the VB-1 holes. Then, B-exciton is broken via electron trapping and subsequently recombines with VB hole, but the hole is left in the VB-1 state. Since the hole concentration is subsequently reduced at VB state, this essentially leads to transferring the hole concentration from VB to VB-1. Consequently, the trion can be formed even as a combination of A-exciton and hole at VB-1.

The band structure of all observed emissions are summarized in Fig. 3.3. Following the above discussion, we have also illustrated the possible defect-induced recombination channel in the figure, although at present the exact nature of the defects remains unknown. Additionally, further studies are needed to investigate the properties of B-trions in more detail.

### 3.2 Local strain-induced band gap fluctuations and exciton localization in aged $WS_2$ monolayers

The  $WS_2$  monolayers studied in this section were grown by a tellurium-assisted CVD method at Rice University in Houston, USA, and all results have been published in greater detail in paper [1].  $WS_2$  monolayers mainly grew as triangular islands with domain sizes up to tens of micrometers (see Fig. 3.4(a) and (b)). There are also regions where additional 2L and even 3L layers can be observed in the center of some triangles. The thickness of as-grown  $WS_2$  monolayers was measured with AFM and was about 0.8 nm and the sample surface was quite smooth (surface roughness  $\sim 0.3$  nm) [122]. After one year, the typical surface roughness increased to 0.5 nm in aged  $WS_2$  monolayers and, in addition, a high density of nanocaps with the base diameter about 30 nm and an average height of 7 nm can be observed (see Fig. 3.4(c)). Similar nanocaps were found also in aged  $MoSe_2$  monolayers [84].

Fig. 3.5(a) shows the Raman spectra of the aged  $WS_2$  monolayer at different temperatures. All Raman spectra measured from different monolayer islands are quite similar and do not differ significantly from the spectra of as-grown layers. The frequency separation of 60  $cm^{-1}$  between  $E_{2g}^1(\Gamma)$  and  $A_{1g}(\Gamma)$  modes is typical for single layer  $WS_2$  measured in many papers [50], [52], [123], [124].

At the same time, the PL spectrum of the aged  $\text{WS}_2$  monolayer is redshifted about 24 meV, see Fig. 3.5(b). It is known that the PL peak position of TMD monolayers is very sensitive to the strain and often CVD grown monolayers show exciton emission at lower energy than monolayers transferred by mechanical exfoliation from bulk crystals. It has been shown that the thermal expansion coefficient (TEC) of  $\text{WS}_2$  is smaller than that of the Si/SiO<sub>2</sub> substrate [125]. Therefore, we will expect an in-plane compression stress on  $\text{WS}_2$  during cooling after CVD growth and, finally, the formation of tensile strain. It was found [126], that the strain affects the band gap energy and also the work function of  $\text{WS}_2$ . Often this compressive stress leads to the formation of ripples and other local inhomogeneities with different strain values. As it was shown [126], the tensile stress (positive strain) has a higher effect on the band gap energy than the compressive stress (negative strain). Therefore, it is natural to believe that in our aged monolayers some additional tensile strain is causing this 24 meV redshift of exciton PL peak and the origin of this extra strain seems to be related to the observed nanocaps.

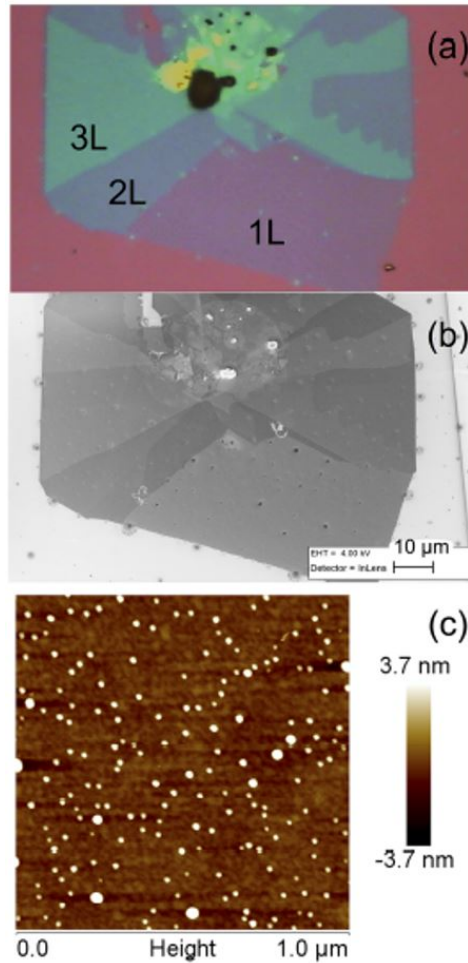


Figure 3.4: Optical (a) and SEM (b) microscopy images of  $\text{WS}_2$  layers on Si/SiO<sub>2</sub> substrate. The positions of single layer (1L), double (2L), and triple (3L) layers were indicated, (c) the AFM scan of the 1L area. (Figure 1 in [1])

The room temperature PL spectrum of the aged monolayer showed only one slightly asymmetric A-exciton peak. Completely different spectra were obtained at  $T = 10$  K, see Fig. 3.6(a), where 5 different PL bands can be clearly observed. All spectra were fitted using an asymmetric hyperbolic secant function:

$$I(E) = I_0 / [\exp((E - E_M)/W_{HE}) + \exp(-(E - E_M)/W_{LE})], \quad (2)$$

and the result of this fitting for one spectrum is also shown in Fig. 3.6(a). Here  $W_{HE}$  and  $W_{LE}$  are related to the width of high energy and low energy sides of the PL band, respectively, while  $E_M$  is related to the peak position  $E_{max} = E_M - [\frac{W_{HE}W_{LE}}{W_{HE}+W_{LE}}] \ln(\frac{W_{LE}}{W_{HE}})$ , but only in the case of a symmetrical band  $E_M = E_{max}$ . The hyperbolic secant function is found to fit well also excitonic PL bands in MoSe<sub>2</sub> monolayers [127].

The shape and intensities of the spectra taken from different islands and different positions differ significantly, demonstrating large spatial variations of monolayer properties. At the same time, the peak positions of all PL bands (except X<sub>D</sub>) remained almost constant. All 5 detected PL bands can be divided into 3 groups: A-exciton peaks  $A_S^0$  ( $E_{max} = 2.030$  eV) and  $A^0$  ( $E_{max} = 2.010$  eV); trion peaks  $A_S^-$  ( $E_{max} = 1.989$  eV) and  $A^-$  ( $E_{max} = 1.970$  eV), and a deep defect-related exciton peak X<sub>D</sub> ( $E_{max} = 1.93$  eV). The separation between double peaks is about 20 meV and the subscript S denotes here shallow states. The double structure of the exciton and trion peaks is rather extraordinary and can be seen merely at very low temperatures ( $T < 30$  K). At higher temperatures, only  $A^0$  and  $A^-$  peaks together with X<sub>D</sub> peak persist. The origin of double peaks will be further discussed later. The rather high intensity of defect-related exciton peak X<sub>D</sub> in all monolayer islands is a clear indication of the high concentration of defects in aged WS<sub>2</sub> monolayers. We also observed that the high intensity of X<sub>D</sub> peak is usually accompanied by the high intensity of the trion peak.

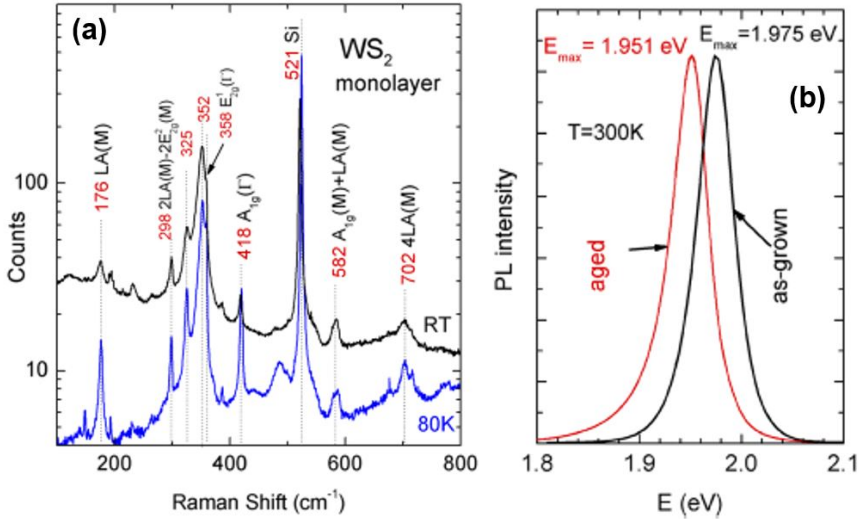


Figure 3.5: (a) Room temperature (black) and low temperature ( $T = 80$  K) (blue) Raman spectra from a WS<sub>2</sub> monolayer region. (b) Normalized room temperature PL spectra of as-grown and aged WS<sub>2</sub> monolayers. The separation between PL peaks is 24 meV. (A modified version of Figure 2 and Figure 3 in [1])

Figure 3.6(b) presents the PL spectra of an aged  $\text{WS}_2$  monolayer measured at  $T = 80$  K using different laser power. All spectra were fitted with an asymmetric hyperbolic secant function (Eq. 2) and the fitting result for 3.5  $\mu\text{W}$  spectrum is presented as blue and red lines. The inset shows the integrated intensities of  $A^0$ ,  $A^-$  and  $X_D$  bands as functions of the excitation power. With the increase in the excitation power, the emission from exciton and trion states linearly increases (slope = 1) over the whole studied range. The emission from  $X_D$  shows a sublinear dependence and saturates at higher excitation power. Similar saturation of the wide  $X_D$  band was observed also in  $\text{MoS}_2$  [128] and in other  $\text{WS}_2$  monolayers [54]. The nature of the defects responsible for the  $X_D$  band is not clear, but due to the very broad and somewhat variable shape of this band we can expect the presence of several different defects.

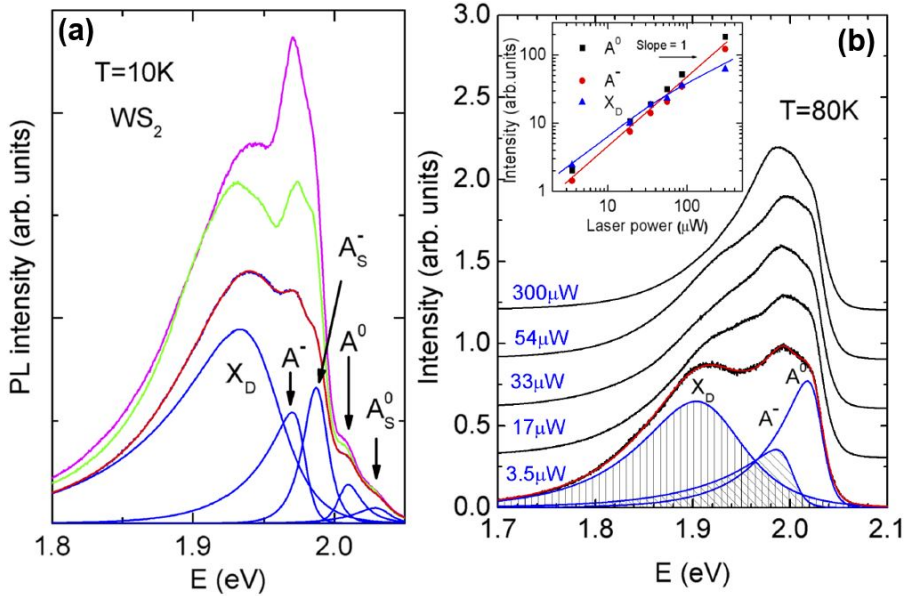


Figure 3.6: (a) Low temperature ( $T = 10$  K)  $\mu\text{PL}$  spectra of an aged  $\text{WS}_2$  monolayer island taken from 3 different spots. Result of spectral fitting with an asymmetric hyperbolic secant function (Eq. 2) is also shown for one spectrum. (b) Excitation intensity dependent normalized PL spectra of aged monolayer  $\text{WS}_2$  measured at  $T = 80$  K and a result of fitting with asymmetric hyperbolic secant function (Eq. 2). All spectra are vertically shifted for clarity. The inset shows the integrated intensity of different peaks as a function of laser power. (A modified version of Figure 4 and Figure 5 in [1])

For temperature-dependent RC and  $\mu\text{PL}$  measurements, we selected monolayer regions, where low-temperature PL intensities of  $X_D$  and trion bands were lowest and, thus, the shape of the  $A^0$  band is relatively well defined. Unfortunately, at temperatures  $T < 80$  K, the  $X_D$  and trion bands start to appear and the reliability of PL spectral fitting suffers a lot. This was not the case with RC measurements (calculated by Eq. 1), where the spectra were unaffected by trion resonances even at very low temperatures, see Fig. 3.7 (a). As it was shown [102], the inverted reflectance contrast spectra of 2D monolayers near the exciton resonances are usually proportional to the absorption and therefore the shape of inverted RC can be used to probe the density of excitonic states. For the RC peak fitting, we used again the asymmetric hyperbolic secant function (Eq. 2) after subtracting the slowly changing background. The asymmetric hyperbolic secant

function was used because the RC peak had an asymmetric shape with larger width at the low energy side. The ratio  $W_{LE}/W_{HE}$  was about 2.5 and did not change with temperature. Both A and B exciton peaks were detected. The same fitting function was used also for PL spectra, presented in Fig. 3.7 (b). Values for peak position  $E_{max}$  and full width at half maximum (FWHM) for  $A^0$ -exciton peaks were calculated numerically from the fitting curves and are presented in Fig. 3.8.

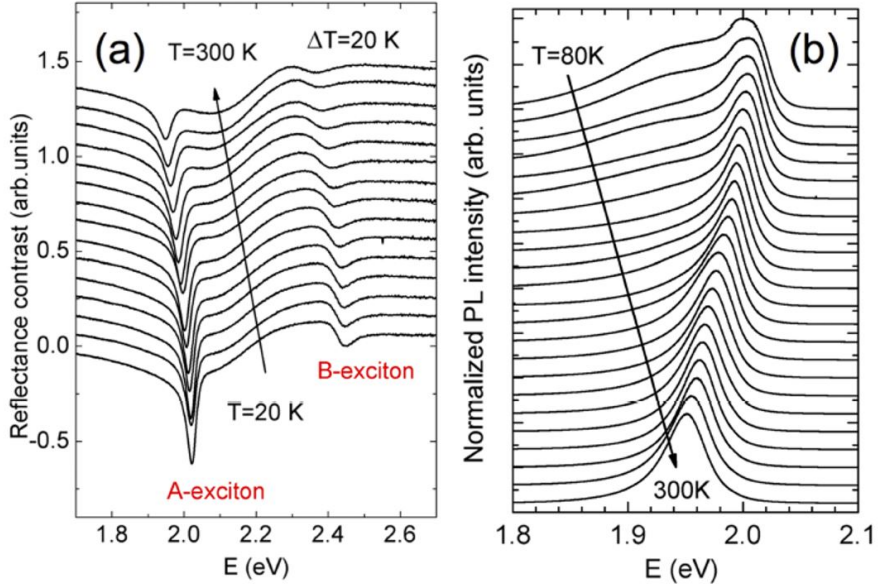


Figure 3.7: (a) Temperature dependence of the reflectance contrast spectra of aged  $WS_2$  monolayer showing A and B exciton resonances. (b) Temperature evolution of normalized  $A^0$ -exciton PL emission. (Figure 6 in [1])

The temperature dependence of  $A^0$ -exciton peak position obtained from RC measurements can be well described by a standard semiconductor bandgap model [129]:

$$E_{max} = E(0) - S\hbar\omega[\coth(\hbar\omega/2kT) - 1], \quad (3)$$

where  $E(0)$  is the peak position at  $T = 0$  K,  $S$  is the dimensionless electron-phonon coupling strength and  $\hbar\omega$  is the average phonon energy. The fitting result with Eq. 3 is shown as a red line in Fig. 3.8 (a) and the parameters found from the fitting are given in Table I. Very similar behavior is seen also for B peak, see Fig. 3.8(a). The separation between A and B exciton peaks is  $\sim 420$  meV and this value is very close to the spin-orbit splitting of the valence band  $425 \pm 18$  meV found for  $WS_2$  [56]. Actually, these fitting parameters are comparable with the parameters for  $WS_2$  monolayers obtained by mechanical exfoliation from a bulk crystal and without any strain [130]. However, some discrepancies also exist between the parameters. First,  $E(0)$  values differ about 42 meV. Second, the  $A^0$  exciton peak position found from PL measurements has slightly different behavior, see Fig. 3.8(a). At lower temperatures, the separation between  $A^0$  exciton peaks measured using reflectance contrast (absorption) and PL is increasing, and this is



typical for localized excitons, where the temperature dependence of peak position often exhibits an S-shape behavior [131], [132].

Figure 3.8(b) shows the temperature dependence of the full width at half maximum (FWHM) of A-exciton line found from the reflectance contrast and PL spectra. The linewidth broadening of the A-exciton for RC band was fitted using the linewidth broadening relation proposed by Rudin *et al.* [133]:

$$FWHM(T) = W_0 + \beta T + \gamma/[\exp(\hbar\omega_{LO}/kT) - 1], \quad (4)$$

where  $W_0$  is a width at  $T = 0$  K including also inhomogeneous broadening,  $\beta$  is a coefficient for the interaction of excitons with acoustic phonons and the last term represents the interaction with LO (longitudinal optical) phonons,  $\hbar\omega_{LO}$  is the LO-phonon energy. The LO-phonon energy is taken equal to 44.6 meV for WS<sub>2</sub> [134]. The fitting result is presented in Fig. 3.8(b) as a red curve and the fitting parameters are shown in Table I. At higher temperatures ( $T > 150$ K) the FWHM of PL band also shows widening due to electron-phonon interaction, but the width of the PL band seems to be smaller than for RC band. This difference is related to the fact that the PL spectrum does not represent the total exciton density of states because the photoexcited carriers undergo relaxation processes before they recombine radiatively. Therefore, the PL spectrum corresponds to the distribution of the lowest exciton energy states while the reflectance contrast spectrum represents the distribution of all exciton states. However, at temperatures  $T < 150$ K, the width of the PL band starts to increase rapidly with the decreasing of temperature. Moreover, the shape of the PL band near the peak maximum changes and becomes wider, see Fig. 3.8 (b). This behavior is again typical for localized excitons [135].

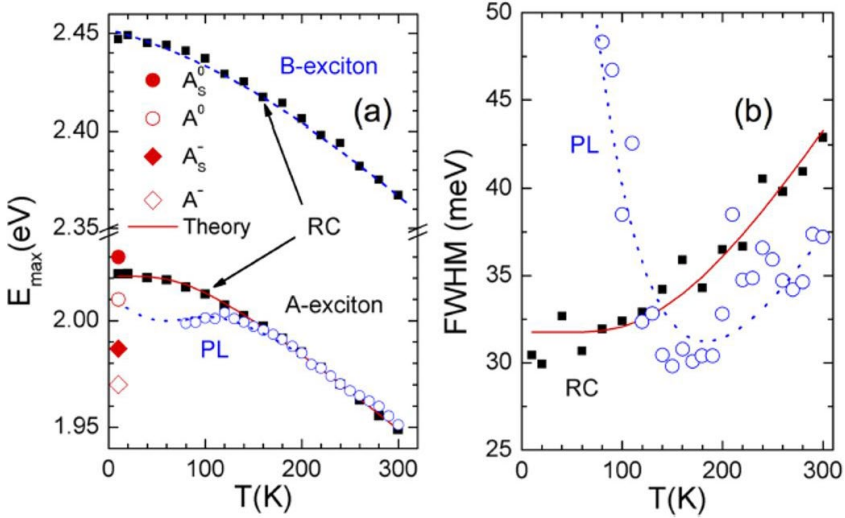


Figure 3.8: (a) Temperature dependence of the PL peak energy (blue circles) and peak position of reflectance contrast (RC) spectra (solid squares). Fitting result using Eq. 3 is given with red curve. Peak positions of different PL peaks at  $T = 10$  K are also indicated. (b) Temperature dependence of FWHM of A<sup>0</sup>-exciton peak obtained from RC (solid squares) and PL spectra (circles). Red curve represents the fitting with Eq. 4 (Figure 7 in [1])

Table 3.1. Fitting parameters as obtained from fitting of the temperature dependence of  $E_{max}$  and FWHM (RC spectra) for  $A^0$ -exciton peak using Eq. 3 and Eq. 4. Fitting results from ref. [130] are given in parentheses.

Fitting equation	Parameter	Value
Eq. 3	$E(0)$ (eV)	2.021 (2.063)
	S	2.23 (2.4)
	$\hbar\omega$ (meV)	22.7 (31)
Eq. 4	$\gamma$ (meV)	53.2
	$\hbar\omega_{LO}$ (meV)	44.6
	$W_0$ (meV)	31.8

A general model for the luminescence of localized-state ensemble (LSE) was given by Li *et al.* [135] According to this work, the shape of the PL band for localized excitons is asymmetric and can be calculated using the density of states function for excitons  $\rho(E)$  and a distribution function  $f(E, T)$  for localized carriers. The  $f(E, T)$  function has a shape resembling a Fermi distribution with a characteristic energy  $E_f$ . The distribution of the localized states  $\rho(E)$  is usually assumed to be described by a Gaussian-like function, but other shapes are also possible. In Ref. [84], for example, the Lorentzian shape was used. According to Ref. [135], the low-energy side of PL band is less affected by the distribution function  $f(E, T)$  and therefore the shape of this side gives a clue about the shape of the  $\rho(E)$  function. In our case, it is reasonable to approximate the function  $\rho(E)$  by a hyperbolic secant, because this function is the most suitable one for PL band shape fitting. Then the overall shape of the localized exciton PL band is given by:

$$I(E, T) = A(T)\rho(E)f(E, T) = \frac{A(T)\rho_0 \operatorname{sech}\left[\frac{E - E_0}{\sigma}\right]\left(\frac{\tau_{tr}}{\tau_r}\right)}{\exp\left[\frac{E - E_f}{kT}\right] + \frac{\tau_{tr}}{\tau_r}}, \quad (5)$$

where  $A(T)$  is a temperature-dependent term,  $\rho_0$  is the amplitude,  $E_0$  is the peak position and  $\sigma$  is the width of the density of states function,  $1/\tau_r$  and  $1/\tau_{tr}$  represent the rate of radiative recombination and the attempt-to-escape rate of the localized carriers, respectively. The shape calculated by Eq. 5 can be quite well fitted using an asymmetric hyperbolic secant function. At the same time, the shape and the temperature dependence of the peak position  $E_{max}$  and FWHM of localized exciton band significantly depend on  $E_0$  and  $E_f$ . In many cases [135], the best correlation with experimentally measured temperature dependencies is obtained by taking  $E_0 > E_f$ . Figure 3.10(a) shows PL spectra calculated by using Eq. 5 for the case  $E_0 - E_f = 20$  meV,  $\sigma = 6$  meV and  $\tau_{tr}/\tau_r = 0.1$  and in Fig. 3.9(b), the temperature dependencies of peak position  $E_{max} - E_0$  and FWHM are given. It can be seen that the shape of the calculated PL band shows very similar behavior to what was observed experimentally, see Figs. 3.7–3.9. At temperatures  $T < 150$  K, we see a rapid increase of FWHM and a gradual redshift of the peak position. Furthermore, the shape of the PL band near the peak maximum becomes wider and the same trend was observed experimentally, see Fig. 3.7(b). This means that the LSE model applies to the aged  $WS_2$  monolayer and spatial fluctuations of the bandgap energy due to local strain will induce this localization in the lowest-energy regions, where the excitons will be swept by the strain-induced potential gradient and funneled toward the center [136]. An LSE model was previously proposed also for  $WS_2$  monolayers grown on a silicon substrate in a hot-wall furnace,

where the room temperature PL peak has a maximum at about 1.955 eV [137]. One potential source of the local strain is associated to the relatively high nanocaps found by AFM scan on the surface of the WS<sub>2</sub> monolayer, see Fig. 3.5(c). The average distance between these nanocaps is less than the diffusion length of excitons in WS<sub>2</sub> monolayers ( $\sim 350$  nm [138]) and therefore excitons can be easily captured in these regions with high strain and reduced band gap energy. The possible strain  $\varepsilon$  for these nanocaps was obtained from the curvature of the nanocaps using the pure-bending equation  $\varepsilon = (d/2)/(R - d/2)$ , where  $R$  and  $d$  are the radius of curvature and the thickness of WS<sub>2</sub> monolayer, respectively [139]. Taking the average thickness of the monolayer  $d = 0.8$  nm, height  $h = 7$  nm and the diameter  $a = 30$  nm of nanocaps, the tensile strain value will be  $\varepsilon = 2.1\%$  and, according to the experimentally determined peak position shift of  $-11.3$  meV per % of strain [75], the overall peak position shift is 23.7 meV. This obtained value is in good correlation with the A<sup>0</sup>-exciton peak position separation between as-grown and aged WS<sub>2</sub> monolayers, see Fig. 3.5(b). At low temperatures, we also detected additional exciton A<sub>S</sub><sup>0</sup> and trion A<sub>S</sub><sup>-</sup> peaks at higher energies, see Fig.3.6(a). The position of these peaks suggests that they are also related to strained areas, where the band gap energy is about 4 meV less than in as-grown monolayers. This energy corresponds to the strain value of  $\varepsilon = 0.35\%$  and this strain could be caused by the general increase of the surface roughness in aged monolayers. These states are very shallow, and excitons are easily thermalized into deeper states when the temperature is increased. The whole aged monolayer surface is thus disturbed by the strain having slightly different origin (increased surface roughness vs. nanocaps) and values and therefore we could see emission from localized states only. The recombination model for excitons and trions in aged WS<sub>2</sub> monolayer is given in Fig. 3.10. At low temperatures, the exciton and trion recombination is possible from both deep  $\rho_D$  and shallow  $\rho_S$  localized states showing double peak structure. At higher temperatures, only  $\rho_D$  states are active. According to our calculations  $\varepsilon_D = 24\text{meV}$  and  $\varepsilon_S = 4$  meV.

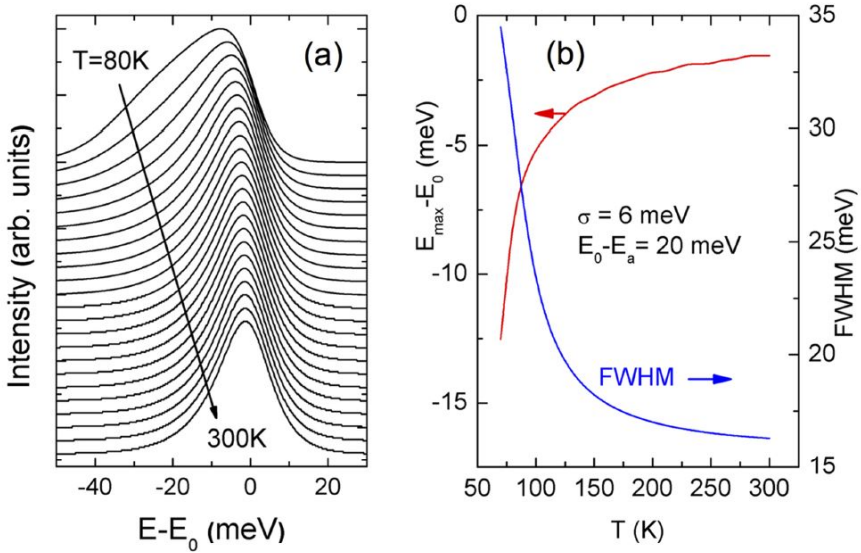


Figure 3.9: (a) Calculated temperature dependence of the luminescence peak shape (normalized) for the case of  $E_0 - E_a = 20$  meV and  $\sigma = 6$  meV using Eq. 5, (b) the temperature dependence of peak position (red) and FWHM (blue). (Figure 8 in [1])

The origin of the nanocaps in the aged monolayer is not clear. It was shown in Ref. [81] that aging usually leads to oxidation of metal states and this process is more prominent at grain boundaries. Sulfur vacancies are similarly believed to play an important role in these oxidation processes. It is also possible that very small nanoparticles were formed on a Si/SiO<sub>2</sub> surface during growth and they are not completely reacted in S atmosphere. Similar nanoparticles were found in many monolayers where they acted as seeds for CVD monolayer growth [140]. During aging, these nanoparticles beneath the monolayer start to expand due to oxidation and, as a result, nanocaps are formed. However again, the true origin of these nanocaps is a topic of future studies.

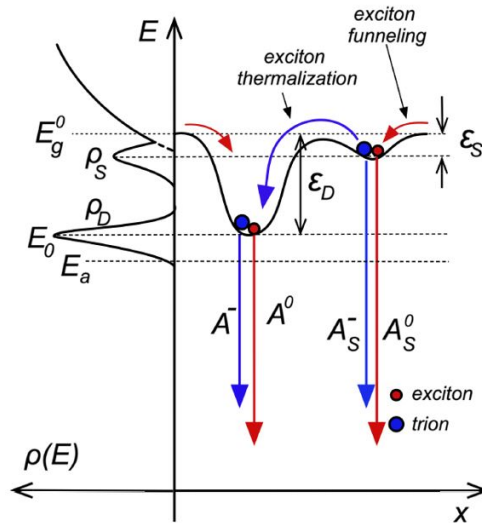


Figure 3.10: Proposed recombination model for localized excitons and trions in aged WS<sub>2</sub> monolayers. Density of deep  $\rho_D$  and shallow  $\rho_S$  localized states are shown. The origin of double PL peaks is explained. (Figure 9 in [I])

### 3.3 Tailoring of bound exciton photoluminescence emission in WS<sub>2</sub> monolayer

This section presents a PL study of bound exciton emission in CVD grown WS<sub>2</sub> monolayers and is based on the results published in the paper [III]. Most of the WS<sub>2</sub> monolayers grew in the form of triangular islands with domain sizes up to several tens of micrometers. However, other shapes were also observed, for example, in Fig. 3.11(a), a scanning electron microscope (SEM) image of butterfly-like WS<sub>2</sub> monolayer is presented. The diameter of this monolayer is about 40  $\mu\text{m}$ . Butterfly-like shaped WS<sub>2</sub> monolayers have been seen previously in several studies [20], [46], [141]. These kinds of monolayers are reported to consist of two symmetrical wings with different atomic orientations, separated by a grain boundary [20]. The grain boundary usually includes multiple different misaligned atoms, creating extended defects in the material. The grain boundary area in the middle of the butterfly-shaped WS<sub>2</sub> monolayer is of particular interest, and therefore, this flake was chosen for further studies. To confirm the high concentration of defects in the grain boundary, a room-temperature PL map from the

monolayer was created. In Fig. 3.11(b), the PL peak position map of the  $A^0$  (neutral A exciton) peak is presented, showing the redshift of the  $A^0$  peak in the middle of the flake. It was shown that the high concentration of defects [142] and a possible tensile strain are the main reasons for this kind of peak shift of  $A^0$  excitons in different TMD monolayers, as we have seen in the previous section and in [84], [89]. In Fig. 3.11(c), two low-temperature ( $T = 15$  K) PL spectra from different regions are presented and a region with a high-intensity defect-bound exciton PL emission is chosen for further studies and the results are presented below.

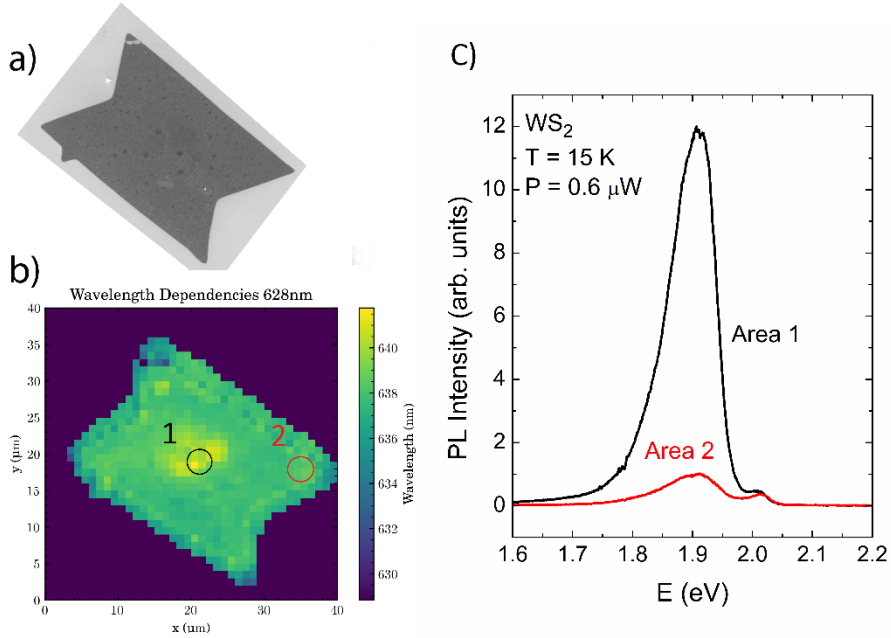


Figure 3.11: (a) SEM picture of a butterfly-shaped  $WS_2$  monolayer. (b) 2D PL map showing the redshift of the  $A^0$  exciton peak in the middle of the flake. (c) Low-temperature ( $T = 15$  K) PL spectra from different  $WS_2$  monolayer areas marked as 1 and 2 in (b). (Figure 1 in [III])

The room-temperature PL spectrum of this defective region shows only one asymmetrical  $A^0$ -exciton peak at  $E_{max} = 1.940$  eV (Fig. 3.12(a)). The peak is shifted to lower energy by about 80 meV when compared to mechanically exfoliated  $WS_2$  monolayers [54]. In the previous section, we observed an asymmetrical  $A^0$  exciton peak at 1.951 eV in aged CVD-grown  $WS_2$  and showed that it was redshifted due to tensile strain. The intensity of the  $A^0$  peak from our butterfly-shaped layer was around 100 times higher than the intensity of the  $A^0$  peak measured from the double-layered  $WS_2$ , confirming that the  $WS_2$  flake studied here is indeed a monolayer.

The Raman spectrum from the CVD-grown  $WS_2$  together with the fitting results is presented in Figure 3.13(a). From the fitting, the positions of the main peaks, the in-plane mode  $E_{2g}^1(\Gamma)$  at  $355.0$   $cm^{-1}$  and the out-of-plane mode  $A_{1g}(\Gamma)$  at  $418.3$   $cm^{-1}$ , were determined. The separation between these peaks is  $\Delta = 63.3$   $cm^{-1}$ . This value is somewhat higher than normally observed in  $WS_2$  monolayers with better quality, where the separation is usually in the range  $\Delta = 61.5$ – $62.4$   $cm^{-1}$  [50], [123], [141], [143]. It is known that the tensile strain in  $WS_2$  monolayers grown on the Si/SiO<sub>2</sub> substrate causes the

in-plane Raman mode  $E_{2g}^1(\Gamma)$  to redshift more than the  $A_{1g}(\Gamma)$  peak [144], which increases the separation between these peaks. The dominating mode in Figure 3.13(a) is  $2LA(M)$  ( $350.2\text{ cm}^{-1}$ ) that has approximately three times the intensity of the  $A_{1g}(\Gamma)$  mode, which is characteristic for the Raman spectra of  $\text{WS}_2$  monolayers, measured with green laser excitation (514 nm [50], 532 nm [145]). This fact and the peak separation value confirm once again that the studied butterfly-like flake is indeed a monolayer. Raman spectra show no dependence on the position on the flake, which indicates the same strain value throughout the flake.

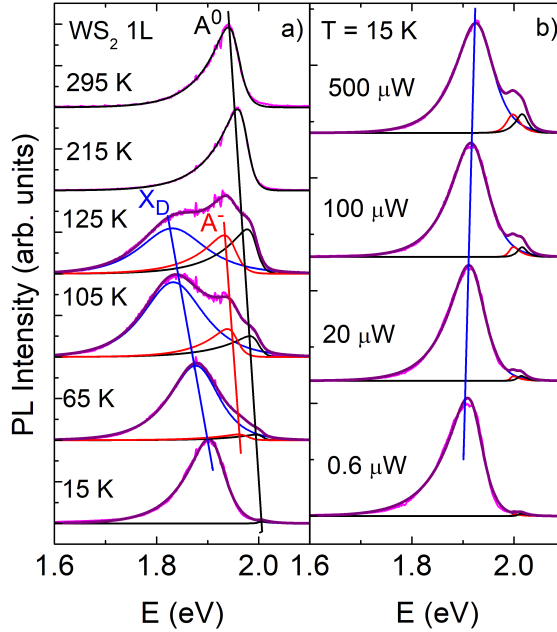


Figure 3.12: Normalized (a) temperature and (b) laser power dependencies ( $T = 15\text{ K}$ ) of the PL spectrum of a  $\text{WS}_2$  monolayer (purple lines). PL-fitting results with asymmetric hyperbolic secant functions (Eq. 2) are shown. Blue lines show the fitting results for the defect-bound exciton peak  $X_D$ , red lines for the trion peaks  $A^-$ , and black lines for the exciton peaks  $A^0$ . (Figure 2 in [III])

All PL spectra were fitted using an asymmetric hyperbolic secant function (Eq. 2). This function has been also used in Section 3.2 to fit the PL spectra of  $\text{WS}_2$  monolayers as well it has been used to fit excitonic PL bands in  $\text{MoSe}_2$  [127] monolayers.

Low laser excitation power ( $5\text{ }\mu\text{W}$ ) was chosen for the temperature-dependent PL measurements ( $T = 15 - 295\text{ K}$ ) to have a more pronounced defect-bound exciton band  $X_D$ , compared with the exciton  $A^0$  and trion  $A^-$  peaks (see Fig. 3.12(b)). The temperature dependence of some characteristic PL spectra is presented in Fig. 3.12(a). An asymmetrical  $A^0$  peak can be seen for the whole temperature range, although at low temperatures, it is relatively weak compared to the  $X_D$  band. The trion peak  $A^-$  appears at  $65\text{ K}$  and disappears above  $205\text{ K}$  (Fig. 3.13(b)). The  $X_D$  emission band shows an asymmetric lineshape with a sharper high-energy cut-off and an exponential low-energy tail. This band is thermally quenched with increasing temperature and becomes invisible at temperatures above  $180\text{ K}$ , as shown in Fig. 3.13(b). Moreover, the  $X_D$  band shows a redshift with

increasing temperature and this shift is larger for the exciton and trion peaks, see Fig. 3.13(b). The redshift of the  $A^0$  and  $A^-$  peaks with increasing temperature follows the same trend as the exciton peak in strain-free mechanically exfoliated  $WS_2$  monolayers [54] shown as a reference in Fig. 3.13(b). A similar temperature dependence of the  $A^0$  peak position was found also in the study by Gu *et al.* [145].

The fitting of the PL spectra measured at different temperatures revealed that the width related to the low energy side  $W_{LE}$  of the  $X_D$  band exhibits only a very weak increase with temperature (Fig. 3.13(d)), whereas the width related to the high energy side  $W_{HE}$  shows a clear temperature dependence. All these features observed for the  $X_D$  band are usually considered as evidence of disorder-related effects and are also typical for highly doped semiconductors like  $CuInGaSe_2$  [146] or  $Cu_2ZnSnSe_4$  [147]. As the random fluctuations of defect concentration or strain can cause band gap and electrostatic potential fluctuations, they may smear the band edges and form exponential tails of the density of states extending into the band gap. At low temperatures, excitons can be trapped by the localized states at the band tails, leading to the observed asymmetric lineshape of the PL spectra. In this case, the low-energy tail of the PL band reflects the energy distribution of the density of states within the band tail and has a very weak temperature dependence [146], [148]. At the same time, the high-energy side usually shows a typical broadening with increasing temperature [146], see Fig. 3.13(d). We therefore conclude that the  $X_D$  band is related to the deep defect states within the band gap and that the PL emission is caused by the excitons bound to these deep defects.

From the temperature dependence of the integral intensity, the thermal activation energy  $E_a = 33 \pm 4$  meV was determined for the defect-bound exciton  $X_D$  (Fig. 3.13(c)) using the following equation [149]:

$$\phi(T) = \phi_0 / [1 + A_1 \exp(-E_a/kT)], \quad (6)$$

where  $\phi$  is the integral intensity of the PL band,  $A_1$  is the process rate parameter and  $E_a$  is the thermal activation energy. A similar activation energy for the defect-bound exciton has been found not only in  $WS_2$  [150], but also in other TMDs like  $WSe_2$  [90], [151] and  $MoS_2$  [152]. When the temperature increases, bound excitons can be thermally activated into delocalized states and captured by the competing nonradiative recombination channels or recombine as free excitons. Therefore, it is expected that the intensity of the bound exciton emission decreases monotonically with increasing temperature. The carriers localized at shallow defect states are first thermally activated to the deeper states, leading to the redshift of  $X_D$  with increasing temperature. Correspondingly, at low temperatures, the increasing excitation intensity is expected to cause band filling of the deeper localized energy states, giving rise to a blueshift of the  $X_D$  emission.

The laser excitation power dependence of the PL spectrum was measured at a low temperature ( $T = 15$  K) in the range of  $P = 0.6 - 500$   $\mu$ W to study the nature of radiative recombination processes. In Fig. 3.12(b), the power series of the PL spectra are shown and it can be seen that the defect band  $X_D$  strongly dominates over the exciton and trion peaks especially at low laser powers. Furthermore, the  $X_D$  peak energy increases with increasing laser power (a straight blue line in Fig. 3.12(b)), confirming the expected blueshift caused by band-filling effects.

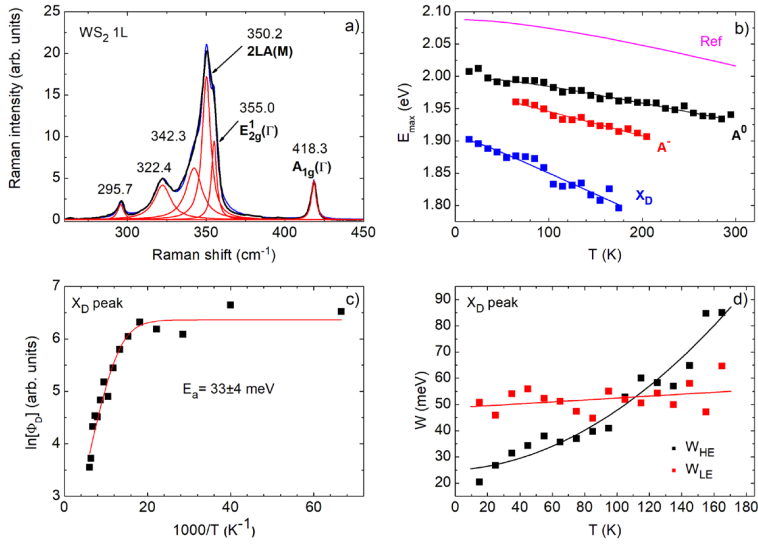


Figure 3.13: (a) Raman spectrum from the  $WS_2$  monolayer. Red lines show the result of spectral fitting with Lorentzian curves. The blue line presents the cumulative fitting result. (b) Temperature dependence of the PL peak energies. Magenta line represents a temperature dependence of the  $A^0$  peak taken from the study by Plechinger et al. [54] (c) Arrhenius plot showing the activation energy of the  $X_D$  band using Eq. 6 (d) The width of high ( $W_{HE}$ ) and low ( $W_{LE}$ ) energy sides of the  $X_D$  band as a function of temperature. The lines are least squares fit to the data. (Figure 3 in [III])

The integrated PL intensity  $\Phi$  versus the laser excitation power  $P$  usually follows a power law dependence:  $\Phi \approx P^k$  [118]. The integrated PL intensity  $\Phi$  as a function of the excitation power  $P$  was investigated for all emission bands at  $T = 15$  K, see Fig. 3.14(a). Both the exciton and trion peaks ( $A^0$ ,  $A^-$ ) show nearly linear dependence ( $k \approx 0.9$ ), whereas the emission from the defect-bound exciton band  $X_D$  shows a different dependence and saturates at high excitation powers. It is also observed that the  $X_D$  band blueshifts as the excitation intensity increases and the rate of this shift is about 15 meV per decade of laser power (Fig. 3.14(b)). This kind of blueshift is usually considered as the evidence of disorder-related effects in semiconductors [89], [146], [153]. We showed before that the random fluctuations of defect concentration or strain can cause band gap and potential fluctuations and form exponential tails in the density of localized states extending into the band gap. At low temperatures, the increasing excitation intensity will cause band filling of the localized energy states, giving rise to the blueshift of  $X_D$  emission.

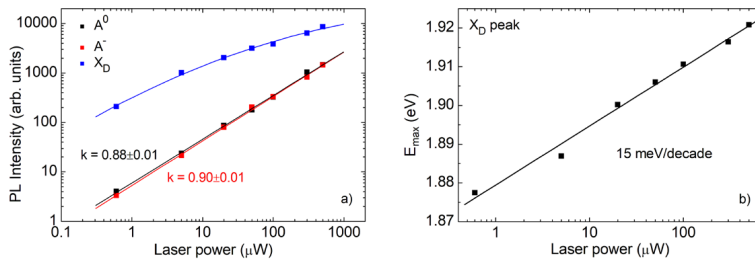


Figure 3.14: (a) Integrated PL intensity  $\Phi$  of different PL bands as a function of the laser power, plotted on a log–log scale. The lines are the least squares fit to the data. (b)  $X_D$  peak position dependence of the laser power. The line is the least square fit to the data. (Figure 4 in [III])



It was shown theoretically that the PL intensity of the exciton-like transition should follow a power law  $\Phi \approx P^k$  with  $k \approx 1$ . A value  $k \ll 1$  indicates a recombination involving defect states [118]. However, the sublinear increase of the intensity of  $X_D$  band with laser power can be explained by the limited concentration of these deep defects leading to the saturation of the intensity of the  $X_D$  band at higher laser powers. A high concentration of deep defects usually leads to a steeper increase of the PL intensity reflected by higher values of  $k$ , as reported by different research groups, see for example the study by Shang *et al.* [154]. Different  $k$  values for the defect band have been observed also in other materials like  $WSe_2$  [90], [151] and  $MoS_2$  [62]. The sublinear dependence of the  $X_D$  band intensity in TMD monolayers has been shown also in the previous section and in  $MoS_2$  [128].

The nature of these deep defects is not clear, but our experiments have shown that by using laser annealing, it is possible to reduce the intensity of the  $X_D$  band. The studied  $WS_2$  monolayer was annealed with a focused laser beam with  $P = 1500 \mu W$  (power density  $\approx 5 \times 10^8 W/m^2$ ) for 5 min at a low temperature ( $T = 15 K$ ). To study the effect of annealing, the PL spectra with a laser power of  $0.6 \mu W$  before and after annealing were compared. Such a low excitation power was used, because the  $X_D$  band was found to be more pronounced when compared to  $A^0$  peak at low laser powers as shown in Fig. 3.12(b). Laser irradiation was found to reduce the relative intensity of the defect-bound exciton band about ten times compared to the  $A^0$  exciton peak intensity, indicating that this type of annealing removes some physisorbed gas atoms from the  $WS_2$  monolayer surface. This effect is rather interesting, suggesting that  $X_D$  band can be sensitive also to other forms of radiation, being useful for some applications. Similar effects have been observed also by other groups [82], [85].

The most probable intrinsic defect in the  $WS_2$  monolayer could be a sulfur vacancy,  $V_s$ , with a reported depth of about  $0.47\text{--}0.6 eV$  from the conduction band edge [155]–[157]. At the same time, grain boundaries and adsorbed atoms or molecules on the surface can also play an important role.

### 3.4 The effect of elevated temperatures on excitonic emission and degradation processes of $WS_2$ monolayer

Studied  $WS_2$  in this section were synthesized in University of Duisburg-Essen, Germany, via the CVD method and the results on which this section is based on are published in paper [IV].  $WS_2$  monolayers were grown in a variety of different shapes with the average domain size around  $100 \mu m$ . The  $WS_2$  monolayers were grown on  $Si/SiO_2$  substrate. The thickness of  $WS_2$  monolayer was determined to be about  $0.8 nm$ , which is typical for TMD monolayers (Fig. 3.15 (a) and (b)) [97]. Another method to support this finding by initial optical characterization is Raman spectroscopy. A Raman spectrum was measured from area 2 (marked in Fig. 3.17) and the results are presented in Fig. 3.15 (c). Raman spectrum was fitted using Lorentzian curves and the peak positions of the main peaks, the in-plane mode  $E_{2g}^1(I)$  at  $357.6 cm^{-1}$  and out-of-plane mode  $A_{1g}(I)$  at  $419.6 cm^{-1}$  were determined. The separation between these peaks is  $\Delta = 62.0 cm^{-1}$  and this value is in the same range as the separation values ( $\Delta = 61.5 - 62.4 cm^{-1}$ ) found in good quality  $WS_2$  monolayers [50], [123], [141], [143]. Additionally, the dominating mode is a second-order contribution ( $2LA(M)$ ) at  $352.7 cm^{-1}$ , as is typical for measurements on  $WS_2$  monolayers under near-resonance condition [50]. All these results confirm that the further studied  $WS_2$  flakes were indeed monolayers.

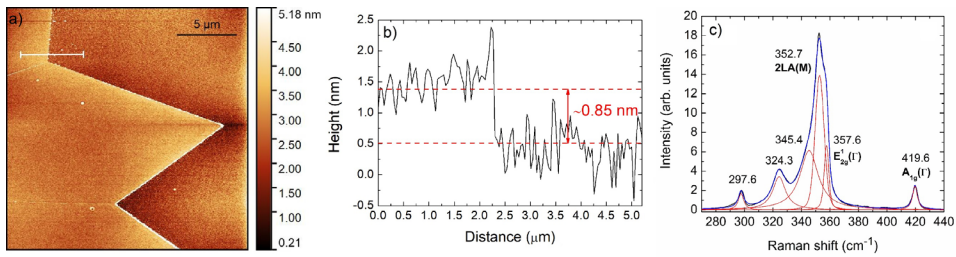


Figure 3.15: AFM height image (a) and AFM line profile (b) showing typical  $WS_2$  monolayer thickness. The line profile was taken along the white line shown in (a). Raman spectrum (c) from the  $WS_2$  monolayer. Red lines show the result of spectral fitting using Lorentzian curves. (Figure 1 in [IV])

In Fig. 3.16(a) a PL image of a  $WS_2$  polycrystalline monolayer flake is given and in Fig. 3.16(b) a PL image of the same flake is given, after heating it in an Ar atmosphere up to  $T = 643$  K. It illustrates the formation of cracks along the grain boundaries, although  $WS_2$  flakes started to be thermally unstable already at around  $T = 573$  K, as was seen in the optical microscope. The different thermal expansion rates of the substrate and  $WS_2$  monolayer can be one reason for this cracking [47]. However, this should not have such a big impact, as the CVD growth temperature is  $T = 1073$  K, and the material can indeed handle the temperature difference between growth and room temperatures. From that knowledge, the stress at  $T = 573$  K should not have such an effect. Nevertheless, defects at grain boundaries can affect the material loss and this phenomenon has been detected previously in  $MoS_2$  monolayers heated in air [100].

As illustrated in Fig. 3.16, grain boundaries and their degradation at higher temperatures can have a crucial influence on the PL emission. Consequently, an equilateral triangular-shaped single-layered  $WS_2$  flake was chosen for further PL studies and it is illustrated in Fig. 3.17. These types of flakes are monocrystalline and without visible grain boundaries. Which is not the case with other shapes, in which the original monocrystalline flakes have ripened into a larger irregular structure with internal grain boundaries [158]. The later discussed PL temperature dependence study was carried out with a  $10\times$  objective ( $NA = 0.25$ ). This objective has the largest laser spot, so it can cover a maximum area and thus the spatial variations in the flake are averaged with the surrounding region (see area 1 in Fig. 3.17(a)). After the temperature dependence study, only part of the material was still intact (Fig. 3.17(b)) and to study the PL response of the intact monolayer, a  $50\times$  objective ( $NA = 0.50$ ) was used (see area 2).

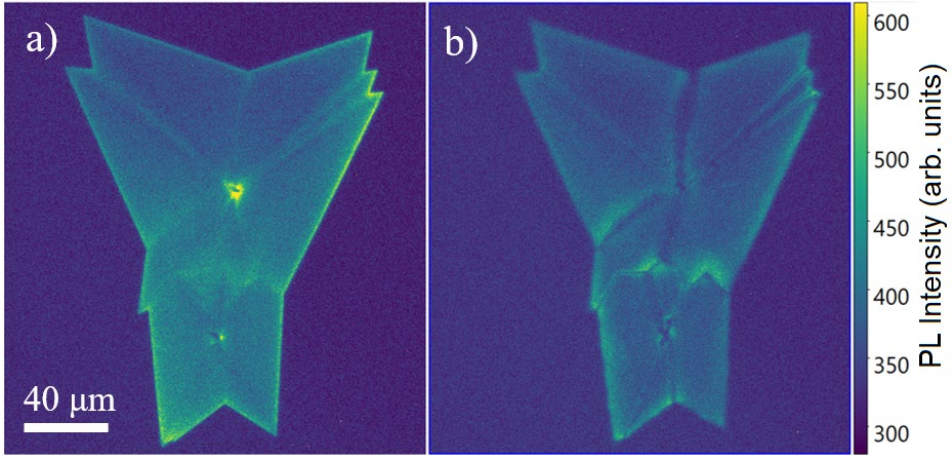


Figure 3.16: PL images of the same flake before (a) and after (b) heating the sample up to  $T = 643$  K. Cracking can be observed at the grain boundaries. (Figure 2 in [IV])

The initial room temperature PL image in Fig. 3.17(a) shows that the PL intensity across the monolayer is nonuniform. It has been reported previously in [78], that the center of the crystal shows lower PL intensity than the areas close to the edges, with this region of lower intensity also extending symmetrically from center towards the vertices.

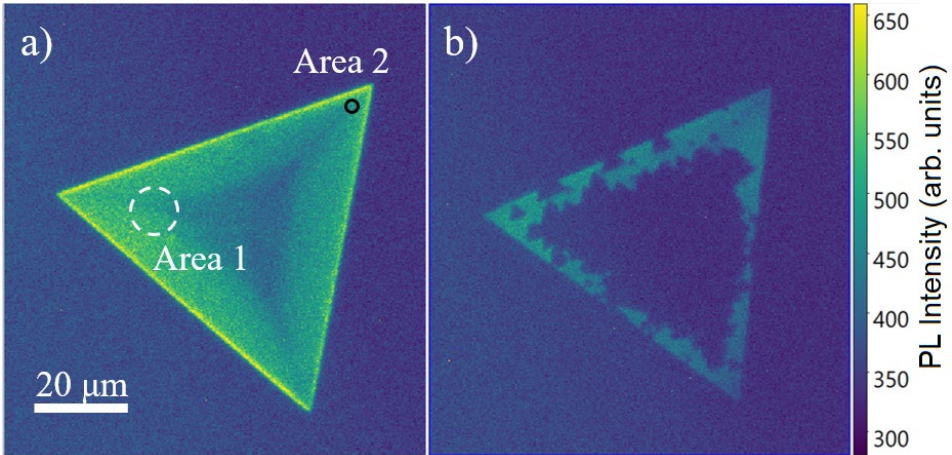


Figure 3.17: PL images of the same flake before (a) and after (b) it was used to study temperature-dependent PL at elevated temperatures. Area 1 and Area 2 are representing the approximate laser spot size and placement of 10x objective and 50x objective, respectively. (Figure 2 in [IV])

The temperature dependence measurements were carried out in the following temperature range  $T = 303 - 723$  K. The temperature dependence of some PL spectra is presented in Fig. 3.18(a). All temperature-dependent PL spectra had an asymmetrical shape and were fitted using Split Pearson VII function, because this function gave the best fitting result [159]. The fittings are also shown in Fig. 3.18(a). The laser power used for temperature-dependent measurements was 0.42 mW. The asymmetrical A exciton peak can be observed in the whole temperature range, but with the increasing temperature

the peak intensity was decreasing, which is in contrast with refs. [92] and [93]. While the peak intensity was decreasing, the peak position was seen to redshift and full width at half maximum to broaden. The temperature dependence of the A exciton peak position is linear and has a trendline equal to  $dE_{max}/dT = -0.358 \pm 0.003$  meV/K (see Fig. 3.18(b)).

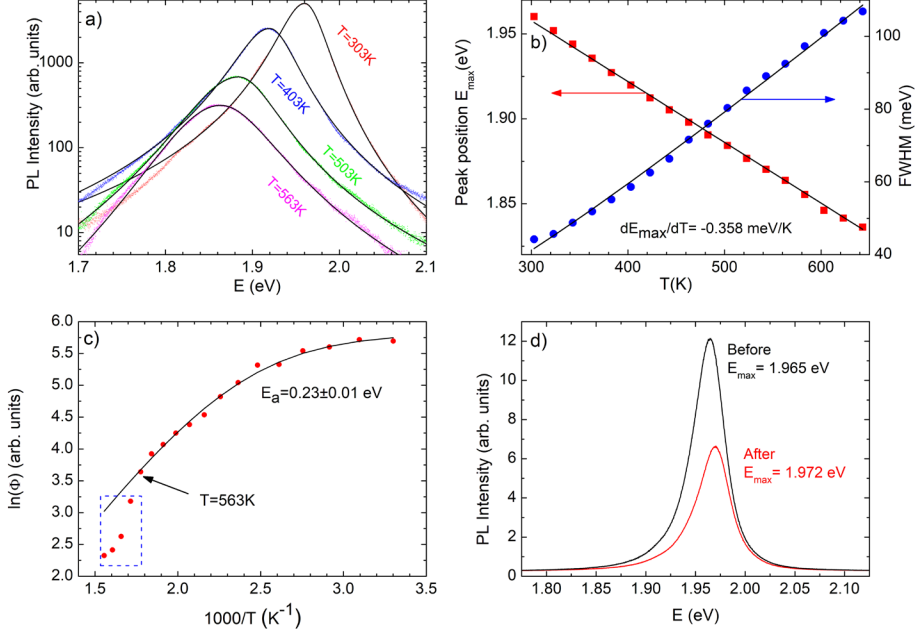


Figure 3.18: (a) Temperature dependent PL spectra of WS<sub>2</sub> monolayer. PL fittings using Split-Pearson-VII function are shown as black lines. (b) Temperature dependence of exciton peak energy (red dots) and FWHM of the exciton peak (blue dots). The exciton peak energy dependence is fitted with linear and FWHM dependence is a result of fitting with Eq. 4. (c) Arrhenius style plot showing the thermal activation energy of the A exciton peak. Fitting result using Eq. 6 is given as a continuous line. Blue rectangle is showing the additional intensity decrease due to material decomposition. (d) Room temperature PL spectra from area 2 of Fig. 3.17(a) of the flake before and after heating up to  $T = 723$  K. (Figure 4 in [IV])

Next, the temperature dependence of the FWHM was fitted using Eq. 4. The interaction with acoustic phonons was neglected because it usually very small [160]. The fitting result is presented in Fig. 3.18(b) and the fitting parameters are following  $W_0 = 16.5 \pm 0.8$  meV and  $\gamma = 113.9 \pm 1.6$  meV. The FWHM of the exciton peak increases in the whole temperature range due to interactions with LO phonons.

Afterward, the thermal activation energy of WS<sub>2</sub> exciton emission was determined to be  $E_a = 0.23 \pm 0.01$  eV and it is illustrated in an Arrhenius style plot in Fig. 3.18(c). The thermal activation energy was found using the Eq. 6. For the calculation of the thermal activation energy, only temperatures up to  $T = 563$  K were included, because at temperatures above  $T = 563$  K we noticed an additional drop of PL intensity due to the decomposition of the WS<sub>2</sub> monolayer (the additional PL intensity loss due to material loss is marked with the blue rectangle in Fig. 3.18(c)). Similar activation energies have been found in WS<sub>2</sub> grown on Si/SiO<sub>2</sub> ( $E_a = 0.40$  eV [77] and  $E_a = 0.53$  eV [161]) and on sapphire ( $E_a = 0.20$  eV [77]).

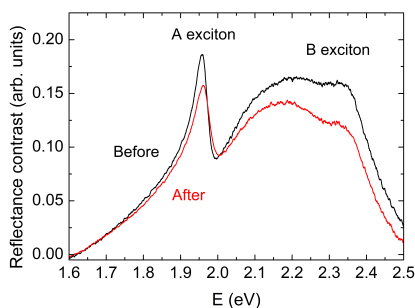


Figure 3.19: Room temperature RC spectra from  $WS_2$  flake before and after heating up to  $T = 723$  K. (Figure 5 in [IV])

Room temperature PL was measured from area 2 (marked in Fig. 3.17(a)) before and after heating up to  $T = 723$  K. Area 2 is in the region that has not undergone apparent thermal decomposition and the results are presented in Fig. 3.18(d). The PL intensity at room temperature following the high temperature measurements remained in a similar range as before, although the intensity has reduced by a factor of two. This indicates that the still intact  $WS_2$  monolayer is stable against temperature variations and largely maintains its previous properties. This suggests that the temperature does not have an irreversible effect on the remaining monolayer.

Another method to confirm that the temperature does not affect the intact material significantly is the Raman spectroscopy. The Raman spectrum was measured after heating up to 723 K from the same area as the spectrum in Fig. 3.15(c) and shows a peak separation of  $\Delta = 61.9$   $cm^{-1}$  and the shape of the spectrum remained the same, confirming that the quality of the remaining monolayer is maintained. Additionally, reflectance contrast measurements can be also used to further study the quality of  $WS_2$  monolayer. RC spectra measured before and after heating ( $T = 723$  K) are presented in Fig. 3.19. It shows that the shape and intensity of the A- and B-exciton bands remain relatively unchanged after thermal treatment.

From Fig. 3.17(b), it seems that the remaining  $WS_2$  monolayer is concentrated near the edges of a triangle, while the central part of the triangle mostly is degraded. It is also interesting to note that the part near the edges of the flake exhibited a greater room temperature PL intensity compared to the central part of the monolayer. This means that the central part of the triangle, which has lower PL intensity, is also decomposing faster at high temperatures than the brighter part of the flake. It may be that the middle area of the triangle has more defects, which are non-radiative [78], and that this is the reason for material loss. Moreover, our measurements showed that the PL band from the middle area of the as-grown flake was also red shifted about 4 meV when compared to the edge region of the flake. This red shift of the exciton band in CVD grown monolayers is related to the slightly higher value of tensile strain, as has already been illustrated in Fig. 3.11. It is possible that the increased strain is also playing an essential role in the more rapid thermal decomposition of the central part of the flake. This is further corroborated by the polycrystalline flake (Fig. 3.16), which has the most significant material loss starting at the grain boundaries, although this flake was exposed to even lower temperatures ( $T = 643$  K). However, the remaining part of the triangular monolayer does also include some small holes, where the material has degraded. These holes have a triangular shape

and are probably related to point defects. The intrinsic defects in as-grown  $\text{MoS}_2$ , including grain boundaries and point defects as starting points for degradation is discussed also by Chen *et al.* [162]. Specifically, areas with higher defect density have larger concentrations of dangling bonds and consequently greater reactivity. Moreover, it was noticed that triangular holes due to point defects have opposite orientation to the parent crystal. This can also be observed in our case (see Fig. 3.17(b)). The PL peak position after high temperature handling had a small blueshift of 7 meV, which may be related to strain release [75], as the material loss and geometry change of the flake can affect the strain inside the flake. The same small blueshift of the A-exciton can be observed also in the RC spectrum after high-temperature handling, see Fig. 3.19.

It is also noteworthy that while the first apparent material loss was detected in the optical image at  $T = 603$  K, it is evident from the spectroscopy data that the initial degradation begins at around  $T = 563$  K. The intensive material loss after high temperature treatment is visible in Fig. 3.17(b), in which only some areas of the original triangle are still present.

AFM was used to further study the intact monolayer, with the results presented in Fig. 3.20. The height and phase scans (Fig. 3.20(a and b) respectively) show that the holes inside the material are indeed of triangular shape. Furthermore, the inside of the triangle (right side of Fig. 3.20(a)) includes areas with large aggregations of material. According to the phase image, these regions are not crystalline  $\text{WS}_2$ , a finding that is further confirmed by Fig. 3.17(b), as these regions are not seen to emit PL. As such, they may be collections of amorphous material consisting of decomposed  $\text{WS}_2$  monolayer remnants.

A second change that can be observed from the AFM results is that the  $\text{WS}_2$  monolayer edge has been shifted, while there is also a very thin line marking the former edge visible in Fig. 3.20. Although this shift of the edge is only by about  $1 \mu\text{m}$ , it is still noticeable in Fig. 3.17, where the size of the triangle is smaller after high temperature measurements. The treatment also seems to have had some effect on the underlying substrate ( $\text{SiO}_2$ ), as evidenced by the black rectangle marked edge in Fig. 3.20(c). Here, part of the underlying  $\text{SiO}_2$  between the original and new  $\text{WS}_2$  appears to be eroded. Although we note that an imaging artifact cannot be ruled out, this apparent substrate degradation is also present in the eroded regions within the remaining monolayer (black rectangle marked as a hole in Fig. 3.20(c)). In turn, one possible reason for the shift of the edge may be due to a higher concentration of defects on the edge, as was discussed previously. The intrinsic defects can be located in grain boundaries or at edges or be present as local point defects and are the starting point for the degradation.

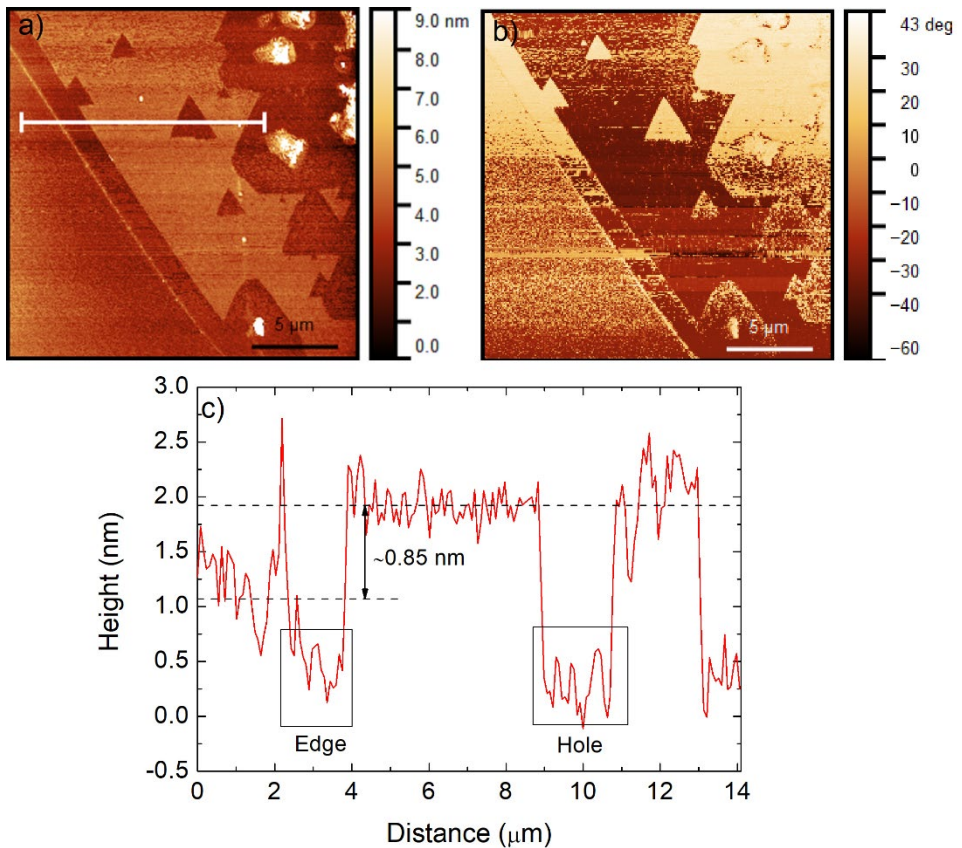


Figure 3.20: AFM height (a) and phase (b) images of the studied flake edge after high temperature measurements up to  $T = 723$  K. Line profile (c) is presented in red color (white line from Fig. 3.20(a)). (Figure 6 in [IV])

As stated earlier, contradictory reports can also be found regarding the high-temperature photoluminescent response of other TMDs, such as  $\text{MoS}_2$ . Many of the monolayered TMD materials (including  $\text{MoS}_2$ ) have similar structures and properties to  $\text{WS}_2$ , and similar general trends to those found here could be tentatively expected in such cases. However, we note that the individual materials are distinct, and it is difficult to predict with certainty the behavior of these other systems without further measurements.

## Conclusion

This thesis was focusing on the PL properties of different TMD monolayers, which either have a high density of defects or have been aged. The main results of this thesis can be concluded followingly:

1. CVD growth procedures for MoS<sub>2</sub> and WS<sub>2</sub> monolayers were successfully established at Taltech.
2. PL spectra of the CVD grown MoS<sub>2</sub> monolayer with high concentration of defects showed that the A band only exhibited specific excitonic properties, while the B-band was found to have a double structure. This double structure could be described by exciton and trion emissions and the B-trion binding energy of 18 meV was found.
3. Aged CVD grown WS<sub>2</sub> monolayers were found to have two kinds of strain: local tensile strain in the nanocap regions, which formed during aging due to nanoparticle oxidation beneath the monolayer, and an additional weaker strain due to increased surface roughness. Smaller band gap due to high tensile strain caused the excitons to localize to the nanocap regions. This localization of excitons was described well by the theory of localized-state ensemble.
4. In a low-temperature PL analysis of a CVD grown WS<sub>2</sub> monolayer, the asymmetrical defect-bound exciton band X<sub>D</sub> at 1.9 eV was found to dominate the spectra. A thermal activation energy of  $E_a = 33 \pm 4$  meV was found for the X<sub>D</sub> band. It is proposed that the X<sub>D</sub> band is related to the deep defect bound excitons and the most probable deep defect could be V<sub>S</sub>, whereas the structural defects and adsorbed atoms could also be the cause of these deep defects.
5. WS<sub>2</sub> monolayers showed at high temperatures and in an inert environment a standard and continuous decrease in PL intensity, accompanied with a near linear decrease in peak position and an increase in peak width. The center part of WS<sub>2</sub> monolayer was found to degrade following the handling at elevated temperatures, while the other region largely maintained its original properties. The area with irreversible changes had initially lower PL intensity than the remaining region. Higher concentration of defects was suggested to be responsible for the material loss.



## References

- [1] S. Novoselov, A. K. Geim, S. V. Morozov, D. Jiang, Y. Zhang, S. V. Dubonos, I. V. Grigorieva, and A. A. Firsov, "Electric Field Effect in Atomically Thin Carbon Films," *Science (80-. )*, vol. 306, no. 5696, pp. 666–669, 2004.
- [2] R. Lv, H. Terrones, A. L. Elías, N. Perea-López, H. R. Gutiérrez, E. Cruz-Silva, L. P. Rajukumar, M. S. Dresselhaus, and M. Terrones, "Two-dimensional transition metal dichalcogenides: Clusters, ribbons, sheets and more," *Nano Today*, vol. 10, no. 5, pp. 559–592, 2015.
- [3] B. Zhu, X. Chen, and X. Cui, "Exciton binding energy of monolayer WS<sub>2</sub>," *Sci. Rep.*, vol. 5, p. 9218, 2015.
- [4] A. T. Hanbicki, M. Currie, G. Kioseoglou, A. L. Friedman, and B. T. Jonker, "Measurement of high exciton binding energy in the monolayer transition-metal dichalcogenides WS<sub>2</sub> and WSe<sub>2</sub>," *Solid State Commun.*, vol. 203, pp. 16–20, 2015.
- [5] X. Zheng and X. Zhang, "Excitons in Two-Dimensional Materials," *IntechOpen*, pp. 1–29, 2019.
- [6] J. Chen, X. Zhao, S. J. R. Tan, H. Xu, B. Wu, B. Liu, D. Fu, W. Fu, D. Geng, Y. Liu, W. Liu, W. Tang, L. Li, W. Zhou, T. C. Sum, and K. P. Loh, "Chemical Vapor Deposition of Large-Size Monolayer MoSe<sub>2</sub> Crystals on Molten Glass," *J. Am. Chem. Soc.*, vol. 139, no. 3, pp. 1073–1076, 2017.
- [7] Y. Gao, Y. L. Hong, L. C. Yin, Z. Wu, Z. Yang, M. L. Chen, Z. Liu, T. Ma, D. M. Sun, Z. Ni, X. L. Ma, H. M. Cheng, and W. Ren, "Ultrafast Growth of High-Quality Monolayer WSe<sub>2</sub> on Au," *Adv. Mater.*, vol. 29, no. 29, pp. 1–8, 2017.
- [8] Y. Gao, Z. Liu, D. M. Sun, L. Huang, L. P. Ma, L. C. Yin, T. Ma, Z. Zhang, X. L. Ma, L. M. Peng, H. M. Cheng, and W. Ren, "Large-area synthesis of high-quality and uniform monolayer WS<sub>2</sub> on reusable Au foils," *Nat. Commun.*, vol. 6, pp. 1–10, 2015.
- [9] L. Zhou, L. Fox, M. Włodek, L. Islas, A. Slastanova, E. Robles, O. Bikondoa, R. Harniman, N. Fox, M. Cattelan, and W. H. Briscoe, "Surface structure of few layer graphene," *Carbon N. Y.*, vol. 136, pp. 255–261, 2018.
- [10] K. S. Novoselov, D. Jiang, F. Schedin, T. J. Booth, V. V. Khotkevich, S. V. Morozov, and A. K. Geim, "Two-dimensional atomic crystals," *Proc. Natl. Acad. Sci. U. S. A.*, vol. 102, no. 30, pp. 10451–10453, 2005.
- [11] G. R. Bhimanapati *et al.*, "Recent Advances in Two-Dimensional Materials beyond Graphene," *ACS Nano*, vol. 9, no. 12, pp. 11509–11539, 2015.
- [12] J. Xiao, M. Zhao, Y. Wang, and X. Zhang, "Excitons in atomically thin 2D semiconductors and their applications," *Nanophotonics*, vol. 6, no. 6, pp. 1309–1328, 2017.
- [13] H. Li, Z. Yin, Q. He, H. Li, X. Huang, G. Lu, D. W. H. Fam, A. I. Y. Tok, Q. Zhang, and H. Zhang, "Fabrication of single- and multilayer MoS<sub>2</sub> film-based field-effect transistors for sensing NO at room temperature," *Small*, vol. 8, no. 1, pp. 63–67, 2012.
- [14] G. H. Lee, Y. J. Yu, X. Cui, N. Petrone, C. H. Lee, M. S. Choi, D. Y. Lee, C. Lee, W. J. Yoo, K. Watanabe, T. Taniguchi, C. Nuckolls, P. Kim, and J. Hone, "Flexible and transparent MoS<sub>2</sub> field-effect transistors on hexagonal boron nitride-graphene heterostructures," *ACS Nano*, vol. 7, no. 9, pp. 7931–7936, 2013.
- [15] Y. Liu, Y. Gao, S. Zhang, J. He, J. Yu, and Z. Liu, "Valleytronics in transition metal dichalcogenides materials," *Nano Res.*, vol. 12, no. 11, pp. 2695–2711, 2019.

- [16] H. Wang, C. Zhang, W. Chan, S. Tiwari, and F. Rana, "Ultrafast response of monolayer molybdenum disulfide photodetectors," *Nat. Commun.*, vol. 6, pp. 6–11, 2015.
- [17] P. Ajayan, P. Kim, and K. Banerjee, "Two-dimensional van der Waals materials," *Phys. Today*, vol. 69, no. 9, pp. 38–44, 2016.
- [18] G. Gao, W. Gao, E. Cannuccia, J. Taha-Tijerina, L. Balicas, A. Mathkar, T. N. Narayanan, Z. Liu, B. K. Gupta, J. Peng, Y. Yin, A. Rubio, and P. M. Ajayan, "Artificially stacked atomic layers: Toward new van der waals solids," *Nano Lett.*, vol. 12, no. 7, pp. 3518–3525, 2012.
- [19] P. Tonndorf, R. Schmidt, P. Böttger, X. Zhang, J. Börner, A. Liebig, M. Albrecht, C. Kloc, O. Gordan, D. R. T. Zahn, S. Michaelis de Vasconcellos, and R. Bratschitsch, "Photoluminescence emission and Raman response of monolayer MoS<sub>2</sub>, MoSe<sub>2</sub>, and WSe<sub>2</sub>," *Opt. Express*, vol. 21, no. 4, pp. 4908–4916, 2013.
- [20] Y.-C. Lin, C.-H. Yeh, H.-C. Lin, M.-D. Siao, Z. Liu, H. Nakajima, T. Okazaki, M.-Y. Chou, K. Suenaga, and P.-W. Chiu, "Stable 1T Tungsten Disulfide Monolayer and Its Junctions: Growth and Atomic Structures," *ACS Nano*, vol. 12, pp. 12080–12088, 2018.
- [21] Y. Li, K. A. N. Duerloo, K. Wauson, and E. J. Reed, "Structural semiconductor-to-semimetal phase transition in two-dimensional materials induced by electrostatic gating," *Nat. Commun.*, vol. 7, pp. 1–8, 2016.
- [22] K. A. N. Duerloo, Y. Li, and E. J. Reed, "Structural phase transitions in two-dimensional Mo- and W-dichalcogenide monolayers," *Nat. Commun.*, vol. 5, no. May, 2014.
- [23] H. L. Zhuang, M. D. Johannes, A. K. Singh, and R. G. Hennig, "Doping-controlled phase transitions in single-layer MoS<sub>2</sub>," *Phys. Rev. B*, vol. 96, no. 16, pp. 1–8, 2017.
- [24] A. R. Beal, W. Y. Liang, and H. P. Hughes, "Kramers-Kronig analysis of the reflectivity spectra of 3R-WS<sub>2</sub> and 2H-WSe<sub>2</sub>," *J. Phys. C Solid State Phys.*, vol. 9, pp. 2449–2457, 1976.
- [25] M. Cotrufo, L. Sun, J. Choi, A. Alù, and X. Li, "Enhancing functionalities of atomically thin semiconductors with plasmonic nanostructures," *Nanophotonics*, vol. 8, no. 4, pp. 577–598, 2019.
- [26] J. You, M. D. Hossain, and Z. Luo, "Synthesis of 2D transition metal dichalcogenides by chemical vapor deposition with controlled layer number and morphology," *Nano Converg.*, vol. 5, no. 1, 2018.
- [27] C. Lee, Q. Li, W. Kalb, X. Z. Liu, H. Berger, R. W. Carpick, and J. Hone, "Frictional characteristics of atomically thin sheets," *Science (80-. )*, vol. 328, pp. 76–80, 2010.
- [28] G. Eda, H. Yamaguchi, D. Voiry, T. Fujita, M. Chen, and M. Chhowalla, "Photoluminescence from chemically exfoliated MoS<sub>2</sub>," *Nano Lett.*, vol. 11, pp. 5111–5116, 2011.
- [29] J. N. Coleman *et al.*, "Two-dimensional nanosheets produced by liquid exfoliation of layered materials," *Science (80-. )*, vol. 331, pp. 568–571, 2011.
- [30] D. Golberg, "Exfoliating the inorganics," *Nat. Nanotechnol.*, vol. 6, no. 4, pp. 200–201, 2011.
- [31] Y. H. Lee, X. Q. Zhang, W. Zhang, M. T. Chang, C. Te Lin, K. Di Chang, Y. C. Yu, J. T. W. Wang, C. S. Chang, L. J. Li, and T. W. Lin, "Synthesis of large-area MoS<sub>2</sub> atomic layers with chemical vapor deposition," *Adv. Mater.*, vol. 24, no. 17, pp. 2320–2325, 2012.

- [32] Y. C. Lin, W. Zhang, J. K. Huang, K. K. Liu, Y. H. Lee, C. Te Liang, C. W. Chu, and L. J. Li, "Wafer-scale MoS<sub>2</sub> thin layers prepared by MoO<sub>3</sub> sulfurization," *Nanoscale*, vol. 4, no. 20, pp. 6637–6641, 2012.
- [33] Y. Zhan, Z. Liu, S. Najmaei, P. M. Ajayan, and J. Lou, "Large-area vapor-phase growth and characterization of MoS<sub>2</sub> atomic layers on a SiO<sub>2</sub> substrate," *Small*, vol. 8, no. 7, pp. 966–971, 2012.
- [34] J. Xie, H. Zhang, S. Li, R. Wang, X. Sun, M. Zhou, J. Zhou, X. W. Lou, and Y. Xie, "Defect-rich MoS<sub>2</sub> ultrathin nanosheets with additional active edge sites for enhanced electrocatalytic hydrogen evolution," *Adv. Mater.*, vol. 25, no. 40, pp. 5807–5813, 2013.
- [35] H. Zhang, "Ultrathin Two-Dimensional Nanomaterials," *ACS Nano*, vol. 9, no. 10, pp. 9451–9469, 2015.
- [36] W. Zhao, Z. Ghorannevis, L. Chu, M. Toh, C. Kloc, P.-H. Tan, and G. Eda, "Evolution of Electronic Structure in Atomically Thin Sheets of WS<sub>2</sub> and WSe<sub>2</sub>," *ACS Nano*, vol. 7, no. 1, pp. 791–797, 2013.
- [37] S. Najmaei, Z. Liu, W. Zhou, X. Zou, G. Shi, S. Lei, B. I. Yakobson, J. C. Idrobo, P. M. Ajayan, and J. Lou, "Vapour phase growth and grain boundary structure of molybdenum disulphide atomic layers," *Nat. Mater.*, vol. 12, no. 8, pp. 754–759, 2013.
- [38] J. C. Shaw, H. Zhou, Y. Chen, N. O. Weiss, Y. Liu, Y. Huang, and X. Duan, "Chemical vapor deposition growth of monolayer MoSe<sub>2</sub> nanosheets," *Nano Res.*, vol. 7, no. 4, pp. 511–517, Apr. 2014.
- [39] C. Jung, S. M. Kim, H. Moon, G. Han, J. Kwon, Y. K. Hong, I. Omkaram, Y. Yoon, S. Kim, and J. Park, "Highly Crystalline CVD-grown Multilayer MoSe<sub>2</sub> Thin Film Transistor for Fast Photodetector," *Sci. Rep.*, vol. 5, pp. 1–9, 2015.
- [40] M. R. Rosenberger, H. J. Chuang, K. M. McCreary, C. H. Li, and B. T. Jonker, "Electrical Characterization of Discrete Defects and Impact of Defect Density on Photoluminescence in Monolayer WS<sub>2</sub>," *ACS Nano*, vol. 12, no. 2, pp. 1793–1800, 2018.
- [41] J. K. Huang, J. Pu, C. L. Hsu, M. H. Chiu, Z. Y. Juang, Y. H. Chang, W. H. Chang, Y. Iwasa, T. Takenobu, and L. J. Li, "Large-area synthesis of highly crystalline WSe<sub>2</sub> monolayers and device applications," *ACS Nano*, vol. 8, no. 1, pp. 923–930, 2014.
- [42] Y. Zhang, Y. Yao, M. G. Sendeku, L. Yin, X. Zhan, F. Wang, Z. Wang, and J. He, "Recent Progress in CVD Growth of 2D Transition Metal Dichalcogenides and Related Heterostructures," *Adv. Mater.*, vol. 31, no. 41, pp. 1–30, 2019.
- [43] A. M. Van Der Zande, P. Y. Huang, D. A. Chenet, T. C. Berkelbach, Y. You, G. H. Lee, T. F. Heinz, D. R. Reichman, D. A. Muller, and J. C. Hone, "Grains and grain boundaries in highly crystalline monolayer molybdenum disulphide," *Nat. Mater.*, vol. 12, no. 6, pp. 554–561, 2013.
- [44] S. Wang, Y. Rong, Y. Fan, M. Pacios, H. Bhaskaran, K. He, and J. H. Warner, "Shape evolution of monolayer MoS<sub>2</sub> crystals grown by chemical vapor deposition," *Chem. Mater.*, vol. 26, no. 22, pp. 6371–6379, 2014.
- [45] Y. Zhang, Y. Zhang, Q. Ji, J. Ju, H. Yuan, J. Shi, T. Gao, D. Ma, M. Liu, Y. Chen, X. Song, H. Y. Hwang, Y. Cui, and Z. Liu, "Controlled Growth of High-Quality Monolayer WS<sub>2</sub> Layers on Sapphire and Imaging Its Grain Boundary," *ACS Nano*, vol. 7, no. 10, pp. 8963–8971, 2013.

- [46] L. Dong, Y. Wang, J. Sun, C. Pan, Q. Zhang, L. Gu, B. Wan, C. Song, F. Pan, C. Wang, Z. Tang, and J. Zhang, "Facile access to shape-controlled growth of WS<sub>2</sub> monolayer via environment-friendly method," *2D Mater.*, vol. 6, p. 015007, 2019.
- [47] K. M. McCreary, A. T. Hanbicki, S. Singh, R. K. Kawakami, G. G. Jernigan, M. Ishigami, A. Ng, T. H. Brintlinger, R. M. Stroud, and B. T. Jonker, "The effect of preparation conditions on raman and photoluminescence of monolayer WS<sub>2</sub>," *Sci. Rep.*, vol. 6, no. October, pp. 1–10, 2016.
- [48] J. Gusakova, X. Wang, L. L. Shiao, A. Krivosheeva, V. Shaposhnikov, V. Borisenko, V. Gusakov, and B. K. Tay, "Electronic Properties of Bulk and Monolayer TMDs: Theoretical Study Within DFT Framework (GVJ-2e Method)," *Phys. Status Solidi Appl. Mater. Sci.*, vol. 214, no. 12, pp. 1–7, 2017.
- [49] K. F. Mak, C. Lee, J. Hone, J. Shan, and T. F. Heinz, "Atomically thin MoS<sub>2</sub>: A new direct-gap semiconductor," *Phys. Rev. Lett.*, vol. 105, no. 13, pp. 2–5, 2010.
- [50] A. Berkdemir, H. R. Gutiérrez, A. R. Botello-Méndez, N. Perea-López, A. L. Elías, C. I. Chia, B. Wang, V. H. Crespi, F. López-Urías, J. C. Charlier, H. Terrones, and M. Terrones, "Identification of individual and few layers of WS<sub>2</sub> using Raman Spectroscopy," *Sci. Rep.*, vol. 3, pp. 1–8, 2013.
- [51] H. Li, Q. Zhang, C. C. R. Yap, B. K. Tay, T. H. T. Edwin, A. Olivier, and D. Baillargeat, "From bulk to monolayer MoS<sub>2</sub>: Evolution of Raman scattering," *Adv. Funct. Mater.*, vol. 22, no. 7, pp. 1385–1390, 2012.
- [52] X. Zhang, X.-F. Qiao, W. Shi, J.-B. Wu, D.-S. Jiang, and P.-H. Tan, "Phonon and Raman scattering of two-dimensional transition metal dichalcogenides from monolayer, multilayer to bulk material," *Chem. Soc. Rev.*, vol. 44, pp. 2757–2785, 2015.
- [53] I. Kylänpää and H. P. Komsa, "Binding energies of exciton complexes in transition metal dichalcogenide monolayers and effect of dielectric environment," *Phys. Rev. B - Condens. Matter Mater. Phys.*, vol. 92, no. 20, pp. 1–6, 2015.
- [54] G. Plechinger, P. Nagler, J. Kraus, N. Paradiso, C. Strunk, C. Schüller, and T. Korn, "Identification of excitons, trions and biexcitons in single-layer WS<sub>2</sub>," *Phys. Status Solidi - Rapid Res. Lett.*, vol. 9, no. 8, pp. 457–461, 2015.
- [55] G. Bin Liu, W. Y. Shan, Y. Yao, W. Yao, and D. Xiao, "Three-band tight-binding model for monolayers of group-VIB transition metal dichalcogenides," *Phys. Rev. B - Condens. Matter Mater. Phys.*, vol. 88, no. 8, pp. 1–10, 2013.
- [56] D. W. Latzke, W. Zhang, A. Suslu, T. R. Chang, H. Lin, H. T. Jeng, S. Tongay, J. Wu, A. Bansil, and A. Lanzara, "Electronic structure, spin-orbit coupling, and interlayer interaction in bulk MoS<sub>2</sub> and WS<sub>2</sub>," *Phys. Rev. B*, vol. 91, no. 23, p. 235202, 2015.
- [57] J. G. Roch, G. Froehlicher, N. Leisgang, P. Makk, K. Watanabe, T. Taniguchi, and R. J. Warburton, "Spin-polarized electrons in monolayer MoS<sub>2</sub>," *Nat. Nanotechnol.*, vol. 14, no. 5, pp. 432–436, 2019.
- [58] G. Plechinger, J. Mann, E. Preciado, D. Barroso, A. Nguyen, J. Eroms, C. Schüller, L. Bartels, and T. Korn, "A direct comparison of CVD-grown and exfoliated MoS<sub>2</sub> using optical spectroscopy," *Semicond. Sci. Technol.*, vol. 29, no. 6, 2014.
- [59] C. R. Zhu, G. Wang, B. L. Liu, X. Marie, X. F. Qiao, X. Zhang, X. X. Wu, H. Fan, P. H. Tan, T. Amand, and B. Urbaszek, "Strain tuning of optical emission energy and polarization in monolayer and bilayer MoS<sub>2</sub>," *Phys. Rev. B - Condens. Matter Mater. Phys.*, vol. 88, no. 12, pp. 1–5, 2013.

- [60] Y. M. He, G. Clark, J. R. Schaibley, Y. He, M. C. Chen, Y. J. Wei, X. Ding, Q. Zhang, W. Yao, X. Xu, C. Y. Lu, and J. W. Pan, "Single quantum emitters in monolayer semiconductors," *Nat. Nanotechnol.*, vol. 10, pp. 497–502, 2015.
- [61] W. H. Chae, J. D. Cain, E. D. Hanson, A. A. Murthy, and V. P. Dravid, "Substrate-induced strain and charge doping in CVD-grown monolayer MoS<sub>2</sub>," *Appl. Phys. Lett.*, vol. 111, no. 14, 2017.
- [62] J. Shang, C. Cong, X. Shen, W. Yang, C. Zou, N. Peimyoo, B. Cao, M. Eginligil, W. Lin, W. Huang, and T. Yu, "Revealing electronic nature of broad bound exciton bands in two-dimensional semiconducting WS<sub>2</sub> and MoS<sub>2</sub>," *Phys. Rev. Mater.*, vol. 1, p. 074001, 2017.
- [63] C. Rice, R. J. Young, R. Zan, U. Bangert, D. Wolverson, T. Georgiou, R. Jalil, and K. S. Novoselov, "Raman-scattering measurements and first-principles calculations of strain-induced phonon shifts in monolayer MoS<sub>2</sub>," *Phys. Rev. B - Condens. Matter Mater. Phys.*, vol. 87, no. 8, pp. 1–5, 2013.
- [64] R. Roldán, A. Castellanos-Gomez, E. Cappelluti, and F. Guinea, "Strain engineering in semiconducting two-dimensional crystals," *J. Phys. Condens. Matter*, vol. 27, no. 31, 2015.
- [65] W. M. Parkin, A. Balan, L. Liang, P. M. Das, M. Lamparski, C. H. Naylor, J. A. Rodríguez-Manzo, A. T. C. Johnson, V. Meunier, and M. Drndić, "Raman Shifts in Electron-Irradiated Monolayer MoS<sub>2</sub>," *ACS Nano*, vol. 10, no. 4, pp. 4134–4142, 2016.
- [66] J. Pandey and A. Soni, "Unraveling biexciton and excitonic excited states from defect bound states in monolayer MoS<sub>2</sub>," *Appl. Surf. Sci.*, vol. 463, no. August 2018, pp. 52–57, 2019.
- [67] K. F. Mak, K. He, C. Lee, G. H. Lee, J. Hone, T. F. Heinz, and J. Shan, "Tightly bound trions in monolayer MoS<sub>2</sub>," *Nat. Mater.*, vol. 12, no. 3, pp. 207–211, 2013.
- [68] Y. Lin, X. Ling, L. Yu, S. Huang, A. L. Hsu, Y. H. Lee, J. Kong, M. S. Dresselhaus, and T. Palacios, "Dielectric screening of excitons and trions in single-layer MoS<sub>2</sub>," *Nano Lett.*, vol. 14, no. 10, pp. 5569–5576, 2014.
- [69] M. D. Tran, J. H. Kim, and Y. H. Lee, "Tailoring photoluminescence of monolayer transition metal dichalcogenides," *Curr. Appl. Phys.*, vol. 16, no. 9, pp. 1159–1174, 2016.
- [70] J. W. Christopher, B. B. Goldberg, and A. K. Swan, "Long tailed trions in monolayer MoS<sub>2</sub>: Temperature dependent asymmetry and resulting red-shift of trion photoluminescence spectra," *Sci. Rep.*, vol. 7, no. 1, pp. 1–8, 2017.
- [71] T. C. Berkelbach, M. S. Hybertsen, and D. R. Reichman, "Theory of neutral and charged excitons in monolayer transition metal dichalcogenides," *Phys. Rev. B - Condens. Matter Mater. Phys.*, vol. 88, no. 4, pp. 1–6, 2013.
- [72] M. Drüppel, T. Deilmann, P. Krüger, and M. Rohlfing, "Diversity of trion states and substrate effects in the optical properties of an MoS<sub>2</sub> monolayer," *Nat. Commun.*, vol. 8, no. 1, p. 2117, 2017.
- [73] Z. Wang, L. Zhao, K. F. Mak, and J. Shan, "Probing the Spin-Polarized Electronic Band Structure in Monolayer Transition Metal Dichalcogenides by Optical Spectroscopy," *Nano Lett.*, vol. 17, no. 2, pp. 740–746, 2017.
- [74] I. Paradisanos, N. Pliatsikas, P. Patsalas, C. Fotakis, E. Kymakis, G. Kioseoglou, and E. Stratakis, "Spatial non-uniformity in exfoliated WS<sub>2</sub> single layers," *Nanoscale*, vol. 8, no. 36, pp. 16197–16203, 2016.

- [75] Y. Wang, C. Cong, W. Yang, J. Shang, N. Peimyoo, Y. Chen, J. Kang, J. Wang, W. Huang, and T. Yu, "Strain-induced direct–indirect bandgap transition and phonon modulation in monolayer  $WS_2$ ," *Nano Res.*, vol. 8, no. 8, pp. 2562–2572, 2015.
- [76] Y. Yu, Y. Yu, C. Xu, Y. Q. Cai, L. Su, Y. Zhang, Y. W. Zhang, K. Gundogdu, and L. Cao, "Engineering Substrate Interactions for High Luminescence Efficiency of Transition-Metal Dichalcogenide Monolayers," *Adv. Funct. Mater.*, vol. 26, no. 26, pp. 4733–4739, 2016.
- [77] L. Su, Y. Yu, L. Cao, and Y. Zhang, "Effects of substrate type and material-substrate bonding on high-temperature behavior of monolayer  $WS_2$ ," *Nano Res.*, vol. 8, no. 8, pp. 2686–2697, 2015.
- [78] M. R. Rosenberger, H. J. Chuang, K. M. McCreary, C. H. Li, and B. T. Jonker, "Electrical Characterization of Discrete Defects and Impact of Defect Density on Photoluminescence in Monolayer  $WS_2$ ," *ACS Nano*, vol. 12, no. 2, pp. 1793–1800, 2018.
- [79] H. Liu, J. Lu, K. Ho, Z. Hu, Z. Dang, A. Carvalho, H. R. Tan, E. S. Tok, and C. H. Sow, "Fluorescence Concentric Triangles: A Case of Chemical Heterogeneity in  $WS_2$  Atomic Monolayer," *Nano Lett.*, vol. 16, no. 9, pp. 5559–5567, 2016.
- [80] Q. Li, Q. Zhou, L. Shi, Q. Chen, and J. Wang, "Recent advances in oxidation and degradation mechanisms of ultrathin 2D materials under ambient conditions and their passivation strategies," *J. Mater. Chem. A*, vol. 7, no. 9, pp. 4291–4312, 2019.
- [81] J. Gao, B. Li, J. Tan, P. Chow, T. M. Lu, and N. Koratkar, "Aging of Transition Metal Dichalcogenide Monolayers," *ACS Nano*, vol. 10, no. 2, pp. 2628–2635, 2016.
- [82] Z. He, X. Wang, W. Xu, Y. Zhou, Y. Sheng, Y. Rong, J. M. Smith, and J. H. Warner, "Revealing Defect-State Photoluminescence in Monolayer  $WS_2$  by Cryogenic Laser Processing," *ACS Nano*, vol. 10, pp. 5847–5855, 2016.
- [83] Y. Rong, K. He, M. Pacios, A. W. Robertson, H. Bhaskaran, and J. H. Warner, "Controlled preferential oxidation of grain boundaries in monolayer tungsten disulfide for direct optical imaging," *ACS Nano*, vol. 9, no. 4, pp. 3695–3703, 2015.
- [84] J. Krustok, T. Raadik, R. Jaaniso, V. Kiisk, I. Sildos, M. Marandi, H. P. Komsa, B. Li, X. Zhang, Y. Gong, and P. M. Ajayan, "Optical study of local strain related disordering in CVD-grown  $MoSe_2$  monolayers," *Appl. Phys. Lett.*, vol. 109, no. 25, p. 253106, 2016.
- [85] V. Orsi Gordo, M. A. G. Balanta, Y. Galvão Gobato, F. S. Covre, H. V. A. Galeti, F. Iikawa, O. D. D. Couto Jr, F. Qu, M. Henini, D. W. Hewak, and C. C. Huang, "Revealing the nature of low-temperature photoluminescence peaks by laser treatment in van der Waals epitaxially grown  $WS_2$  monolayers," *Nanoscale*, vol. 10, pp. 4807–4815, 2018.
- [86] C. Palacios-Berraquero, D. M. Kara, A. R.-P. Montblanch, M. Barbone, P. Latawiec, D. Yoon, A. K. Ott, M. Loncar, A. C. Ferrari, and M. Atatüre, "Large-scale quantum-emitter arrays in atomically thin semiconductors," *Nat. Commun.*, vol. 8, p. 15093, 2017.
- [87] A. Srivastava, M. Sidler, A. V. Allain, D. S. Lembke, A. Kis, and A. Imamoglu, "Optically active quantum dots in monolayer  $WSe_2$ ," *Nat. Nanotechnol.*, vol. 10, pp. 491–496, 2015.

- [88] P. Tonndorf, R. Schmidt, R. Schneider, J. Kern, M. Buscema, G. A. Steele, A. Castellanos-Gomez, H. S. J. van der Zant, S. Michaelis de Vasconcellos, and R. Bratschitsch, "Single-photon emission from localized excitons in an atomically thin semiconductor," *Optica*, vol. 2, no. 4, pp. 347–352, 2015.
- [89] Z. Wu and Z. Ni, "Spectroscopic investigation of defects in two-dimensional materials," *Nanophotonics*, vol. 6, no. 6, pp. 1219–1237, 2017.
- [90] Z. Wu, W. Zhao, J. Jiang, T. Zheng, Y. You, J. Lu, and Z. Ni, "Defect Activated Photoluminescence in WSe<sub>2</sub> Monolayer," *J. Phys. Chem. C*, vol. 121, pp. 12294–12299, 2017.
- [91] T. Venanzi, H. Arora, A. Erbe, A. Pashkin, S. Winnerl, M. Helm, and H. Schneider, "Exciton localization in MoSe<sub>2</sub> monolayers induced by adsorbed gas molecules," *Appl. Phys. Lett.*, vol. 114, p. 172106, 2019.
- [92] Y. Li, W. Liu, H. Xu, C. Zhang, L. Yang, W. Yue, and Y. Liu, "Abnormal high-temperature luminescence enhancement observed in monolayer MoS<sub>2</sub> flakes: Thermo-driven transition from negatively charged trions to neutral excitons," *J. Mater. Chem. C*, vol. 4, no. 39, pp. 9187–9196, 2016.
- [93] Y. Chen, W. Wen, Y. Zhu, N. Mao, Q. Feng, M. Zhang, H. P. Hsu, J. Zhang, Y. S. Huang, and L. Xie, "Temperature-dependent photoluminescence emission and Raman scattering from Mo<sub>1-x</sub>W<sub>x</sub>S<sub>2</sub> monolayers," *Nanotechnology*, vol. 27, p. 445705, 2016.
- [94] P. J. Ko, A. Abderrahmane, T. V. Thu, D. Ortega, T. Takamura, and A. Sandhu, "Laser Power Dependent Optical Properties of Mono- and Few-Layer MoS<sub>2</sub>," *J. Nanosci. Nanotechnol.*, vol. 15, pp. 6843–6846, 2015.
- [95] S. Zhu, D. Li, Y. Hu, J. Wang, X. Wang, and W. Lu, "Enhancement of direct and indirect exciton emissions in few-layer WSe<sub>2</sub> at high temperatures," *Mater. Res. Express*, vol. 5, p. 066209, 2018.
- [96] H. Chen, Y. Li, W. Liu, H. Xu, G. Yang, J. Shi, Q. Feng, T. Yu, X. Liu, and Y. Liu, "High-temperature driven inter-valley carrier transfer and significant fluorescence enhancement in multilayer WS<sub>2</sub>," *Nanoscale Horizons*, vol. 3, no. 6, pp. 598–605, 2018.
- [97] A. P. S. Gaur, S. Sahoo, J. F. Scott, and R. S. Katiyar, "Electron - Phonon interaction and double-resonance Raman studies in monolayer WS<sub>2</sub>," *J. Phys. Chem. C*, vol. 119, no. 9, pp. 5146–5151, 2015.
- [98] Z. Hu, Y. Bao, Z. Li, Y. Gong, R. Feng, Y. Xiao, X. Wu, Z. Zhang, X. Zhu, P. M. Ajayan, and Z. Fang, "Temperature dependent Raman and photoluminescence of vertical WS<sub>2</sub>/MoS<sub>2</sub> monolayer heterostructures," *Sci. Bull.*, vol. 62, pp. 16–21, 2017.
- [99] G. Ye, Y. Gong, J. Lin, B. Li, Y. He, S. T. Pantelides, W. Zhou, R. Vajtai, and P. M. Ajayan, "Defects Engineered Monolayer MoS<sub>2</sub> for Improved Hydrogen Evolution Reaction," *Nano Lett.*, vol. 16, pp. 1097–1103, 2016.
- [100] K. Yao, J. D. Femi-Oyetero, S. Yao, Y. Jiang, L. El Bouanani, D. C. Jones, P. A. Ecton, U. Philipose, M. El Bouanani, B. Rout, A. Neogi, and J. M. Perez, "Rapid ambient degradation of monolayer MoS<sub>2</sub> after heating in air," *2D Mater.*, vol. 7, p. 015024, 2020.
- [101] K. F. Mak, M. Y. Sfeir, Y. Wu, C. H. Lui, J. A. Misewich, and T. F. Heinz, "Measurement of the Optical Conductivity of Graphene," *Phys. Rev. Lett.*, vol. 101, p. 196405, 2008.
- [102] A. Arora, M. Koperski, K. Nogajewski, J. Marcus, C. Faugeras, and M. Potemski, "Excitonic resonances in thin films of WSe<sub>2</sub>: From monolayer to bulk material," *Nanoscale*, vol. 7, pp. 10421–10429, 2015.

- [103] C. Lee, H. Yan, L. E. Brus, T. F. Heinz, J. Hone, and S. Ryu, "Anomalous lattice vibrations of single- and few-layer MoS<sub>2</sub>," *ACS Nano*, vol. 4, no. 5, pp. 2695–2700, 2010.
- [104] A. Michail, N. Delikoukos, J. Parthenios, C. Galiotis, and K. Papagelis, "Optical detection of strain and doping inhomogeneities in single layer MoS<sub>2</sub>," *Appl. Phys. Lett.*, vol. 108, no. 17, 2016.
- [105] H. Li, A. W. Contryman, X. Qian, S. M. Ardakani, Y. Gong, X. Wang, J. M. Weisse, C. H. Lee, J. Zhao, P. M. Ajayan, J. Li, H. C. Manoharan, and X. Zheng, "Optoelectronic crystal of artificial atoms in strain-textured molybdenum disulphide," *Nat. Commun.*, vol. 6, no. May, 2015.
- [106] H. Nan, Z. Wang, W. Wang, Z. Liang, Y. Lu, Q. Chen, D. He, P. Tan, F. Miao, X. Wang, J. Wang, and Z. Ni, "Strong photoluminescence enhancement of MoS<sub>2</sub> through defect engineering and oxygen bonding," *ACS Nano*, vol. 8, no. 6, pp. 5738–5745, 2014.
- [107] B. Chakraborty, A. Bera, D. V. S. Muthu, S. Bhowmick, U. V. Waghmare, and A. K. Sood, "Symmetry-dependent phonon renormalization in monolayer MoS<sub>2</sub> transistor," *Phys. Rev. B - Condens. Matter Mater. Phys.*, vol. 85, no. 16, pp. 2–5, 2012.
- [108] A. Azcatl, X. Qin, A. Prakash, C. Zhang, L. Cheng, Q. Wang, N. Lu, M. J. Kim, J. Kim, K. Cho, R. Addou, C. L. Hinkle, J. Appenzeller, and R. M. Wallace, "Covalent Nitrogen Doping and Compressive Strain in MoS<sub>2</sub> by Remote N<sub>2</sub> Plasma Exposure," *Nano Lett.*, vol. 16, no. 9, pp. 5437–5443, 2016.
- [109] S. Mignuzzi, A. J. Pollard, N. Bonini, B. Brennan, I. S. Gilmore, M. A. Pimenta, D. Richards, and D. Roy, "Effect of disorder on Raman scattering of single-layer MoS<sub>2</sub>," *Phys. Rev. B - Condens. Matter Mater. Phys.*, vol. 91, no. 19, pp. 1–7, 2015.
- [110] D. Wu, H. Huang, X. Zhu, Y. He, Q. Xie, X. Chen, X. Zheng, H. Duan, and Y. Gao, "E" Raman mode in thermal strain-fractured CVD-MoS<sub>2</sub>," *Crystals*, vol. 6, no. 11, 2016.
- [111] X. Li and H. Zhu, "Two-dimensional MoS<sub>2</sub>: Properties, preparation, and applications," *J. Mater.*, vol. 1, no. 1, pp. 33–44, 2015.
- [112] A. Zafar, H. Nan, Z. Zafar, Z. Wu, J. Jiang, Y. You, and Z. Ni, "Probing the intrinsic optical quality of CVD grown MoS<sub>2</sub>," *Nano Res.*, vol. 10, no. 5, pp. 1608–1617, 2017.
- [113] Z. Liu, M. Amani, S. Najmaei, Q. Xu, X. Zou, W. Zhou, T. Yu, C. Qiu, A. G. Birdwell, F. J. Crowne, R. Vajtai, B. I. Yakobson, Z. Xia, M. Dubey, P. M. Ajayan, and J. Lou, "Strain and structure heterogeneity in MoS<sub>2</sub> atomic layers grown by chemical vapour deposition," *Nat. Commun.*, vol. 5, 2014.
- [114] N. Scheuschner, O. Ochedowski, A. M. Kaulitz, R. Gillen, M. Schleberger, and J. Maultzsch, "Photoluminescence of freestanding single- and few-layer MoS<sub>2</sub>," *Phys. Rev. B - Condens. Matter Mater. Phys.*, vol. 89, no. 12, pp. 2–7, 2014.
- [115] H. J. Conley, B. Wang, J. I. Ziegler, R. F. Haglund, S. T. Pantelides, and K. I. Bolotin, "Bandgap engineering of strained monolayer and bilayer MoS<sub>2</sub>," *Nano Lett.*, vol. 13, no. 8, pp. 3626–3630, 2013.
- [116] D. Lloyd, X. Liu, J. W. Christopher, L. Cantley, A. Wadehra, B. L. Kim, B. B. Goldberg, A. K. Swan, and J. S. Bunch, "Band Gap Engineering with Ultralarge Biaxial Strains in Suspended Monolayer MoS<sub>2</sub>," *Nano Lett.*, vol. 16, no. 9, pp. 5836–5841, 2016.
- [117] Z. Li, S. W. Chang, C. C. Chen, and S. B. Cronin, "Enhanced photocurrent and photoluminescence spectra in MoS<sub>2</sub> under ionic liquid gating," *Nano Res.*, vol. 7, no. 7, pp. 973–980, 2014.



- [118] T. Schmidt, K. Lischka, and W. Zulehner, "Excitation-power dependence of the near-band-edge photoluminescence of semiconductors," *Phys. Rev. B*, vol. 45, no. 16, pp. 8989–8994, 1992.
- [119] D. Kaplan, Y. Gong, K. Mills, V. Swaminathan, P. M. Ajayan, S. Shirodkar, and E. Kaxiras, "Excitation intensity dependence of photoluminescence from monolayers of MoS<sub>2</sub> and WS<sub>2</sub>/MoS<sub>2</sub> heterostructures," *2D Mater.*, vol. 3, no. 1, 2016.
- [120] L. Li, R. Long, T. Bertolini, and O. V. Prezhdo, "Sulfur Adatom and Vacancy Accelerate Charge Recombination in MoS<sub>2</sub> but by Different Mechanisms: Time-Domain Ab Initio Analysis," *Nano Lett.*, vol. 17, no. 12, pp. 7962–7967, 2017.
- [121] T. Deilmann and K. S. Thygesen, "Dark excitations in monolayer transition metal dichalcogenides," *Phys. Rev. B*, vol. 96, no. 20, pp. 1–5, 2017.
- [122] Y. Gong, Z. Lin, G. Ye, G. Shi, S. Feng, Y. Lei, A. L. Elías, N. Perea-Lopez, R. Vajtai, H. Terrones, Z. Liu, M. Terrones, and P. M. Ajayan, "Tellurium-Assisted Low-Temperature Synthesis of MoS<sub>2</sub> and WS<sub>2</sub> Monolayers," *ACS Nano*, vol. 9, no. 12, pp. 11658–11666, 2015.
- [123] H. R. Gutiérrez, N. Perea-López, A. L. Elías, A. Berkdemir, B. Wang, R. Lv, F. López-Urías, V. H. Crespi, H. Terrones, and M. Terrones, "Extraordinary room-temperature photoluminescence in triangular WS<sub>2</sub> monolayers," *Nano Lett.*, vol. 13, no. 8, pp. 3447–3454, 2013.
- [124] C. Cong, J. Shang, X. Wu, B. Cao, N. Peimyoo, C. Qiu, L. Sun, and T. Yu, "Synthesis and optical properties of large-area single-crystalline 2D semiconductor WS<sub>2</sub> monolayer from chemical vapor deposition," *Adv. Opt. Mater.*, vol. 2, no. 2, pp. 131–136, 2014.
- [125] Y. Ding and B. Xiao, "Thermal expansion tensors, Grüneisen parameters and phonon velocities of bulk MT<sub>2</sub> (M = W and Mo; T = S and Se) from first principles calculations," *RSC Adv.*, vol. 5, no. 24, pp. 18391–18400, 2015.
- [126] L. Meng, Y. Zhang, S. Hu, X. Wang, C. Liu, Y. Guo, X. Wang, and X. Yan, "Two dimensional WS<sub>2</sub> lateral heterojunctions by strain modulation," *Appl. Phys. Lett.*, vol. 108, no. 26, p. 263104, 2016.
- [127] J. S. Ross, S. Wu, H. Yu, N. J. Ghimire, A. M. Jones, G. Aivazian, J. Yan, D. G. Mandrus, D. Xiao, W. Yao, and X. Xu, "Electrical control of neutral and charged excitons in a monolayer semiconductor," *Nat. Commun.*, vol. 4, p. 1474, 2013.
- [128] S. Tongay, J. Suh, C. Ataca, W. Fan, A. Luce, J. S. Kang, J. Liu, C. Ko, R. Raghunathanan, J. Zhou, F. Ogletree, J. Li, J. C. Grossman, and J. Wu, "Defects activated photoluminescence in two-dimensional semiconductors: Interplay between bound, charged, and free excitons," *Sci. Rep.*, vol. 3, p. 2657, 2013.
- [129] K. P. O'Donnell and X. Chen, "Temperature dependence of semiconductor band gaps," *Appl. Phys. Lett.*, vol. 58, no. 25, pp. 2924–2926, 1991.
- [130] K. Wei, Y. Liu, H. Yang, X. Cheng, and T. Jiang, "Large Range Manipulation of Exciton Species in Monolayer WS<sub>2</sub>," *Appl. Opt.*, vol. 55, no. 23, pp. 6251–6255, 2016.
- [131] Q. Li, S. J. Xu, W. C. Cheng, M. H. Xie, S. Y. Tong, C. M. Che, and H. Yang, "Thermal redistribution of localized excitons and its effect on the luminescence band in InGaN ternary alloys," *Appl. Phys. Lett.*, vol. 79, no. 12, pp. 1810–1812, 2001.
- [132] A. R. Mohmad, F. Bastiman, C. J. Hunter, R. D. Richards, S. J. Sweeney, J. S. Ng, J. P. R. David, and B. Y. Majlis, "Localization effects and band gap of GaAsBi alloys," *Phys. Status Solidi Basic Res.*, vol. 251, no. 6, pp. 1276–1281, 2014.

- [133] S. Rudin, T. L. Reinecke, and B. Segall, "Temperature-dependent exciton linewidths in semiconductor quantum wells," *Phys. Rev. B*, vol. 41, no. 5, pp. 3017–3027, 1990.
- [134] A. Molina-Sánchez and L. Wirtz, "Phonons in single-layer and few-layer MoS<sub>2</sub> and WS<sub>2</sub>," *Phys. Rev. B - Condens. Matter Mater. Phys.*, vol. 84, no. 15, pp. 1–8, 2011.
- [135] Q. Li, S. J. Xu, M. H. Xie, and S. Y. Tong, "A model for luminescence of localized state ensemble," *Europhys. Lett.*, vol. 71, no. 6, p. 14, 2005.
- [136] J. Feng, X. Qian, C. W. Huang, and J. Li, "Strain-engineered artificial atom as a broad-spectrum solar energy funnel," *Nat. Photonics*, vol. 6, no. 12, pp. 866–872, 2012.
- [137] X. H. Wang, J. Q. Ning, Z. C. Su, C. C. Zheng, B. R. Zhu, L. Xie, H. S. Wu, and S. J. Xu, "Photoinduced doping and photoluminescence signature in an exfoliated WS<sub>2</sub> monolayer semiconductor," *RSC Adv.*, vol. 6, no. 33, pp. 27677–27681, 2016.
- [138] J. He, D. He, Y. Wang, Q. Cui, F. Ceballos, and H. Zhao, "Spatiotemporal dynamics of excitons in monolayer and bulk WS<sub>2</sub>," *Nanoscale*, vol. 7, no. 21, pp. 9526–9531, 2015.
- [139] B. G. Shin, G. H. Han, S. J. Yun, H. M. Oh, J. J. Bae, Y. J. Song, C. Y. Park, and Y. H. Lee, "Indirect Bandgap Puddles in Monolayer MoS<sub>2</sub> by Substrate-Induced Local Strain," *Adv. Mater.*, vol. 28, no. 42, pp. 9378–9384, 2016.
- [140] J. D. Cain, F. Shi, J. Wu, and V. P. Dravid, "Growth Mechanism of Transition Metal Dichalcogenide Monolayers: The Role of Self-Seeding Fullerene Nuclei," *ACS Nano*, vol. 10, no. 5, pp. 5440–5445, 2016.
- [141] Y. Zhang, Y. Zhang, Q. Ji, J. Ju, H. Yuan, J. Shi, T. Gao, D. Ma, M. Liu, Y. Chen, X. Song, H. Y. Hwang, Y. Cui, and Z. Liu, "Controlled Growth of High-Quality Monolayer WS<sub>2</sub> Layers on Sapphire and Imaging Its Grain Boundary," *ACS Nano*, vol. 7, no. 10, pp. 8963–8971, 2013.
- [142] P. K. Chow, R. B. Jacobs-Gedrim, J. Gao, T. M. Lu, B. Yu, H. Terrones, and N. Koratkar, "Defect-induced photoluminescence in monolayer semiconducting transition metal dichalcogenides," *ACS Nano*, vol. 9, no. 2, pp. 1520–1527, 2015.
- [143] K. M. McCreary, A. T. Hanbicki, G. G. Jernigan, J. C. Culbertson, and B. T. Jonker, "Synthesis of Large-Area WS<sub>2</sub> monolayers with Exceptional Photoluminescence," *Sci. Rep.*, vol. 6, p. 19159, 2016.
- [144] A. M. Dadgar, D. Scullion, K. Kang, D. Esposito, E. H. Yang, I. P. Herman, M. A. Pimenta, E. G. Santos, and A. N. Pasupathy, "Strain Engineering and Raman Spectroscopy of Monolayer Transition Metal Dichalcogenides," *Chem. Mater.*, vol. 30, pp. 5148–5155, 2018.
- [145] H. Gu, L. Chen, Y. Lu, F. Tian, Z. Zhang, K. Xu, J. Wu, V. D. Botcha, K. Li, and X. Liu, "Low-temperature study of neutral and charged excitons in the large-area monolayer WS<sub>2</sub>," *Jpn. J. Appl. Phys.*, vol. 57, p. 060309, 2018.
- [146] J. Krustok, H. Collan, M. Yakushev, and K. Hjelt, "The Role of Spatial Potential Fluctuations in the Shape of the PL Bands of Multinary Semiconductor Compounds," *Phys. Scr.*, vol. T79, pp. 179–182, 1999.
- [147] M. V. Yakushev, M. A. Sulimov, J. Márquez-Prieto, I. Forbes, J. Krustok, P. R. Edwards, V. D. Zhivulko, O. M. Borodavchenko, A. V. Mudryi, and R. W. Martin, "Influence of the copper content on the optical properties of CZTSe thin films," *Sol. Energy Mater. Sol. Cells*, vol. 168, pp. 69–77, 2017.

- [148] J. Krustok, J. Raudoja, M. Yakushev, R. D. Pilkington, and H. Collan, "On the Shape of the Close-to-Band-Edge Photoluminescent Emission Spectrum in Compensated CuGaSe<sub>2</sub>," *Phys. Status Solidi*, vol. 173, pp. 483–490, 1999.
- [149] J. Krustok, H. Collan, and K. Hjelt, "Does the low-temperature Arrhenius plot of the photoluminescence intensity in CdTe point towards an erroneous activation energy?," *J. Appl. Phys.*, vol. 81, no. 3, pp. 1442–1445, 1997.
- [150] V. Carozo, Y. Wang, K. Fujisawa, B. R. Carvalho, A. Mccreary, S. Feng, Z. Lin, C. Zhou, N. Perea-lópez, A. L. Elías, B. Kabius, V. H. Crespi, and M. Terrones, "Optical identification of sulfur vacancies : Bound excitons at the edges of monolayer tungsten disulfide," *Sci. Adv.*, vol. 3, p. 1602813, 2017.
- [151] Z. Wu, Z. Luo, Y. Shen, W. Zhao, W. Wang, H. Nan, X. Guo, L. Sun, X. Wang, Y. You, and Z. Ni, "Defects as a factor limiting carrier mobility in WSe<sub>2</sub> : A spectroscopic investigation," *Nano Res.*, vol. 9, no. 12, pp. 3622–3631, 2016.
- [152] N. Saigal and S. Ghosh, "Evidence for two distinct defect related luminescence features in monolayer MoS<sub>2</sub>," *Appl. Phys. Lett.*, vol. 109, p. 122105, 2016.
- [153] A. Jagomägi, J. Krustok, M. Grossberg, M. Danilson, and J. Raudoja, "Deep defect related photoluminescence in heavily doped CuGaTe<sub>2</sub> crystals," *Phys. Status Solidi Appl. Mater. Sci.*, vol. 203, no. 5, pp. 949–955, 2006.
- [154] J. Shang, X. Shen, C. Cong, N. Peimyoo, B. Cao, M. Eginligil, and T. Yu, "Observation of Excitonic Fine Structure in a 2D Transition-Metal Dichalcogenide Semiconductor," *ACS Nano*, vol. 9, no. 1, pp. 647–655, 2015.
- [155] X. Zhao, X. Dai, C. Xia, and T. Wang, "Superlattices and Microstructures Structural defects in pristine and Mn-doped monolayer WS<sub>2</sub> : A first-principles study," *Superlattices Microstruct.*, vol. 85, pp. 339–347, 2015.
- [156] H. Liu, N. Han, and J. Zhao, "Atomistic insight into the oxidation of monolayer transition metal dichalcogenides: from structures to electronic properties," *RSC Adv.*, vol. 5, pp. 17572–17581, 2015.
- [157] J. Wei, Z. Ma, H. Zeng, Z. Wang, Q. Wei, and P. Peng, "Electronic and optical properties of vacancy-doped WS<sub>2</sub> monolayers," *AIP Adv.*, vol. 2, p. 042141, 2012.
- [158] E. Pollmann, L. Madauß, V. Zeuner, and M. Schleberger, "Strain in Single-Layer MoS<sub>2</sub> Flakes Grown by Chemical Vapor Deposition," *Encycl. Interfacial Chem. Surf. Sci. Electrochem.*, vol. 3, pp. 338–343, 2018.
- [159] D. Balzar, "X-ray diffraction line broadening: modeling and applications to high-T<sub>c</sub> superconductors," *J. Res. Natl. Inst. Stand. Technol.*, vol. 98, no. 3, p. 321, 1993.
- [160] S. Helmrich, R. Schneider, A. W. Achtstein, A. Arora, B. Herzog, S. M. de Vasconcellos, M. Kolarczik, O. Schöps, R. Bratschitsch, U. Woggon, and N. Owschimikow, "Exciton – phonon coupling in mono- and bilayer MoTe<sub>2</sub>," *2D Mater.*, vol. 5, p. 045007, 2018.
- [161] N. Peimyoo, J. Shang, C. Cong, X. Shen, X. Wu, E. K. L. Yeow, and T. Yu, "Nonblinking, intense two-dimensional light emitter: Monolayer WS<sub>2</sub> Triangles," *ACS Nano*, vol. 7, no. 12, pp. 10985–10994, 2013.
- [162] X. Chen, S. M. Shinde, K. P. Dhakal, S. W. Lee, H. Kim, Z. Lee, and J. H. Ahn, "Degradation behaviors and mechanisms of MoS<sub>2</sub> crystals relevant to bioabsorbable electronics," *NPG Asia Mater.*, vol. 10, no. 8, pp. 810–820, 2018.

## Acknowledgements

First, my upmost gratitude goes to my supervisors Prof. Jüri Krustok and Prof. Maarja Grossberg for their support, guidance, and encouragement over the years.

I want to thank the Head of the Department of Materials and Environmental Technology, Prof. Malle Krunks for providing the opportunity to carry out my doctoral studies in this department.

I am very thankful to my colleagues from the Laboratory of Optoelectronic Materials Physics and from the Laboratory of Photovoltaic Materials Research, for their help during the years. Especially I want to thank Dr. Peter Walke, Dr. Taavi Raadik, Dr. Valdek Mikli, Dr. Jaan Raudoja and Dr. Marit Kauk-Kuusik for useful discussion and support.

I am greatly thankful to Prof. Axel Lorke, Prof. Marika Schleberger, Marcel Ney, Dr. Aswin Asaithambi, Lukas Madauß, Erik Pollmann, André Maas from University of Duisburg-Essen for their collaboration and guidance.

I want to thank my co-authors Dr. Hannu-Pekka Komsa, Prof. Raivo Jaaniso, Prof. Valter Kiisk, Prof. Ilmo Sildos, Dr. Bo Li and Dr. Yongji Gong for their collaboration.

My special thanks goes to the opponents Dr. Levent Gütay and Prof. Toomas Rõõm for finding time to review this thesis.

This work was financially supported by European Union through the European Regional Development Fund, Project TK141, by the institutional research funding IUT 19-28, by the Estonian Research Council grant PRG1023, and by FP7 project CHEETAH, EC grant agreement no. 609788. Part of the equipment used in this work was financed by ASTRA 5-7. This work was partially supported by the ASTRA “TUT Institutional Development Programme for 2016-2022” Graduate School of Functional Materials and Technologies (2014-2020.4.01.16-0032).

Finally, my warmest appreciation goes to my family – Kristiine, Anita, Siiri, Helmut, and Ivo. Thank you for always being there for me.

## Abstract

### Growth and optical properties of two-dimensional transition metal dichalcogenides

This thesis is focused on the photoluminescence (PL) studies of monolayered transition metal dichalcogenides (TMDs),  $\text{MoS}_2$  and  $\text{WS}_2$ . These less than a nanometer thick semiconductor materials have attracted considerable attention because of their interesting physical properties such as a direct bandgap and very high exciton binding energy, meaning the exciton emission can be observed at room temperature. These properties make them suitable for different potential applications in various opto-electronic devices, such as photodetectors, solar cells, and LEDs. The stability of these materials has not been studied very thoroughly; however, it is crucial for future device production. PL spectroscopy was used as the main tool in this work to characterize the optical properties of TMDs. The aim was to grow TMD monolayers by the chemical vapor deposition (CVD) method and then investigate the optical properties of aged or highly defected single-layer TMDs and the overall stability of these monolayers at different temperature conditions.

All studied TMD monolayers were grown by the CVD method on a  $\text{Si/SiO}_2$  substrate. Raman spectroscopy and atomic force microscopy were used to identify monolayered  $\text{MoS}_2$  and  $\text{WS}_2$  flakes.

The B-band emission from the monolayered  $\text{MoS}_2$  sample was investigated in detail by PL spectroscopy. The evolution of the B-band shape upon variable excitation power is well described by a combination of exciton and trion contributions, from which B-trion binding energy of 18 meV has been extracted. The absence of accompanying A-trion emission in the studied samples and the enhanced intensity of the B-band could be ascribed to a fast non-radiative recombination channel arising from the large defect density in the studied samples. It has been found that band-selective recombination channels or the formation of dark/bright trions are possible microscopic scenarios for our observations.

Temperature dependent PL and reflectance contrast spectroscopy were used to study aged  $\text{WS}_2$  monolayers. Aged  $\text{WS}_2$  monolayers were found to have a typical surface roughness about 0.5 nm and, in addition, a high density of nanoparticles (nanocaps) with the base diameter about 30 nm and an average height of 7 nm. The A-exciton of aged monolayers was found to redshift about 24 meV to lower energy compared to the A-exciton in as-grown monolayer at room temperature. This redshift is explained using the local tensile strain concept, where a strain value of 2.1% was calculated for these nanocap regions. Strained nanocaps have lower band gap energy and excitons will funnel into these regions. At  $T = 10$  K, double exciton and trion peaks were revealed in PL spectroscopy. The separation between double peaks was found to be about 20 meV and the origin of higher energy peaks is related to the optical band gap energy fluctuations caused by the random distribution of local tensile strain due to increased surface roughness. In addition, a wide defect-related exciton band  $X_D$  was found at about 1.93 eV in all aged monolayers. It is shown that the theory of localized excitons describes well the temperature dependence of peak position and halfwidth of the A-exciton band. The possible origin of nanocaps was also discussed.

Temperature- and laser power-dependent PL spectroscopy was used to study the properties of the asymmetric defect-bound exciton band  $X_D$  in defective  $\text{WS}_2$  monolayers. Based on PL mapping, a monolayer region with an intensive  $X_D$  band

emission at about 1.9 eV was chosen for further studies. The  $X_D$  band is thermally quenched above 180 K, and the thermal activation energy is found to be  $E_a = 33 \pm 4$  meV. At  $T = 15$  K, the  $X_D$  band intensity reveals a sublinear dependence with increasing excitation power and the peak position shows a blueshift of about 15 meV per decade of laser power. It is shown that the  $X_D$  band is related to the deep defect states within the band gap of  $WS_2$ .

Controlled experiments at high temperatures (up to  $T = 723$  K) in an inert environment were performed on  $WS_2$  monolayers. In contrast to some previous PL studies with conflicting results, we found that the photoluminescent intensity shows a consistent reduction above room temperature. This is accompanied by an almost linear redshift of the PL peak maximum, and a nearly linear increase in the peak width, which is attributed to an enhanced interaction with optical phonons. Moreover, by fitting the photoluminescence integral intensity with an Arrhenius type dependence, we demonstrate that the center of the  $WS_2$  monolayer flake starts to undergo irreversible degradation at a temperature of 573 K in an inert environment. In contrast, regions close to the flake edges with a more intense room temperature PL response, remain stable. The macroscopic PL signal is largely recovered in these regions following subsequent cooling to room temperature.

## Lühikokkuvõte

### Kahedimensionaalsete siirdemetallide dikalkogeniidide kasvatus ning optiliste omaduste uurimine

Antud töö eesmärgiks oli uurida kahemõõtmelisi (2D) pooljuhtmaterjale ( $\text{MoS}_2$  ja  $\text{WS}_2$ ) fotoluminescents-spektroskoopia (PL) abil. Viimaste aastate jooksul on need vähem kui nanomeetri paksused materjalid ärratanud üha enam teadlaste tähelepanu oma väga huvitavate ja kasulike omaduste tõttu. 2D pooljuhtmaterjalid on otsese keelutsooniga ning ebaharilikult kõrge eksitoni seoseenergiaga, mistõttu on neid materjale ergastades võimalik eksitonkiirgust detekteerida ka toatemperatuuril. Eelmainitud omaduste tõttu võivad tulevikus 2D pooljuhtmaterjalid leida rakendust erinevates optoelektronika seadistes, nagu näiteks detektorites, päikseelementides ja valgusdiodides, selleks on aga äärmiselt tähtis nende materjalide stabiilsus. 2D pooljuhtmaterjalide stabiilsust ei ole veel väga põhjalikult uuritud. Antud töö esimeseks eesmärgiks oli kasvatada ühekihilisi  $\text{MoS}_2$  ja  $\text{WS}_2$  keemilise aurusedestuse (CVD) meetodil. Seejärel oli eesmärgiks uurida nii vananenud kui ka suure defektide hulgaga  $\text{MoS}_2$  ja  $\text{WS}_2$  monokihtide optilisi omadusi ning nende materjalide stabiilsust erinevatel temperatuuridel.

Kõik antud töös uuritud ühekihilised  $\text{MoS}_2$  ja  $\text{WS}_2$  olid kasvatatud CVD meetodil ning  $\text{Si/SiO}_2$  alustele.  $\text{MoS}_2$  ja  $\text{WS}_2$  ühekihilise struktuuri kindlaks määramisel kasutati nii Raman spektroskoopiat kui ka aatomjõu-mikroskoopiat.

Ühekihiliselt  $\text{MoS}_2$  uuriti fotoluminescents spektrokooiaga detailselt B-tsoonist lähtuvat kiirgust. B-tsooni spektri kuju muutumist laseri ergastusvõimsuse muutmisel on võimalik seletada B-eksitoni ja B-triioni kiirguste kombinatsioonina. B-triioni seoseenergiaks saime 18 meV. Ühekihiliselt  $\text{MoS}_2$  mõõdetud luminescentspektris aga puudus A-triion, lisaks oli B-tsooni intensiivsus võrdlemisi kõrge. Need nähtused võib omistada kiirele mittekiirguslikule rekombinatsioonikanalile, mis omakorda on seotud kõrge defektide tihedusega uuritud materjalides. Meie tähelepanekuid võib selgitada nii tsoonitundlike rekombinatsioonikanalitega kui ka „tumedate“ triionite moodustumisega.

Vananenud ühekihilise  $\text{WS}_2$  uurimiseks kasutati temperatuurist sõltuvaid fotoluminescentskiirguse ning peegelduskontrasti spektreid. Vananenud ühekihilisel  $\text{WS}_2$  oli tavapärase pinna karedus umbes 0.5 nm, lisaks leidis kihi all ka suure tihedusega nanoosakesi (nanokoonused), mille põhja läbimõõt oli umbes 30 nm ja kõrgus umbes 7 nm. Toatemperatuurine A-eksitoni kiirgus leiti olevat vananenud ühekihilises materjalis 24 meV madalamal energial kui värskest kasvatatud ühekihilises  $\text{WS}_2$ . Spektri punanihke põhjuseks võib pidada lokaalseid tõmbepingeid nanokoonuste piirkonnas, kus tõmbepinge väärtus on umbes 2.1 %. Pinge all olevates nanokoonustes toimub ka keelutsooni kitsenemine, mistõttu tõmmatakse eksitonid just nendesse piirkondadesse. Väga madalatel temperatuuridel ( $T = 10$  K) näitas PL spektri analüüs eksitoni ja triioni piikide lõhenemist kaheks eraldi piigiks. Piikide lõhenemise vahe oli umbes 20 meV. Suuremal energial olevate eksitoni ja triioni piikide olemasolu on seotud optilise keelutsooni laiuse fluktuatsioonidega, mis on tekkinud lokaalse tõmbepinge juhusliku jaotusega suurenenud pinna kareduse tõttu. Lisaks sellele oli igas vananenud ühekihilises  $\text{WS}_2$  lai defektidega seotud eksitoni piik  $X_D$ , mis asus ligikaudu 1.93 eV juures. Näidati, et A-eksitoni kiirguse piigi asukohta ja piigi poollaiuse temperatuursõltuvust on võimalik kirjeldada lokaliseerunud eksitonide teooriaga. Samuti pakuti välja nanokoonuste võimalikud tekkepõhjused.

Suure defektide hulgaga ühekihilises  $\text{WS}_2$  esinevate asümmeetrilise defektidega seotud eksitoni piigi  $X_D$  omaduste uurimiseks kasutati temperatuurist ja laseri võimsusest

sõltuvaid PL spektreid. Fotoluminestsentskiirguse kaardistamisel oli ühekihilisel  $WS_2$  näha piirkond, kus  $X_D$  piik oli kõrge intensiivsusega ja  $X_D$  piigi asukoht oli umbes 1.9 eV juures. Antud piirkond valiti välja järgnevateks uuringuteks. Temperatuursõltuvuse mõõtmistest oli näha, et  $X_D$  piik kustub temperatuuridel üle 180 K, lisaks oli võimalik välja arvutada termiline aktivatsiooni energia  $E_a = 33 \pm 4$  meV. Madalal temperatuuril ( $T = 15$  K)  $X_D$  piigi intensiivsus kasvas sublineaarselt laseri ergastusvõimsuse kasvuga. Samal ajal piigi asukoht nihkus umbes 15 meV suurema energia poole iga laseri võimsuse dekaadi kohta. Töös on näidatud, et  $X_D$  piik on seotud sügavate defektitasemetega  $WS_2$  keelutsoonis.

Ühekihiliste  $WS_2$  stabiilsuse uurimiseks viidi läbi kontrollitud katsed kõrgetel temperatuuridel (kuni  $T = 723$  K) inertgaasi keskkonnas. Varasemalt läbi viidud ning osaliselt vasturääkivatele kõrgetemperatuurse fotoluminestsentskiirguse uuringute tulemustele vastupidiselt, näitasid antud töös läbi viidud katsed, et fotoluminestsentskiirguse intensiivsus kahaneb pidevalt temperatuuri tõustes. Lisaks intensiivsuse kahanemisele, piigi asukoht nihkus väiksemate energiatega poole ning piigi poollaius laienes lineaarselt, mida võib omistada suurenenud vastasmõjule optiliste foononitega. Fotoluminestsentskiirguse integraalse intensiivsuse temperatuursõltuvus näitas, et temperatuuridel üle 573 K inertgaasi keskkonnas hakkab ühekihilise  $WS_2$  keskkohast materjal kaduma. Ühekihilise  $WS_2$  äärealad, kus fotoluminestsentskiirgus oli algselt keskkohaga võrreldes tugevam, jäid aga stabiilseks. Nendes piirkondades jäi fotoluminestsentskiirgus peale mahajahutamist ligikaudselt samaks nagu enne kuumutamist.





## Appendix

### Publication I

Krustok, J., **Kaupmees, R.**, Jaaniso, R., Kiisk, V., Sildos, I., Li, B., Gong, Y. (2017). Local strain-induced band gap fluctuations and exciton localization in aged WS<sub>2</sub> monolayers. *AIP Advances*, 7, 065005



## Local strain-induced band gap fluctuations and exciton localization in aged WS<sub>2</sub> monolayers

J. Krustok,<sup>1,2,a</sup> R. Kaupmees,<sup>2</sup> R. Jaaniso,<sup>3</sup> V. Kiisk,<sup>3</sup> I. Sildos,<sup>3</sup> B. Li,<sup>4</sup> and Y. Gong<sup>5</sup>

<sup>1</sup>*Division of Physics, Tallinn University of Technology, Ehitajate tee 5, 19086 Tallinn, Estonia*

<sup>2</sup>*Department of Materials and Environmental Technology, Tallinn University of Technology, Ehitajate tee 5, 19086 Tallinn, Estonia*

<sup>3</sup>*Institute of Physics, University of Tartu, W. Ostwaldi 1, 50411 Tartu, Estonia*

<sup>4</sup>*Department of Mechanical Engineering, Villanova University, 800 Lancaster Avenue, Villanova, Pennsylvania 19085, USA*

<sup>5</sup>*Department of Materials Science and Engineering, Stanford University, Stanford, California 94305, USA*

(Received 11 April 2017; accepted 26 May 2017; published online 5 June 2017)

Optical properties of aged WS<sub>2</sub> monolayers grown by CVD method on Si/SiO<sub>2</sub> substrates are studied using temperature dependent photoluminescence and reflectance contrast spectroscopy. Aged WS<sub>2</sub> monolayers have a typical surface roughness about 0.5 nm and, in addition, a high density of nanoparticles (nanocaps) with the base diameter about 30 nm and average height of 7 nm. The A-exciton of aged monolayer has a peak position at 1.951 eV while in as-grown monolayer the peak is at about 24 meV higher energy at room temperature. This red-shift is explained using local tensile strain concept, where strain value of 2.1% was calculated for these nanocap regions. Strained nanocaps have lower band gap energy and excitons will funnel into these regions. At T=10K a double exciton and trion peaks were revealed. The separation between double peaks is about 20 meV and the origin of higher energy peaks is related to the optical band gap energy fluctuations caused by random distribution of local tensile strain due to increased surface roughness. In addition, a wide defect related exciton band X<sub>D</sub> was found at about 1.93 eV in all aged monolayers. It is shown that the theory of localized excitons describes well the temperature dependence of peak position and halfwidth of the A-exciton band. The possible origin of nanocaps is also discussed. © 2017 Author(s). All article content, except where otherwise noted, is licensed under a Creative Commons Attribution (CC BY) license (<http://creativecommons.org/licenses/by/4.0/>). [<http://dx.doi.org/10.1063/1.4985299>]

### I. INTRODUCTION

Layered semiconductor compounds involving transition metals from group VI and chalcogens (TMDs) are promising candidates for studying atomically thin structures and have attracted considerable attention because of their unique properties and their potential applications in various opto-electronic devices.<sup>1</sup> The basic building block of these layers consists of one atomic layer of transition metal atoms sandwiched by two chalcogen atomic layers, thus forming one monolayer. All these monolayers have a strong intra layer chalcogen-metal covalent bond while different layers are weakly linked by van der Waals forces. These binary compounds are typically semiconductors with an indirect band gap, while monolayers often have a direct band gap in the visible or near infrared spectral range. The band gap energy of WS<sub>2</sub> bulk crystals is about 0.88 eV, while the monolayer shows an optical bandgap around 2.0 eV.<sup>2</sup> Optical properties of WS<sub>2</sub> monolayers have been studied in many papers.<sup>3-14</sup> The room temperature photoluminescence (PL) spectrum of the WS<sub>2</sub>

<sup>a</sup>E-mail: [Juri.Krustok@ttu.ee](mailto:Juri.Krustok@ttu.ee)



monolayer is characterized by the presence of two exciton peaks that arise from vertical transitions at the K point of the Brillouin zone from a spin-orbit-split valence band to a nearly degenerate conduction band. These PL peaks are called as A and B peaks with peak positions near 2.0 and 2.4 eV, respectively.<sup>15</sup> So the spin-orbit splitting of the valence band is found to be 425 meV in WS<sub>2</sub> monolayer.<sup>16</sup> Besides a neutral A<sup>0</sup> exciton peak a trion (A<sup>-</sup>) peak is often visible at about 43 meV lower energy.<sup>11</sup> At temperatures below T=80K the trion peak usually dominates. However, the actual peak positions of excitons and trions are very sensitive to the preparation method of monolayers. Often monolayers grown by chemical vapor deposition (CVD) on Si/SiO<sub>2</sub> substrates show PL emission at lower energies with respect to monolayers transferred by mechanical exfoliation from bulk crystals or monolayers grown on other substrates.<sup>17,18</sup> The main reason of this redshift is believed to be related to the strain in as-grown monolayers, which is usually released after the monolayer is transferred on the same Si/SiO<sub>2</sub> substrate.<sup>5,19</sup> It was found that the uniaxial tensile strain could cause the red shift of A-exciton peak in WS<sub>2</sub> monolayer at a rate -11.3 meV per % of strain.<sup>5</sup> However, slightly higher values were predicted by theoretical calculations.<sup>19</sup> The origin of the strain in as-grown monolayers is due to the different thermal expansion coefficients (TEC) of WS<sub>2</sub> and SiO<sub>2</sub> substrate. But additional strain could be related to the surface roughness, which is causing a local strain depending on a surface topography. In MoS<sub>2</sub> monolayers this concept was verified by creating artificial atoms<sup>20</sup> or wrinkles<sup>21</sup> on a substrate surface and thus getting very high values of local tensile strain and, accordingly, band gap energy fluctuations. The formation of quite high wrinkles in WS<sub>2</sub> monolayers due to strain relaxation processes was recently reported<sup>22</sup> and the A<sup>0</sup> band was red-shifted in these wrinkled areas due to layer bending. Even in WS<sub>2</sub> monolayers prepared by mechanical exfoliation there is a remarkable inhomogeneous strain across the monolayer's area and spatial non-uniformity of the electron density across the monolayer surface due to oxygen chemisorption.<sup>23</sup> Besides a strain many structural defects exist in CVD-grown WS<sub>2</sub> on Si/SiO<sub>2</sub>. These defects introduce localized states in the bandgap, leading a dramatic decrease in the carrier mobility. It was found that CVD-grown monolayer of WS<sub>2</sub> on Si/SiO<sub>2</sub> substrate shows about 10<sup>3</sup> times lower carrier mobility than mechanically exfoliated samples measured under similar conditions.<sup>24,25</sup> It was also reported, that during CVD growth S-rich and S-poor domains could be formed within WS<sub>2</sub> monolayers with very different properties and this could be also one possible reason of spatial non-uniformity of WS<sub>2</sub> monolayers.<sup>26</sup>

Majority of TMD studies were performed on fresh grown monolayers and usually all these compounds have been considered as air-stable semiconductors under ambient conditions. However, recent studies show that CVD grown TMD monolayers exhibit not so good long-term stability in air and usually large-scale structural and morphological changes can be detected after about 1 year storage at normal laboratory atmosphere.<sup>27</sup> The presence of oxidized metal states and organic adsorbates were detected in aged MoS<sub>2</sub> and WS<sub>2</sub> monolayers. The degradation of monolayers commonly starts from grain boundaries and these oxidation processes can be accelerated by using higher temperatures.<sup>28</sup> Unfortunately, optical properties of aged TMD monolayers have not been studied in detail so far. However, it was reported that the PL intensity of aged WS<sub>2</sub> monolayers grown on sapphire substrate drops noticeably and shows large spatial variations.<sup>27</sup>

In our recent paper<sup>29</sup> optical properties of aged MoSe<sub>2</sub> monolayers were studied. These monolayers showed quite high surface roughness leading to a random distribution of local tensile strain and, thus, spatial optical band gap energy fluctuations. Local band gap minimums are capable of efficient funneling and localization of excitons. It was shown that the model of localized excitons describes well the shape and temperature dependence of excitonic PL band. It is obvious that aging of TMD monolayers is quite complicated and different monolayers can show very different behavior. Therefore aging processes and their effect on optical properties of different TMD monolayers definitely need further studies to clarify the nature aging and to understand exciton localization routes.

In the present work we provide new and additional to Ref. 29 experimental results on optical properties of CVD grown and aged WS<sub>2</sub> monolayers on Si/SiO<sub>2</sub> substrates. We show that also aged WS<sub>2</sub> monolayers exhibit different local strains due to surface topography leading to exciton localization.

## II. EXPERIMENTAL DETAILS

An original tellurium-assisted CVD method was used to synthesize WS<sub>2</sub> layers on Si/SiO<sub>2</sub> substrate under atmospheric pressure in a quartz reaction tube (inner diameter ~ 5 cm). For WS<sub>2</sub> synthesis, mixed W and Te powders were scattered on a Si/SiO<sub>2</sub> substrate. The quartz tube was heated to 500 °C at a rate of 50 °C/min and was then kept at 500 °C for 15 min before cooling. Using W/Te precursor allows growth at temperatures much lower when compared to that of CVD syntheses using WO<sub>3</sub> precursors (~800 °C). The sulfur powder was loaded at the upstream zone inside the same quartz tube with a temperature of about 200 °C. Argon (100 sccm) was used as protection from oxidation and carrier gas during growth. No tellurium containing phases were detected after growth in WS<sub>2</sub> layers. More details of the growth process can be found in the paper by Y. Gong *et al.*<sup>12</sup> WS<sub>2</sub> monolayers used in this study were stored in air under ambient conditions (i.e., room temperature and atmospheric pressure) for about 1 year.

Raman, reflectance contrast (RC) and  $\mu$ PL measurements were carried out using a Horiba LabRAM HR800 Micro-Raman system or a Renishaw inVia Raman microscope (through 50x or 100x objective lenses) equipped with a multichannel CCD detection system in the backscattering configuration with a spectral resolution better than 1 cm<sup>-1</sup>. An Nd-YAG laser (wavelength 532 nm) or an Ar laser (wavelength 488 nm) was used for excitation. The laser spot size was about 2  $\mu$ m in diameter. Linkam THMS350V heating/cooling stage was used for temperature dependent Raman measurements (T=80-300K). For the low temperature (T=10-300K) PL and RC measurements, the UTREKS-LSO cryosystem with the helium-bath cryostat was used. An atomic force microscope (AFM; Bruker Multimode) with a Nanoscope V controller was used to determine the surface roughness and the thickness of the layers.

## III. RESULTS AND DISCUSSION

### A. General properties

The WS<sub>2</sub> monolayers mainly grow as triangular islands with domain sizes up to tens of micrometers (see Fig. 1 (a) (b)). There are also regions where additional 2L and even 3L layers can be observed in the center of some triangles. The thickness of as-grown WS<sub>2</sub> monolayers was measured with AFM and was about 0.8 nm and the sample surface was quite smooth (surface roughness ~0.3 nm).<sup>12</sup> On the contrary, aged WS<sub>2</sub> monolayers have a typical surface roughness about 0.5 nm and, in addition, a high density of nanocaps with the base diameter about 30 nm and average height of 7 nm, see Fig. 1(c). Similar nanocaps were found also in aged MoSe<sub>2</sub> monolayers.<sup>29</sup>

Figure 2 shows the Raman spectra of aged WS<sub>2</sub> monolayer at different temperatures. All Raman spectra measured from different monolayer islands are quite similar and do not differ significantly from the spectra of as-grown layers. The frequency separation of ~60 cm<sup>-1</sup> between E<sub>12g</sub>( $\Gamma$ ) and A<sub>1g</sub>( $\Gamma$ ) modes is typical for single layer WS<sub>2</sub> measured in many papers.<sup>30-33</sup>

At the same time the  $\mu$ PL spectrum of aged WS<sub>2</sub> monolayer is red-shifted about 24 meV, see Fig. 3. It is known that the PL peak position of TMD monolayers is very sensitive to the strain and often CVD grown monolayers show exciton emission at lower energy than monolayers transferred by mechanical exfoliation from bulk crystals. It has been shown that the thermal expansion coefficient (TEC) of WS<sub>2</sub> is smaller than that of the Si/SiO<sub>2</sub> substrate.<sup>34</sup> Therefore, we will expect an in-plane compression stress on WS<sub>2</sub> during cooling after CVD growth and, finally, formation of tensile strain. It was found<sup>19</sup> that the strain affects a band gap energy and also a work function of WS<sub>2</sub>. Often this compressive stress leads to formation of ripples and other local inhomogeneities with different strain values. As it was shown<sup>19</sup> the tensile stress (positive strain) has higher effect on the band gap energy than the compressive stress (negative strain). So it is natural to believe that in our aged monolayers some additional tensile strain is causing this 24 meV red-shift of exciton PL peak and the origin of this extra strain seems to be related to observed nanocaps.

The room temperature  $\mu$ PL spectrum of aged monolayer showed only one slightly asymmetric A-exciton peak. Completely different spectra were obtained at T=10K, see Fig. 4, where 5 different PL bands can be clearly observed. All spectra were fitted using an asymmetric hyperbolic secant function  $I(E) = I_0 [e^{(E-E_M)/W_{HE}} + e^{-(E-E_M)/W_{LE}}]^{-1}$  and the result of this fitting for one spectrum is also shown

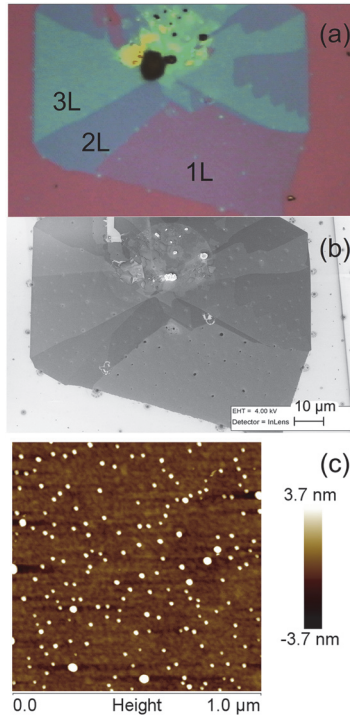


FIG. 1. Optical (a) and SEM (b) microscopy images of  $\text{WS}_2$  layers on  $\text{Si}/\text{SiO}_2$  substrate. The positions of single layer (1L), double (2L) and triple (3L) layers were indicated, (c) the AFM scan from the 1L area.

in Fig. 4. Here  $W_{HE}$  and  $W_{LE}$  are related to the width of high energy and low energy sides of the PL band, respectively, while  $E_M$  is related to the peak position  $E_{max} = E_M - \left[ \frac{W_{HE}W_{LE}}{W_{HE}+W_{LE}} \right] \ln \left( \frac{W_{LE}}{W_{HE}} \right)$ , but only in case of symmetrical band  $E_M = E_{max}$ . The hyperbolic secant function is found to fit well also excitonic PL bands in  $\text{MoSe}_2$  monolayers.<sup>35</sup> Somewhat altered shape and intensity

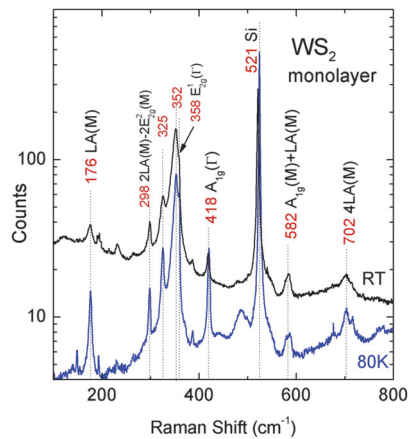


FIG. 2. Room temperature (black) and low temperature ( $T=80\text{K}$ ) (blue) Raman spectra from a  $\text{WS}_2$  monolayer region.

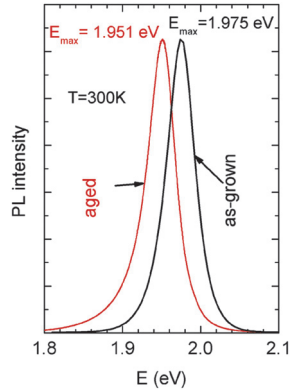


FIG. 3. Normalized room temperature PL spectra of as-grown and aged WS<sub>2</sub> monolayers. The separation between PL peaks is 24 meV.

of the spectra taken from different islands and different positions demonstrate large spatial variations of monolayers properties. At the same time peak positions of all PL bands (except  $X_D$ ) remained almost constant. All PL bands can be divided into 3 groups: A-exciton peaks  $A^0$  ( $E_{max} = 2.030$  eV) and  $A_S^0$  ( $E_{max} = 2.010$  eV); trion peaks  $A^-$  ( $E_{max} = 1.989$  eV) and  $A_S^-$  ( $E_{max} = 1.970$  eV), and a deep defect related exciton peak  $X_D$  ( $E_{max} = 1.93$  eV). Here the subscript S denotes shallow states. The double structure of exciton and trion peaks is rather extraordinary and can be seen merely at very low temperatures ( $T < 30$ K). At higher temperatures only  $A^0$  and  $A^-$  peaks together with  $X_D$  peak persist. The separation between double peaks is about 20 meV. The origin of these peaks will be further discussed later. Rather high intensity of defect related exciton peak  $X_D$  in all monolayer islands is a clear indication of high concentration of defects in aged WS<sub>2</sub> monolayers. We also observed that the high intensity of  $X_D$  peak is usually accompanied by the high intensity of trion peak.

Figure 5 presents the PL spectra of aged WS<sub>2</sub> monolayer measured at  $T=80$ K using different laser power. All spectra were fitted with an asymmetric hyperbolic secant function and the fitting result for 3.5  $\mu$ W spectrum is presented as blue and red lines. The inset shows the integrated intensities of  $A^0$ ,  $A^-$  and  $X_D$  bands as functions of the excitation power. With the increase in the excitation power, the emission from exciton and trion states linearly increases (slope = 1) over the whole studied range.

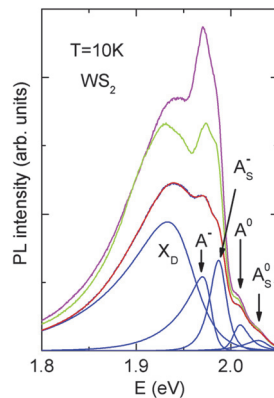


FIG. 4. Low temperature ( $T=10$ K)  $\mu$ PL spectra of WS<sub>2</sub> monolayer island taken from 3 different spots. Result of spectral fitting with an asymmetric hyperbolic secant function is also shown for one spectrum.



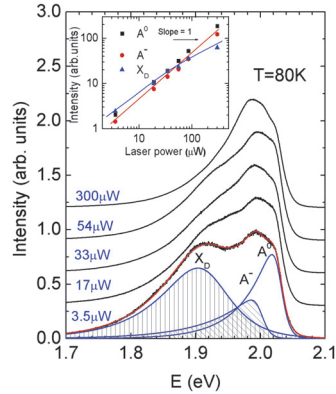


FIG. 5. Excitation intensity dependent normalized PL spectra of aged monolayer WS<sub>2</sub> measured at T=80K and a result of fitting with asymmetric hyperbolic secant function. All spectra are vertically shifted for clarity. The inset shows the integrated intensity of different peaks as a function of laser power.

The emission from  $X_D$  shows a sublinear dependence and saturates at higher excitation power. Similar saturation of the wide  $X_D$  band was observed also in MoS<sub>2</sub><sup>36</sup> and in other WS<sub>2</sub> monolayers.<sup>10</sup> The nature of defects responsible for the  $X_D$  band is not clear, but due to very wide and somewhat variable shape of this band we can expect a presence of several different defects.

## B. Temperature dependence

For temperature dependent RC and  $\mu$ PL measurements we selected monolayer regions, where low-temperature PL intensities of  $X_D$  and trion bands were lowest and, thus, the shape of the  $A^0$  band is more or less well defined. Unfortunately at temperatures  $T < 80$ K the  $X_D$  and trion bands started to appear and the reliability of PL spectral fitting suffers a lot. This was not a case with RC measurements, where spectra were unaffected by trion resonances even at very low temperatures, see Fig. 6 (a). If  $R(E)$  and  $R_0(E)$  are the reflectance spectra of the WS<sub>2</sub> monolayer and the Si/SiO<sub>2</sub> substrate respectively, as a function of the photon energy ( $E$ ), then the RC spectrum is defined as

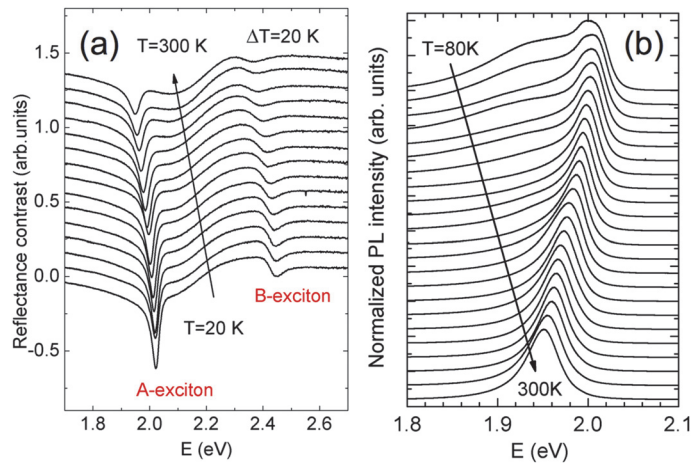


FIG. 6. (a) Temperature dependence of the reflectance contrast spectra of aged WS<sub>2</sub> monolayer showing A and B exciton resonances. (b) Temperature evolution of normalized  $A^0$ -exciton PL emission.

follows:  $RC(E)=[R(E) - R_0(E)]/[R(E)+R_0(E)]$ . As it was shown<sup>37</sup> the inverted reflectance contrast spectra of 2D monolayers near the exciton resonances are usually proportional to the absorption and therefore the shape of inverted RC can be used to probe the density of excitonic states. For the RC peak fitting we used again the asymmetric hyperbolic secant function after subtracting slowly changing background. The asymmetric hyperbolic secant function was used because RC peak had an asymmetric shape with larger width at low energy side. The ratio  $W_{LE}/W_{HE}$  was about 2.5 and did not change with temperature. Both, A and B exciton peaks were detected. The same fitting function was used also for  $\mu$ PL spectra, presented in Fig. 6 (b). Values for peak position  $E_{max}$  and full width at half maximum ( $FWHM$ ) for  $A^0$ -exciton peaks were calculated numerically from fitting curves and are presented in Fig. 7.

The temperature dependence of  $A^0$ -exciton peak position obtained from RC measurements can be well described by a standard semiconductor bandgap model:<sup>38</sup>

$$E_{max} = E(0) - S\hbar\omega [\coth(\hbar\omega/2kT) - 1], \quad (1)$$

where  $E(0)$  is a peak position at  $T=0K$ ,  $S$  is dimensionless electron-phonon coupling strength and  $\hbar\omega$  is an average phonon energy. The fitting result with Eq. (1) is shown as a red line in Fig. 7(a) and parameters found from fitting are given in Table I. Very similar behavior is seen also for B peak, see Fig. 7(a). The separation between A and B exciton peaks is  $\sim 420$  meV and this value is very close to the spin-orbit splitting of the valence band  $425 \pm 18$  meV found for  $WS_2$ .<sup>16</sup> Actually, these fitting parameters are comparable with parameters for  $WS_2$  monolayers obtained by mechanical exfoliation from a bulk crystal and without any strain.<sup>3</sup> However, some discrepancies also exist between the parameters. First,  $E(0)$  values differ about 42 meV. Second, the  $A^0$  exciton peak position found from PL measurements has slightly different behavior, see Fig. 7(a). At lower temperatures the separation between  $A^0$  exciton peaks measured using reflectance contrast (absorption) and PL is increasing and this is typical for localized excitons, where the temperature dependence of peak position often exhibits an S-shape behavior.<sup>39,40</sup>

Figure 7(b) shows the temperature dependence of the full width at half maximum ( $FWHM$ ) of A-exciton line found from reflectance contrast and PL spectra. The linewidth broadening of the A-exciton for RC band was fitted using the relation proposed by Rudin et al.<sup>41</sup> given as

$$FWHM(T) = W_0 + \beta T + \gamma / [\exp(\hbar\omega_{LO}/kT) - 1], \quad (2)$$

where  $W_0$  is a width at  $T=0K$  including also inhomogeneous broadening,  $\beta$  is a coefficient for the interaction of excitons with acoustic phonons and the last term represents the interaction with LO

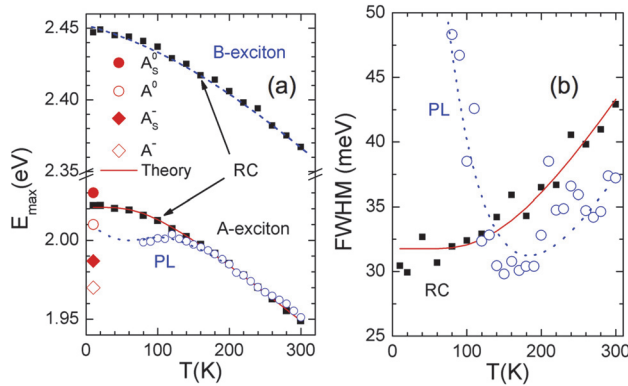


FIG. 7. (a) Temperature dependence of the PL peak energy (blue circles) and peak position of reflectance contrast (RC) spectra (solid squares). Fitting result using Eq. (1) is given with red curve. Peak positions of different PL peaks at  $T=10K$  are also indicated. (b) Temperature dependence of  $FWHM$  of  $A^0$ -exciton peak obtained from RC (solid squares) and PL spectra (circles). Red curve represents the fitting with Eq. (2).

TABLE I. Fitting parameters as obtained from fitting of the temperature dependence of  $E_{max}$  and  $FWHM$  (RC spectra) for  $A^0$ -exciton peak using Eq. (1) and Eq. (2). Fitting results from Ref. 3 are given in parentheses.

Fitting equation	Parameter	Value
Eq. (1)	$E(0)$ (eV)	2.021 (2.063)
	$S$	2.23 (2.4)
	$\hbar\omega$ (meV)	22.7 (31)
Eq. (2)	$\gamma$ (meV)	53.2
	$\hbar\omega_{LO}$ (meV)	44.6
	$W_0$ (meV)	31.8

(longitudinal optical) phonons,  $\hbar\omega_{LO}$  is the LO-phonon energy and is taken to be equal to 44.6 meV for  $WS_2$ .<sup>42</sup> The interaction with acoustic phonons was neglected because it is usually very small. The fitting result is presented in Fig. 7(b) as a red curve and fitting parameters are shown in Table I. At higher temperatures ( $T > 150K$ ) the  $FWHM$  of PL band also shows widening due to electron-phonon interaction, but the width of the PL band seems to be smaller than for RC band. This difference is related to the fact, that the PL spectrum does not represent the total exciton density of states because photoexcited carriers undergo relaxation processes before they recombine radiatively. Therefore the PL spectrum corresponds to distribution of lowest exciton energy states while reflectance contrast spectrum represents the distribution of all exciton states. However, at temperatures  $T < 150K$  the width of the PL band starts to increase rapidly with decreasing of temperature. Moreover, the shape of the PL band near the peak maximum changes and becomes wider, see Fig. 6 (b). This behavior is again typical for localized excitons.<sup>43</sup>

### C. Theory of localized excitons

A general model for the luminescence of localized-state ensemble (LSE) was given by Li et al.<sup>43</sup> According to this work the shape of PL band for localized excitons is asymmetric and can be calculated using density of states function for excitons  $\rho(E)$  and a distribution function  $f(E,T)$  for localized carriers. The  $f(E,T)$  function has a shape resembling a Fermi distribution with a characteristic energy  $E_a$ . The distribution of the localized states  $\rho(E)$  is usually assumed to be described by a Gaussian-like function, but other shapes are also possible. In Ref. 29, for example, the Lorentzian shape was used. According to Ref. 43, the low-energy side of PL band is less affected by the distribution function  $f(E,T)$  and therefore the shape of this side gives a clue about the shape of  $\rho(E)$  function. In our case it is reasonable to approximate function  $\rho(E)$  by hyperbolic secant, because this function was the most suitable one for PL band shape fittings. Then the overall shape of localized excitons PL band is given by:

$$\begin{aligned}
 I(E, T) &= A(T)\rho(E)f(E, T) = \\
 &= \frac{A(T)\rho_0 \operatorname{sech}\left[\frac{E-E_0}{\sigma}\right] (\tau_{tr}/\tau_r)}{\exp\left[\frac{E-E_a}{kT}\right] + \tau_{tr}/\tau_r}, \quad (3)
 \end{aligned}$$

where  $A(T)$  is a temperature dependent term,  $\rho_0$  is the amplitude,  $E_0$  is a peak position and  $\sigma$  is a width of the density of states function,  $I/\tau_r$  and  $I/\tau_{tr}$  represent the rate of radiative recombination and the attempt-to-escape rate of the localized carriers, respectively. The shape calculated by Eq. (3) can be quite well fitted using an asymmetric hyperbolic secant function. At the same time, the shape and the temperature dependence of peak position  $E_{max}$  and  $FWHM$  of localized excitons band significantly depend on  $E_0$  and  $E_a$ . In many cases<sup>43</sup> the best correlation with experimentally measured temperature dependencies is obtained by taking  $E_0 > E_a$ . Figure 8(a) shows calculated by using Eq. (3) PL spectra for the case  $E_0 - E_a = 20$  meV,  $\sigma = 6$  meV and  $\tau_{tr}/\tau_r = 0.1$  and in Fig. 8(b) the temperature dependencies of peak position  $E_{max}-E_0$  and  $FWHM$  are given. It can be seen that the shape of calculated PL band shows very similar behavior to what was observed experimentally, see Figs. 6–8. At temperatures  $T < 150K$  we see a rapid increase of  $FWHM$  and a gradual red-shift of peak position. Furthermore, the shape of the PL band near the peak maximum becomes wider

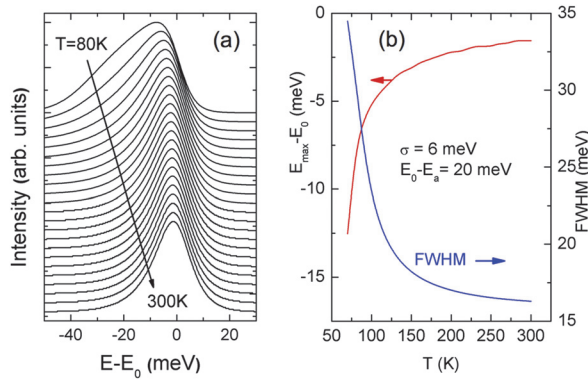


FIG. 8. (a) Calculated temperature dependence of luminescence peak shape (normalized) for the case of  $E_0 - E_a = 20$  meV and  $\sigma = 6$  meV using Eq. (3), (b) the temperature dependence of peak position (red) and FWHM (blue).

and the same trend was observed experimentally, see Fig. 6(b). This means that the LSE model applies to aged WS<sub>2</sub> monolayer and spatial fluctuations of the bandgap energy due to local strain will induce this localization in the lowest-energy regions, where excitons will be swept by the strain-induced potential gradient and funneled toward the center.<sup>44</sup> The LSE model was previously proposed also for WS<sub>2</sub> monolayers grown on a silicon substrate in a hot-wall furnace, where the room temperature PL peak has a maximum at about 1.955 eV.<sup>45</sup> One potential source of the local strain is associated to relatively high nanocaps found by AFM scan on a surface of WS<sub>2</sub> monolayer, see Fig. 1(c). The average distance between these nanocaps is less than the diffusion length of excitons in WS<sub>2</sub> monolayers ( $\sim 350$  nm<sup>46</sup>) and therefore excitons can be easily captured in these regions with high strain and reduced band gap energy. The possible strain  $\varepsilon$  for these nanocaps was obtained from the curvature of nanocaps using the pure-bending equation  $\varepsilon = (d/2)/(R - d/2)$ , where  $R$  and  $d$  are the radius of curvature and the thickness of WS<sub>2</sub> monolayer, respectively.<sup>47</sup> Taking the average thickness of the monolayer  $d = 0.8$  nm, height  $h = 7$  nm and the diameter  $a = 30$  nm of nanocaps, the tensile strain value will be  $\varepsilon = 2.1\%$  and, according to experimentally determined peak position shift of  $-11.3$  meV per % of strain,<sup>5</sup> the overall peak position shift is 23.7 meV. This obtained value is in good correlation with the  $A^0$ -exciton peak position separation between as-grown and aged WS<sub>2</sub> monolayers, see Fig. 3. At low temperatures we also detected additional exciton  $A_S^0$  and trion  $A_S^-$  peaks at higher energies, see Fig. 4. The position of these peaks suggests that they are also related to strained areas, where the band gap energy is about 4 meV less than in as-grown monolayers. This energy corresponds to the strain value of  $\varepsilon = 0.35\%$  and this strain could be caused by the general increase of the surface roughness in aged monolayers. These states are very shallow and excitons are easily thermalized into deeper states when temperature is increased. The whole aged monolayer surface is thus disturbed by the strain having slightly different origin (increased surface roughness vs. nanocaps) and value and therefore we could see emission from localized states only. The recombination model for excitons and trions in aged WS<sub>2</sub> monolayer is given in Fig. 9. At low temperatures the exciton and trion recombination is possible from both deep  $\rho_D$  and shallow  $\rho_S$  localized states showing double peak structure. At higher temperatures only  $\rho_D$  states are active. According to our calculations  $\varepsilon_D = 24$  meV and  $\varepsilon_S = 4$  meV.

The origin of nanocaps in aged monolayer is not clear. It was shown in Ref. 27 that aging usually leads to oxidation of metal states and this process is more prominent at grain boundaries. Sulfur vacancies are similarly believed to play important role in these oxidation processes. It is also possible, that very small nanoparticles were formed on a Si/SiO<sub>2</sub> surface during growth and they are not completely reacted in S atmosphere. Similar nanoparticles were found in many monolayers where they acted as seeds for CVD monolayer growth.<sup>48</sup> During aging these nanoparticles beneath the monolayer start to expand due to oxidation and, as a result, nanocaps are formed. But again, the true origin of these nanocaps is a topic of future studies.

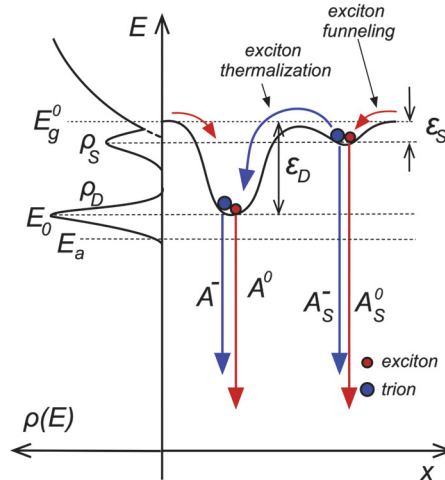


FIG. 9. Proposed recombination model for localized excitons and trions in aged WS<sub>2</sub> monolayers. Density of deep  $\rho_D$  and shallow  $\rho_S$  localized states are shown. The origin of double PL peaks is explained.

#### IV. CONCLUSIONS

We have presented photoluminescence and reflectance contrast spectra of aged WS<sub>2</sub> monolayers, measured at temperatures  $T=10\text{-}300\text{K}$ . Room temperature PL spectra show the A-exciton at 1.951 eV, while in as-grown monolayer the peak was at 24 meV higher energy. We propose that this red-shift is related to the band gap narrowing due to formation of nanocaps and local tensile strain. The local strain value related to nanocaps is about 2.1%. Additional weaker strain ( $\sim 0.35\%$ ) is associated with increased surface roughness in aged monolayers. At  $T=10\text{K}$  double exciton and trion peaks were discovered and we suggest that they are present due to these different strains. In addition, a wide defect related exciton band  $X_D$  was found at about 1.93 eV in all aged monolayers. We showed that the theory of localized-state ensemble can be used to describe well the temperature dependence of peak position and halfwidth of the A-exciton band.

#### ACKNOWLEDGMENTS

This work was supported by institutional research funding IUT 19-28 and IUT 34-27 of the Estonian Ministry of Education and Research, by the European Union through the European Regional Development Fund (Project TK141), and by FP7 project CHEETAH, EC grant agreement no. 609788. Dr. R. Naidu is acknowledged for her help in AFM measurements.

<sup>1</sup> G. Bhimanapati, Z. Lin, V. Meunier, Y. Jung, J. Cha, S. Das, D. Xiao, Y. Son, M. S. Strano, V. R. Cooper, L. Liang, S. G. Louie, E. Ringe, W. Zhou, S. S. Kim, R. R. Naik, B. G. Sumpter, H. Terrones, F. Xia, Y. Wang, J. Terrones, and J. A. Robinson, *ACS Nano* **9**, 11509 (2015).

<sup>2</sup> H. Terrones, F. López-Urías, and M. Terrones, *Sci. Rep.* **3**, 1549 (2013).

<sup>3</sup> K. Wei, Y. Liu, H. Yang, X. Cheng, and T. Jiang, *Appl. Opt.* **55**, 6251 (2016).

<sup>4</sup> T. Kato and T. Kaneko, *ACS Nano* **10**, 9687 (2016).

<sup>5</sup> Y. Wang, C. Cong, W. Yang, J. Shang, N. Peimyoo, Y. Chen, J. Kang, J. Wang, W. Huang, and T. Yu, *Nano Res.* **8**, 2562 (2015).

<sup>6</sup> L. Yuan and L. Huang, *Nanoscale* **7**, 7402 (2015).

<sup>7</sup> A. McCreary, A. Berkdemir, J. Wang, M. A. Nguyen, A. L. Elías, N. Perea-López, K. Fujisawa, B. Kabius, V. Carozo, D. A. Cullen, T. E. Mallouk, J. Zhu, and M. Terrone, *J. Mater. Res.* **31**, 931 (2016).

<sup>8</sup> G. Plechinger, P. Nagler, A. Arora, R. Schmidt, A. Chernikov, A. Granados del Águila, P. C. M. Christianen, R. Bratschitsch, C. Schüller, and T. Korn, *Nat. Commun.* **7**, 12715 (2016).

<sup>9</sup> W. Zhao, Z. Ghorannevis, L. Chu, M. Toh, C. Kloc, P.-H. Tan, and G. Eda, *ACS Nano* **7**, 791 (2013).

<sup>10</sup> J. Shang, X. Shen, C. Cong, N. Peimyoo, B. Cao, M. Eginligil, and T. Yu, *ACS Nano* **9**, 647 (2015).

<sup>11</sup> G. Plechinger, P. Nagler, J. Kraus, N. Paradiso, C. Strunk, C. Schüller, and T. Korn, *Phys. Status Solidi RRL* **9**, 457 (2015).

- <sup>12</sup> Y. Gong, Z. Lin, G. Ye, G. Shi, S. Feng, Y. Lei, A. L. Elías, N. Perea-López, R. Vajtai, H. Terrones, Z. Liu, M. Terrones, and P. M. Ajayan, *ASC Nano* **9**, 11658 (2015).
- <sup>13</sup> A. M. Rivera, A. P. S. Gaur, S. Sahoo, and R. S. Katiyar, *J. Appl. Phys.* **120**, 105102 (2016).
- <sup>14</sup> P. K. Chow, R. B. Jacobs-Gedrim, J. Gao, T.-M. Lu, B. Yu, H. Terrones, and N. Koratkar, *ASC Nano* **9**, 1520 (2015).
- <sup>15</sup> A. T. Hanbickia, M. Curriea, G. Kioseogloub, A. L. Friedmana, and B. T. Jonker, *Solid State Commun.* **203**, 16 (2015).
- <sup>16</sup> D. W. Latzke, W. Zhang, A. Suslu, T.-R. Chang, H. Lin, H.-T. Jeng, S. Tongay, J. Wu, A. Bansil, and A. Lanzara, *Phys. Rev. B* **91**, 235202 (2015).
- <sup>17</sup> L. Su, Y. Yu, L. Cao, and Y. Zhang, *Nano Res.* **8**, 2686 (2015).
- <sup>18</sup> Y. Yu, Y. Yu, C. Xu, Y.-Q. Cai, L. Su, Y. Zhang, Y.-W. Zhang, K. Gundogdu, and L. Cao, *Adv. Funct. Mater.* **26**, 4733 (2016).
- <sup>19</sup> L. Meng, Y. Zhang, S. Hu, X. Wang, C. Liu, Y. Guo, X. Wang, and X. Yan, *Appl. Phys. Lett.* **108**, 263104 (2016).
- <sup>20</sup> H. Li, A. W. Contryman, X. Qian, S. M. Ardakani, Y. Gong, X. Wang, J. M. Weisse, C. H. Lee, J. Zhao, P. M. Ajayan, J. Li, H. C. Manoharan, and X. Zheng, *Nat. Commun.* **6**, 7381 (2015).
- <sup>21</sup> A. Castellanos-Gomez, R. Roldan, E. Cappelluti, M. Buscema, F. Guinea, H. S. J. van der Zant, and G. A. Steel, *Nano Lett.* **13**, 5361 (2013).
- <sup>22</sup> Q. Zhang, Z. Chang, G. Xu, Z. Wang, Y. Zhang, Z.-Q. Xu, S. Chen, Q. Bao, J. Z. Liu, Y.-W. Mai, W. Duan, M. S. Fuhrer, and C. Zheng, *Adv. Funct. Mater.* **26**, 8707 (2016).
- <sup>23</sup> I. Paradisanos, N. Pliatsikas, P. Patsalas, C. Fotakis, E. Kymakis, G. Kioseoglou, and E. Stratakis, *Nanoscale* **8**, 16197 (2016).
- <sup>24</sup> Y.-H. Lee, L. Yu, H. Wang, W. Fang, X. Ling, Y. Shi, C.-T. Lin, J.-K. Huang, M.-T. Chang, C.-S. Chang, M. Dresselhaus, T. Palacios, L.-J. Li, and J. Kong, *Nano Lett.* **13**, 1852 (2013).
- <sup>25</sup> T. Georgiou, H. Yang, R. Jalil, J. Chapman, K. S. Novoselova, and A. Mishchenko, *Dalton Trans.* **43**, 10388 (2014).
- <sup>26</sup> H. Liu, J. Lu, K. Ho, Z. Hu, Z. Dang, A. Carvalho, H. R. Tan, E. S. Tok, and C. H. Sow, *Nano Lett.* **16**, 5559 (2016).
- <sup>27</sup> J. Gao, B. Li, J. Tan, P. Chow, T.-M. Lu, and N. Koratkar, *ACS Nano* **10**, 2628 (2016).
- <sup>28</sup> Y. Rong, K. He, M. Pacios, A. W. Robertson, H. Bhaskaran, and J. H. Warner, *ASC Nano* **9**, 3695 (2015).
- <sup>29</sup> J. Krustok, T. Raadik, R. Jaanisoo, V. Kiisk, I. Sildos, M. Marandi, H.-P. Komsa, B. Li, X. Zhang, Y. Gong, and P. M. Ajayan, *Appl. Phys. Lett.* **109**, 253106 (2016).
- <sup>30</sup> A. Berkdemir, H. R. Gutiérrez, A. R. Botello-Méndez, N. Perea-López, A. L. Elías, C.-I. Chia, B. Wang, V.H. Crespi, F. López-Urías, J.-C. Charlier, H. Terrones, and M. Terrones, *Sci. Rep.* **3**, 1755 (2013).
- <sup>31</sup> C. Cong, J. Shang, X. Wu, B. Cao, N. Peimyoo, C. Qiu, L. Sun, and T. Yu, *Adv. Opt. Mater.* **2**, 131 (2014).
- <sup>32</sup> H. R. Gutiérrez, N. Perea-López, A. L. Elías, A. Berkdemir, B. Wang, R. Lv, F. López-Urías, V. H. Crespi, H. Terrones, and M. Terrones, *Nano Lett.* **13**, 3447 (2013).
- <sup>33</sup> X. Zhang, X.-F. Qiao, W. Shi, J.-B. Wu, D.-S. Jiang, and P.-H. Tan, *Chem. Soc. Rev.* **44**, 2757 (2015).
- <sup>34</sup> Y. Dinga and B. Xiao, *RSC Adv.* **5**, 18391 (2015).
- <sup>35</sup> J. S. Ross, S. Wu, H. Yu, N. J. Ghimire, A. M. Jones, G. Aivazian, J. Yan, D. G. Mandrus, D. Xiao, W. Yao, and X. Xu, *Nat. Commun.* **4**, 1474 (2013).
- <sup>36</sup> S. Tongay, J. Suh, C. Ataca, W. Fan, A. Luce, J. S. Kang, J. Liu, C. Ko, R. Raghunathanan, J. Zhou, F. Ogletree, J. Li, J. C. Grossman, and J. Wu, *Sci. Rep.* **3**, 2657 (2013).
- <sup>37</sup> A. Arora, M. Koperski, K. Nogajewski, J. Marcus, C. Faugeras, and M. Potemski, *Nanoscale* **7**, 10421 (2015).
- <sup>38</sup> K. P. O'Donnell and X. Chen, *Appl. Phys. Lett.* **58**, 2924 (1991).
- <sup>39</sup> A. R. Mohamad, F. Bastiman, C. J. Hunter, R. D. Richards, S. J. Sweeney, J. S. Ng, J. P. R. David, and B. Y. Majlis, *Phys. Status Solidi B* **251**, 1276 (2014).
- <sup>40</sup> Q. Li, S. J. Xu, W. C. Cheng, M. H. Xie, S. Y. Tong, C. M. Che, and H. Yang, *Appl. Phys. Lett.* **79**, 1810 (2001).
- <sup>41</sup> S. Rudin, T. L. Reinecke, and B. Segall, *Phys. Rev. B* **42**, 11218 (1990).
- <sup>42</sup> A. Molina-Sánchez and L. Wirtz, *Phys. Rev. B* **84**, 155413 (2011).
- <sup>43</sup> Q. Li, S. J. Xu, M. H. Xie, and S. Y. Tong, *Europhys. Lett.* **71**, 994 (2005).
- <sup>44</sup> J. Feng, X. Qian, C.-W. Huang, and J. Li, *Nat. Photonics* **6**, 866 (2012).
- <sup>45</sup> X. H. Wang, J. Q. Ning, Z. C. Su, C. C. Zheng, B. R. Zhu, L. Xie, H. S. Wu, and S. J. Xu, *RSC Adv.* **6**, 27677 (2016).
- <sup>46</sup> J. He, D. He, Y. Wang, Q. Cui, F. Ceballos, and H. Zhao, *Nanoscale* **7**, 9526 (2015).
- <sup>47</sup> B. G. Shin, G. H. Han, S. J. Yun, H. M. Oh, J. J. Bae, Y. J. Song, C.-Y. Park, and Y. H. Lee, *Adv. Mater.* **28**, 9378 (2016).
- <sup>48</sup> J. D. Cain, F. Shi, J. Wu, and V. P. Dravid, *ACS Nano* **10**, 5440 (2016).



**Publication II**

**Kaupmees, R.**, Komsa, H.-P., Krustok, J. (2019). Photoluminescence study of B-trions in MoS<sub>2</sub> monolayers with high density of defects. *Physica Status Solidi B*, 256, 1800384





# Photoluminescence Study of B-Trions in MoS<sub>2</sub> Monolayers with High Density of Defects

Reelika Kaupmees, Hannu-Pekka Komsa, and Jüri Krustok\*

Photoluminescence spectroscopy has been used to investigate the details of *B* band emission from single-layer MoS<sub>2</sub> samples grown by chemical vapor deposition. The evolution of the peak shape upon variable excitation power is well described by a combination of exciton and trion contributions, from which *B* trion binding energy of 18 meV has been extracted. It has been suggested that the absence of accompanying *A* trion emission in our samples, as well as the enhanced intensity of the *B* band, can be ascribed to a fast non-radiative recombination channel arising from the large defect density in our samples. It has been found that band-selective recombination channels or formation of dark/bright trions are possible microscopic scenarios for our observations.

## 1. Introduction

The appearance of 2D atomic crystals with various optical and electrical properties has opened up new routes for electronic and optoelectronic device fabrication based on atomically thin layers.<sup>[1,2]</sup> Among them, monolayers of transition metal dichalcogenides (TMDs), such as MoSe<sub>2</sub>, WSe<sub>2</sub>, and MoS<sub>2</sub>, are the most attractive having well-defined semiconductor properties.<sup>[3]</sup> MoS<sub>2</sub> is the most studied TMD atomic crystal, where an atomic plane of Mo atoms is found between two layers of S atoms in a trigonal prismatic structure forming a so-called monolayer.<sup>[4]</sup> In multilayer arrangements, monolayers are stacked together with weak van der Waals interactions between S atoms. While first MoS<sub>2</sub> monolayers were obtained by mechanical exfoliation,<sup>[1]</sup> other methods are proved to be more promising to produce large area and high quality 2D materials to

enable their industrialization. Among them, the chemical vapor deposition (CVD) method is the most popular one and has been successfully demonstrated in synthesis of MoS<sub>2</sub> monolayers and other 2D materials.<sup>[5–12]</sup>

The band structure of MoS<sub>2</sub> converts from an indirect bandgap to a direct one when decreasing its thickness from bulk to a single layer. As a result the photoluminescence (PL) intensity increases remarkably and two PL bands emerge at about 1.8 and 1.95 eV at room temperature.<sup>[13–15]</sup> These bands are called *A* and *B* band, respectively, and they correspond to the direct excitonic transitions at the *K* point in the Brillouin zone, where the *B*

band is related to the spin-orbit split lower valence band. The value of spin-orbit splitting of the valence band in MoS<sub>2</sub> monolayers is  $\Delta E_{SO} = 148$  meV,<sup>[16]</sup> while the splitting of the conduction band is very small and does not exceed 5 meV. The actual peak position of *A* and *B* bands depends on type of the substrate and on quality of monolayers. It has been shown that monolayers grown by CVD on SiO<sub>2</sub>/Si substrates usually show PL bands at lower energy than in exfoliated monolayers<sup>[17,18]</sup> and this is caused by intrinsic tensile strain in MoS<sub>2</sub> monolayer.<sup>[19,20]</sup> The strain and the presence of lattice defects affect not only PL bands, but also the position of Raman peaks of monolayer.<sup>[20–23]</sup> It has been shown that the *A* band at room temperature is often a sum of neutral (*A*<sup>0</sup>) and charged (*A*<sup>−</sup>) exciton emissions.<sup>[24–27]</sup> The charged exciton is called trion and, in principle, it could be either negative (*A*<sup>−</sup>) or positive (*A*<sup>+</sup>) depending on the type of majority carriers. Theoretical calculations show that the same double peak structure is expected also for the *B* band.<sup>[28–30]</sup> Experimentally the *B*<sup>−</sup> trion has been recently observed by reflectance contrast measurements in WSe<sub>2</sub> and MoSe<sub>2</sub>,<sup>[31]</sup> but attempts to detect the existence of *B*<sup>−</sup> (or *B*<sup>+</sup>) trion by PL have not been successful.

In this work, the photoluminescence properties of CVD grown single-layer MoS<sub>2</sub> are investigated by using variable excitation power in order to detect a presence of the *B* trion.


## 2. Experimental Section

MoS<sub>2</sub> monolayers were grown by a CVD method on a Si substrate with a 275 nm thick SiO<sub>2</sub> layer and using MoO<sub>3</sub> and S precursors. For the CVD process, a two-zone furnace was used with S zone at 200 °C and MoO<sub>3</sub> zone at 790 °C. N<sub>2</sub> was used as a carrier gas with a gas flow of 100 sccm. The Si/SiO<sub>2</sub> substrate

R. Kaupmees, Prof. J. Krustok  
Department of Materials and Environmental Technology  
Tallinn University of Technology  
Ehitajate tee 5, 19086 Tallinn, Estonia  
E-mail: juri.krustok@ttu.ee

Dr. H.-P. Komsa  
Department of Applied Physics  
Aalto University  
P.O. Box 11100, 00076 Aalto, Finland

Prof. J. Krustok  
Division of Physics  
Tallinn University of Technology  
Ehitajate tee 5, 19086 Tallinn, Estonia

 The ORCID identification number(s) for the author(s) of this article can be found under <https://doi.org/10.1002/pssb.201800384>.

DOI: 10.1002/pssb.201800384

was positioned face-down at about 2 cm from a MoO<sub>3</sub> precursor. This growth process produced uniform MoS<sub>2</sub> domains and the size of these areas ranges from several tens to more than hundred micrometers. Raman and PL-unpolarized measurements were carried out using a Horiba LabRAM HR800 Micro-Raman system equipped with a multichannel CCD detection system in the backscattering configuration with a spectral resolution better than 1 cm<sup>-1</sup>. An Nd-YAG laser (wavelength 532 nm) was used for excitation. The laser spot size was about 2 μm in diameter. The scanning electron microscope (SEM) HR-SEM Zeiss Merlin was used to study the morphology of monolayers.

### 3. Results and Discussion

Figure 1 shows a SEM picture of the monolayer and the Raman spectrum from the CVD-grown MoS<sub>2</sub>. The Raman peaks associated with MoS<sub>2</sub>, namely, the in-plane mode E' (381.7 cm<sup>-1</sup>) and the out-of-plane mode A<sub>1</sub>' (405.0 cm<sup>-1</sup>) are clearly seen in Figure 1.<sup>[33,34]</sup> The separation between these peaks is Δ = 23.3 cm<sup>-1</sup> and this value is higher than usually observed separation in high quality monolayers (Δ ≈ 19 cm<sup>-1</sup><sup>[34]</sup>). Vertical-dashed lines in Figure 1 mark the peak positions of high quality exfoliated monolayer and, with respect to these lines, our CVD-grown MoS<sub>2</sub> has peaks that are either softened (E') or stiffened (A<sub>1</sub>'), which can be attributed to the presence of substrate-induced tensile strain and charge doping.<sup>[19,35]</sup> The origin of tensile strain in CVD-grown MoS<sub>2</sub> layers has been attributed to the mismatch of the thermal expansion coefficient between the layer and a SiO<sub>2</sub>/Si substrate<sup>[19]</sup> or/and to the surface roughness.<sup>[6,36]</sup> It is known that the lattice tensile strain affects predominantly the in-plane vibration mode E' while the A<sub>1</sub>' mode is relatively unaffected: -2.1 cm<sup>-1</sup> per % strain and -0.4 cm<sup>-1</sup> per % strain, respectively.<sup>[22]</sup> According to these estimations our MoS<sub>2</sub> monolayer seems to have a tensile strain in the range of 1%. However, the shift of E' mode can be also related to high defect

(mostly sulfur vacancies) concentration as was shown in ref. [21]. The blue shift of the A<sub>1</sub>' peak is believed to be a result of hole doping, because, due to the strong interaction between A<sub>1</sub>' phonon and electrons, the A<sub>1</sub>' mode is very sensitive to the doping of MoS<sub>2</sub>.<sup>[37]</sup> High concentration of sulfur vacancies and cracked regions are very active centers for molecular adsorption and, for example, adsorbed O<sub>2</sub> and/or H<sub>2</sub>O can introduce hole doping and thus reduce the electron concentration.<sup>[37]</sup> As it was shown in refs. [19,38,39], the reduced electron concentration leads to a blue shift of the A<sub>1</sub>' peak compared with the peak position in exfoliated high quality monolayer. It was also shown that the nitrogen doping could be an effective way to produce hole doping in MoS<sub>2</sub> monolayers<sup>[40]</sup> by creating N<sub>S</sub> acceptor defects. The presence of weak side peaks at about 409 and 378 cm<sup>-1</sup> (see Figure 1(b)) also confirms a high defect concentration in our monolayer, because these peaks were previously assigned to the defect-induced modes.<sup>[41,42]</sup>

Room temperature PL spectra of our MoS<sub>2</sub> show a clear presence of A and B bands at about 1.79 and 1.95 eV, respectively, see Figure 2. Additional weak band X<sub>D</sub> at 1.69 eV is also visible and it is related to defect bound excitons.<sup>[43]</sup> The relative PL intensity of the B-band was higher than usually observed in high quality MoS<sub>2</sub> monolayers and the overall photoluminescence intensity was also rather weak. In addition, we noticed a faint continuous background emission and it was subtracted during further analysis. All PL bands are red-shifted with respect to peak positions of high quality exfoliated monolayers and this is typical for CVD grown strained MoS<sub>2</sub> on SiO<sub>2</sub>/Si substrates.<sup>[19,44]</sup> At the same time, we did not observe any features corresponding to indirect transition usually visible in multilayers at about 1.5 eV.<sup>[45]</sup> This fact confirms that the red-shift of PL bands is caused by strained and defective MoS<sub>2</sub> monolayer and not by a presence of multilayers. The effect of tensile strain on PL properties of MoS<sub>2</sub> monolayers is studied in many papers and it was found that the decrease in the optical band gap is approximately linear with strain, ≈45 meV per % of strain for monolayer MoS<sub>2</sub>.<sup>[46]</sup>

Later studies showed even higher values, ≈100 meV per % of strain.<sup>[19,36,47]</sup> The peak position of the A-band in exfoliated MoS<sub>2</sub> monolayers is about 1.85 eV<sup>[48]</sup> and therefore we can expect to have ≈0.6% of strain in our monolayer. This strain is smaller than the estimated strain value from Raman measurements and therefore we expect that the shift of Raman peaks is partly caused also by charge doping.

The increase of an excitation intensity leads to nearly linear increase of the A-band intensity while the B-band shows a super-linear increase. Moreover, we noticed a red-shift of the B-band with increasing laser power, but the shape and the peak position of the A-band did not change. All these facts confirm that the A-band does not contain additional trion emission and we observe only emission of neutral excitons A<sup>0</sup>. At the same time, the behavior of the B-band can be explained if both trions and neutral excitons

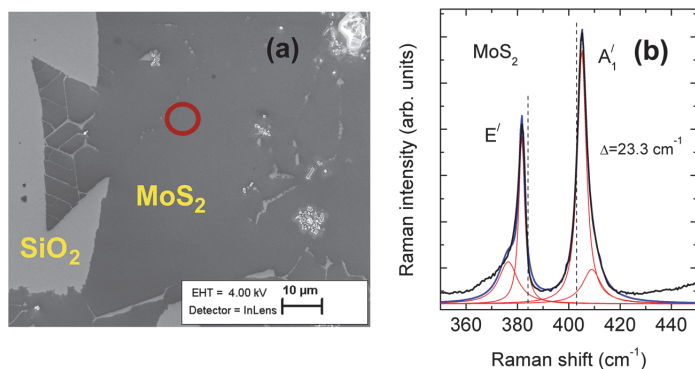


**Figure 1.** a) SEM picture of our MoS<sub>2</sub> monolayer, red circle indicates the location where Raman and PL spectra were measured. b) Raman spectrum from the monolayer area of MoS<sub>2</sub>. Red lines show a result of spectral fitting with Lorentzian curves and blue line is a cumulative fitting result. Vertical dashed lines represent the peak positions measured from high quality exfoliated MoS<sub>2</sub> monolayers.<sup>[32]</sup>

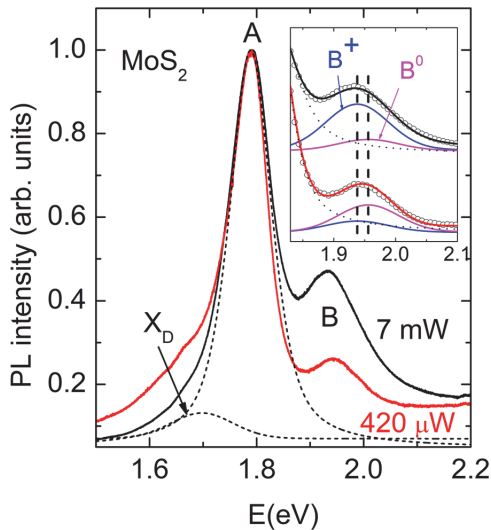


**Figure 2.** Normalized room temperature PL spectra of MoS<sub>2</sub> monolayer measured at different laser power. The inset shows a magnified range of the B-band with fitting results using pseudo-Voigt peak shape function for exciton (B<sup>0</sup>) (magenta line) and trion (B<sup>+</sup>) (blue line) and A-band (dotted curve). Experimental points are presented as circles, fitting results are given with solid black and red lines. Peak positions of B<sup>0</sup> and B<sup>+</sup> are marked with dashed vertical lines. Fitting result for the A-band (at 7 mW) is also shown as dashed lines.

are present. Different properties of A and B bands in our monolayer indicate that electrons in the conduction band play a minor role and holes in both valence bands determine emission properties. Therefore we probably have positive B-trions (B<sup>+</sup>) where two holes are paired with one electron. Accordingly, all PL spectra were fitted using a pseudo-Voigt line shapes for A<sup>0</sup>, B<sup>+</sup>, and B<sup>0</sup>. The separation between our B<sup>0</sup> and B<sup>+</sup> bands was found to be 18 meV and it was kept constant in all fittings. Based on deterioration of the fit upon changing this separation, we estimate the uncertainty of the trion binding energy to be less than 2 meV. By changing the laser excitation intensity over a factor of 150, the peak positions and peak widths (FWHM) of these PL bands did not change indicating no heating of the sample over the range of laser powers used. An example of this fitting for the B band region is shown in Figure 2. At lower laser powers, the B<sup>0</sup> band dominates at 1.956 eV but at higher laser powers we clearly see a rapid increase of the B<sup>+</sup> band at 1.938 eV. The value of spin orbit splitting in our monolayer is found to be  $\Delta E_{SO} = 166$  meV and it is slightly bigger than in high quality monolayers. According to recent first-principles calculations,<sup>[29]</sup> the binding energy of trions in MoS<sub>2</sub> monolayers somewhat depends on substrate and for SiO<sub>2</sub>/Si substrate values 35/32 and 18/17 meV were found for A<sup>-</sup>/A<sup>+</sup> and B<sup>-</sup>/B<sup>+</sup> trions, respectively. The latter agrees very well with our experimental value. Very small binding energy for the B trion explains why it is so difficult to resolve B trion emission while A trion is often visible even at room temperature.

In general, the excitation intensity dependence of the PL intensity is a good indicator of the nature of radiative recombination processes. Specifically, the integral PL intensity, *I*, shows a power law dependence on the laser excitation power, *P*, as  $I \sim P^k$ . A value of  $k \approx 1$  indicates an exciton-like transition and  $k \ll 1$  suggests a recombination path involving defects.<sup>[49]</sup> For trions, where the recombination involves three particles, the intensity should show a  $P^{1.5}$  dependence, i.e., superlinear increase on laser power.<sup>[14]</sup> If both trion and neutral excitons are present, then the increase of B-band intensity must have superlinear dependence with  $1 < k < 1.5$ . The actual value of *k* for each PL band depends also on other conditions like type of a substrate, defect concentration, and crystal quality of monolayers. The dependence of integral intensity of PL bands on laser power is presented in Figure 3. Both neutral excitons (A<sup>0</sup>, B<sup>0</sup>) show nearly linear increase with laser power (note that the B<sup>0</sup>-band seems to have almost the same behavior as the A<sup>0</sup>-band at higher laser power), but the B<sup>+</sup> band increases with  $k = 1.42$ . This value correlates with the expected value for trions ( $k = 1.5$ ). The total intensity of the B-band increases with laser power as  $I \sim P^{1.25}$ .

All properties of our MoS<sub>2</sub> monolayer indicate that we have a very high concentration of defects and quite low carrier concentration. The reason for the fairly intense B-band emission, as compared to those reported in the literature, is therefore assigned to defects. In particular, we assume that there is a non-radiative recombination channel that preferentially acts on the holes in the A-band. This can occur if the traps are energetically close to the valence band maximum, which is responsible for the A-band emission. For example, as it was shown in ref. [50], sulfur adatoms on the surface of MoS<sub>2</sub> layer can introduce a very fast non-radiative recombination channel.

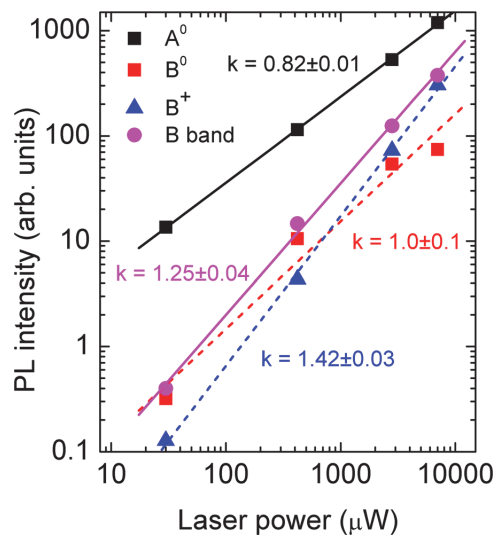


**Figure 3.** Integrated photoluminescence intensity of different PL bands as a function of the laser power plotted on a log–log scale. The lines are least squares fit to the data.

The difference in the relative intensities of trions and excitons in the *A* and *B* bands also appears puzzling. After all, the presence of *B*-trions should imply the presence of free carriers and thereby also of *A*-trions. We speculate on two scenarios for this apparent discrepancy: either the density of *A*-trions or their emission intensity is suppressed. For the former, if there is fast recombination channel for the *A*-excitons, as also assumed above, they will recombine before they can find free carrier and thereby form a trion. Thus, the *A*-trion formation is suppressed. In this scenario, it is irrelevant whether the free carriers are electrons or holes, as long as their concentration is low. The fast recombination channel does not need to be completely non-radiative, but it needs to be selective to *A* to keep the exciton density sufficiently low, while *B*-excitons live longer and form trions. In the latter scenario, the calculated lowest energy *B*<sup>+</sup> trion has one hole in the highest valence band (VB) and one hole in the lower spin-orbit-split band (VB-1). This could in principle show up either as *A*<sup>+</sup> trion or as *B*<sup>+</sup> trion. However, due to the spin orientation in the relevant bands, it is expected to be dark in *A*, but bright in *B*,<sup>[29,51]</sup> and thus shows up more strongly as *B*<sup>+</sup>. The reason for the enhancement of this type of trions over “normal” *A*<sup>+</sup> trions could be ascribed to the same process as in the previous scenario. Alternatively, we could assume there is a fast non-radiative recombination mechanism that affects similarly both conduction band states, but preferentially the VB holes over the VB-1 holes. Then, *B*-exciton is broken via electron trapping and subsequently recombines with VB hole, but a hole is left in the VB-1 state. Since the hole concentration is subsequently reduced at VB state, this essentially leads to transferring the hole concentration from

VB to VB-1. Consequently the trion can be formed even as combination of *A*-exciton and hole at VB-1.

The band structure with all the observed emissions are summarized in **Figure 4**. Following the above discussion, we have also illustrated the possible defect-induced recombination channel in the figure, although at present the exact nature of the defects remains unknown. Also further studies are needed to investigate the properties of *B*-trions in more detail.

## 4. Conclusions

Photoluminescence spectra of our CVD grown MoS<sub>2</sub> monolayer exhibit two predominant bands (*A* and *B*) corresponding to the optical transitions at the *K*-point in the Brillouin zone. High concentration of defects in our sample creates a fast non-radiative recombination channel and additionally reduces a carrier concentration.

While the *A*-band exhibits only specific excitonic properties, the *B*-band has a double structure. The evolution of the *B*-band shape upon variable excitation power is well described by a combination of exciton and trion contributions, from which we extract *B*-trion binding energy of 18 meV.

## Acknowledgments

This work was supported by institutional research funding IUT (IUT19-28) of the Estonian Ministry of Education and Research, by the European Union through the European Regional Development Fund, Project TK141, and the Academy of Finland through project No. 311058. The authors acknowledge fruitful discussion with Dr. Thorsten Deilmann.

## Conflict of Interest

The authors declare no conflict of interest.

## Keywords

chemical vapor deposition, monolayers, MoS<sub>2</sub>, photoluminescence, trions

Received: July 25, 2018  
Revised: September 24, 2018  
Published online: October 8, 2018

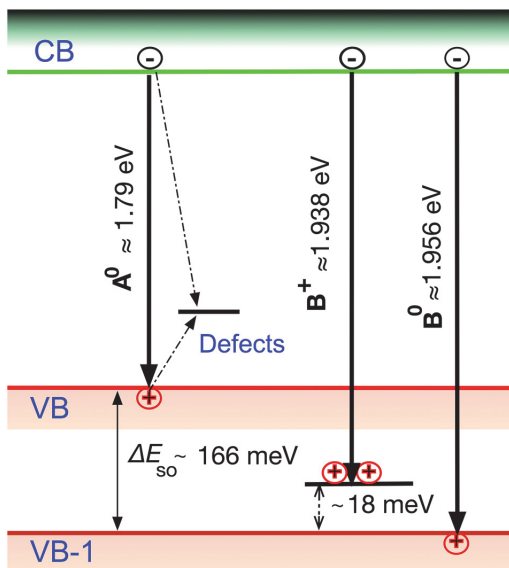


**Figure 4.** The band structure near the *K*-point of the Brillouin zone showing radiative and non-radiative emissions in MoS<sub>2</sub> monolayer.

- [1] K. S. Novoselov, D. Jiang, F. Schedin, T. J. Booth, V. V. Khotkevich, S. V. Morozov, A. K. Geim, *Proc. Natl. Acad. Sci. USA* **2005**, 102, 10451.
- [2] J. Xiao, M. Zhao, Y. Wang, X. Zhang, *Nanophotonics* **2017**, 6, 1309.
- [3] K. F. Mak, C. Lee, J. Hone, J. Shan, T. F. Heinz, *Phys. Rev. Lett.* **2010**, 105, 2.
- [4] Y. P. Venkata Subbaiah, K. J. Saji, A. Tiwari, *Adv. Funct. Mater.* **2016**, 26, 2046.
- [5] Y.-H. Lee, X.-Q. Zhang, W. Zhang, M.-T. Chang, C.-T. Lin, K.-D. Chang, Y.-C. Yu, J. T.-W. Wang, C.-S. Chang, L.-J. Li, T.-W. Lin, *Adv. Mater.* **2012**, 24, 2320.
- [6] J. Krustok, T. Raadik, R. Jaaniso, V. Kiisk, I. Sildos, M. Marandi, H.-P. Komsa, B. Li, X. Zhang, Y. Gong, P. M. Ajayan, *Appl. Phys. Lett.* **2016**, 109, 253106.

- [7] N. Kosku Perkgöz, *Anadolu Univ. J. Sci. Technol. A – Appl. Sci. Eng.* **2017**, *18*, 375.
- [8] J. Xia, X. Huang, L.-Z. Liu, M. Wang, L. Wang, B. Huang, D.-D. Zhu, J.-J. Li, C.-Z. Gu, X.-M. Meng, *Nanoscale* **2014**, *6*, 8949.
- [9] A. Özden, F. Ay, C. Sevik, N. K. Perkgöz, *Jpn. J. Appl. Phys.* **2017**, *56*, 06GG05.
- [10] H. Bergeron, V. K. Sangwan, J. J. McMorro, G. P. Campbell, I. Balla, X. Liu, M. J. Bedzyk, T. J. Marks, M. C. Hersam, *Appl. Phys. Lett.* **2017**, *110*, 53101.
- [11] J. Krustok, R. Kaupmees, R. Jaanisoo, V. Kiisk, I. Sildos, B. Li, Y. Gong, *AIP Adv.* **2017**, *7*, 65005.
- [12] X. Wang, H. Feng, Y. Wu, L. Jiao, *J. Am. Chem. Soc.* **2013**, *135*, 5304.
- [13] A. Splendiani, L. Sun, Y. Zhang, T. Li, J. Kim, C. Y. Chim, G. Galli, F. Wang, *Nano Lett.* **2010**, *10*, 1271.
- [14] D. Kaplan, Y. Gong, K. Mills, V. Swaminathan, P. M. Ajayan, S. Shirodkar, E. Kaxiras, *2D Mater.* **2016**, *3*, 15005.
- [15] K. P. Dhakal, D. L. Duong, J. Lee, H. Nam, M. Kim, M. Kan, Y. H. Lee, J. Kim, *Nanoscale* **2014**, *6*, 13028.
- [16] G.-B. Liu, W.-Y. Shan, Y. Yao, W. Yao, D. Xiao, *Phys. Rev. B* **2013**, *88*, 85433.
- [17] G. Plechinger, J. Mann, E. Preciado, D. Barroso, A. Nguyen, J. Eroms, C. Schüller, L. Bartels, T. Korn, *Semicond. Sci. Technol.* **2014**, *29*, 064008.
- [18] C. R. Zhu, C. Wang, B. L. Liu, X. Marie, X. F. Qiao, X. Zhang, X. X. Wu, H. Fan, P. H. Tan, T. Amand, B. Urbaszek, *Phys. Rev. B* **2013**, *88*, 121301(R).
- [19] W. H. Chae, J. D. Cain, E. D. Hanson, A. A. Murthy, V. P. Dravid, *Appl. Phys. Lett.* **2017**, *111*, 143106.
- [20] R. Roldán, A. Castellanos-Gomez, E. Cappelluti, F. Guinea, *J. Phys.: Condens. Matter* **2015**, *27*, 313201.
- [21] W. M. Parkin, A. Balan, L. Liang, P. M. Das, M. Lamparski, C. H. Naylor, J. A. Rodríguez-Manzo, A. T. C. Johnson, V. Meunier, M. Drndić, *ACS Nano* **2016**, *10*, 4134.
- [22] C. Rice, R. J. Young, R. Zan, U. Bangert, D. Wolverson, T. Georgiou, R. Jalil, K. S. Novoselov, *Phys. Rev. B* **2013**, *87*, 81307.
- [23] Y. Wang, C. Cong, C. Qiu, T. Yu, *Small* **2013**, *9*, 2857.
- [24] K. F. Mak, K. He, C. Lee, G. H. Lee, J. Hone, T. F. Heinz, J. Shan, *Nature Mater.* **2012**, *12*, 207.
- [25] Y. Lin, X. Ling, L. Yu, S. Huang, A. L. Hsu, Y.-H. Lee, J. Kong, M. S. Dresselhaus, T. Palacios, *Nano Lett.* **2014**, *14*, 5569.
- [26] J. W. Christopher, B. B. Goldberg, A. K. Swan, *Sci. Rep.* **2017**, *7*, 14062.
- [27] M. D. Tran, J. H. Kim, Y. H. Lee, *Curr. Appl. Phys.* **2016**, *16*, 1159.
- [28] T. C. Berkelbach, M. S. Hybertsen, D. R. Reichman, *Phys. Rev. B* **2013**, *88*, 45318.
- [29] M. Drüppel, T. Deilmann, P. Krüger, M. Rohlfing, *Nature Commun.* **2017**, *8*, 2117.
- [30] I. Kylänpää, H.-P. Komsa, *Phys. Rev. B* **2015**, *92*, 205418.
- [31] Z. Wang, L. Zhao, K. F. Mak, J. Shan, *Nano Lett.* **2017**, *17*, 740.
- [32] X. Li, H. Zhu, *J. Mater.* **2015**, *1*, 33.
- [33] C. Lee, H. Yan, L. E. Brus, T. F. Heinz, J. Hone, S. Ryu, *ACS Nano* **2010**, *4*, 2695.
- [34] H. Li, Q. Zhang, C. C. R. Yap, B. K. Tay, T. H. T. Edwin, A. Olivier, D. Baillargeat, *Adv. Funct. Mater.* **2012**, *22*, 1385.
- [35] A. Michail, N. Delikoukos, J. Parthenios, C. Galiotis, K. Papagelis, *Appl. Phys. Lett.* **2016**, *108*, 173102.
- [36] H. Li, A. W. Contryman, X. Qian, S. M. Ardakani, Y. Gong, X. Wang, J. M. Weisse, C. H. Lee, J. Zhao, P. M. Ajayan, J. Li, H. C. Manoharan, X. Zheng, *Nature Commun.* **2015**, *6*, 7381.
- [37] H. Nan, Z. Wang, W. Wang, Z. Liang, Y. Lu, Q. Chen, D. He, P. Tan, F. Miao, X. Wang, J. Wang, Z. Ni, *ACS Nano* **2014**, *8*, 5738.
- [38] B. Chakraborty, A. Bera, D. V. S. Muthu, S. Bhowmick, U. V. Waghmare, A. K. Sood, *Phys. Rev. B* **2012**, *85*, 161403.
- [39] A. Bera, D. V. S. Muthu, A. K. Sood, *J. Raman Spectrosc.* **2018**, *49*, 100.
- [40] A. Azcatl, X. Qin, A. Prakash, C. Zhang, L. Cheng, Q. Wang, N. Lu, M. J. Kim, J. Kim, K. Cho, R. Addou, C. L. Hinkle, J. Appenzeller, R. M. Wallace, *Nano Lett.* **2016**, *16*, 5437.
- [41] S. Mignuzzi, A. J. Pollard, N. Bonini, B. Brennan, I. S. Gilmore, M. A. Pimenta, D. Richards, D. Roy, *Phys. Rev. B* **2015**, *91*, 195411.
- [42] D. Wu, H. Huang, X. Zhu, Y. He, Q. Xie, X. Chen, X. Zheng, H. Duan, Y. Gao, *Crystals* **2016**, *6*, 151.
- [43] A. Zafar, H. Nan, Z. Zafar, Z. Wu, J. Jiang, Y. You, Z. Ni, *Nano Res.* **2017**, *10*, 1608.
- [44] Z. Liu, M. Amani, S. Najmaei, Q. Xu, X. Zou, W. Zhou, T. Yu, C. Qiu, A. G. Birdwell, F. J. Crowne, R. Vajtai, B. I. Yakobson, Z. Xia, M. Dubey, P. M. Ajayan, J. Lou, *Nature Commun.* **2014**, *5*, 5246.
- [45] N. Scheuschner, O. Ochedowski, A.-M. Kaulitz, R. Gillen, M. Schleberger, J. Maultzsch, *Phys. Rev. B* **2014**, *89*, 125406.
- [46] H. J. Conley, B. Wang, J. I. Ziegler, R. F. Haglund, S. T. Pantelides, K. I. Bolotin, *Nano Lett.* **2013**, *13*, 3626.
- [47] D. Lloyd, X. Liu, J. W. Christopher, L. Cantley, A. Wadehra, B. L. Kim, B. B. Goldberg, A. K. Swan, J. S. Bunch, *Nano Lett.* **2016**, *16*, 5836.
- [48] Z. Li, S.-W. Chang, C.-C. Chen, S. B. Cronin, *Nano Res.* **2014**, *7*, 973.
- [49] T. Schmidt, K. Lischka, *Phys. Rev. B* **1992**, *45*, 8989.
- [50] L. Li, R. Long, T. Bertolini, O. V. Prezhdo, *Nano Lett.* **2017**, *17*, 7962.
- [51] T. Deilmann, K. S. Thygesen, *Phys. Rev. B* **2017**, *96*, 201113.



**Publication III**

**Kaupmees, R.**, Grossberg, M., Ney, M., Asaithambi, A., Lorke, A., Krustok, J. (2020). Tailoring of bound exciton photoluminescence emission in WS<sub>2</sub> monolayers. *Physica Status Solidi (RRL)*, 14, 1900355





# Tailoring of Bound Exciton Photoluminescence Emission in WS<sub>2</sub> Monolayers

Reelika Kaupmees,\* Maarja Grossberg, Marcel Ney, Aswin Asaithambi, Axel Lorke, and Jüri Krustok

Temperature- and laser power-dependent photoluminescence (PL) properties of the asymmetric defect-bound exciton band  $X_D$  in defective WS<sub>2</sub> monolayers, grown by chemical vapor deposition, are studied. Based on PL mapping, a monolayer region with an intensive  $X_D$  band emission at about 1.9 eV is chosen for further studies. The  $X_D$  band is thermally quenched above 180 K, and the thermal activation energy is found to be  $E_a = 33 \pm 4$  meV. At  $T = 15$  K, the  $X_D$  band intensity reveals a sublinear dependence with increasing excitation power and the peak position shows a blueshift of about 15 meV per decade of laser power. It is shown that the  $X_D$  band is related to the deep defect states within the band gap of WS<sub>2</sub>.

Two-dimensional (2D) semiconductor atomic crystals, also known as transition metal dichalcogenides (TMDs), like MoS<sub>2</sub>, MoSe<sub>2</sub>, WS<sub>2</sub>, and WSe<sub>2</sub>, have attracted considerable attention because of their interesting physical properties and potential applications in various electronic and optoelectronic devices.<sup>[1–5]</sup> For example, monolayered TMDs have the advantage of being direct band gap semiconductors, unlike their 3D counterparts that have an indirect band gap.<sup>[6]</sup> Among these TMDs, WS<sub>2</sub> has the largest band gap in the visible spectral range, around 2.0 eV, and exhibits stronger photoluminescence (PL) emission than most other studied TMDs, making WS<sub>2</sub> atomic crystals excellent candidates for future optoelectronic devices.<sup>[7,8]</sup> The characteristic room temperature PL spectrum of a WS<sub>2</sub> monolayer consists of two excitonic peaks, *A* and *B*, resulting from the large valence band spin–orbit splitting of 425 meV.<sup>[9]</sup> The peak positions of *A* and *B* excitons in WS<sub>2</sub> are around 2.0 and 2.4 eV, respectively.<sup>[10]</sup> These values are found

for mechanically exfoliated WS<sub>2</sub> monolayers, but the peak positions are really sensitive to the preparation method. In the case of WS<sub>2</sub> monolayers grown by chemical vapor deposition (CVD) onto Si/SiO<sub>2</sub> substrates, the *A* and *B* exciton peaks are usually detected at lower energies compared with the mechanically exfoliated layers or CVD-grown layers on other substrates.<sup>[11,12]</sup> This redshift is mostly caused by the strain in the as-grown monolayers on the Si/SiO<sub>2</sub> substrate.<sup>[13–15]</sup> In addition to the charge-neutral  $A^0$  exciton peak, a charged trion  $A^-$  peak is also often found at about 43 meV lower energies.<sup>[16]</sup> At low temperatures ( $T \approx 10$  K), a broad defect-bound

exciton band ( $X_D$ ) with a peak position of about 1.9 eV has been found to dominate the PL spectra.<sup>[17]</sup> This spectral region includes also a single-photon emission (a series of sharp peaks in the defect band region) that has been detected in the low-temperature PL spectra of WS<sub>2</sub> monolayers<sup>[18]</sup> and in other 2D compounds.<sup>[19–21]</sup> Excitons in the defect band region can be bounded to lattice defects.<sup>[22,23]</sup> In addition, Venanzi et al.<sup>[24]</sup> have shown that the defect-bound exciton band consists of excitons that are localized by physisorbed gas molecules on the MoSe<sub>2</sub> monolayer surface. This phenomenon appears also in other TMDs like WS<sub>2</sub>. Still, while *A* and *B* peaks have been studied extensively, the properties of the defect-bound exciton band are not fully understood. We have previously studied<sup>[25]</sup> the luminescence of excitons and trions in CVD-grown WS<sub>2</sub> monolayers and focus on the defect-bound exciton band properties using temperature and excitation power-dependent PL measurements.

WS<sub>2</sub> monolayers mainly grew in triangular islands with domain sizes up to several tens of micrometers; however, other shapes were observed as well. In **Figure 1a**, a scanning electron microscope (SEM) image of CVD-grown butterfly-like WS<sub>2</sub> monolayer is presented. The diameter of this monolayer is about 40  $\mu\text{m}$ . Butterfly-like-shaped WS<sub>2</sub> monolayers have been seen in several studies.<sup>[26–28]</sup> These kinds of monolayers are reported to consist of two symmetrical wings with different atomic orientations, separated by a grain boundary.<sup>[27]</sup> Grain boundary usually includes multiple different misaligned atoms, creating extended defects to the material. The grain boundary area in the middle of the butterfly-shaped WS<sub>2</sub> monolayer is of particular interest, and therefore, it is a subject of this study. To confirm the high concentration of defects in the grain boundary, a room-temperature PL map from the monolayer was created. In **Figure 1b**, the PL peak position map of the  $A^0$  (neutral *A* exciton) peak is presented,

R. Kaupmees, Prof. M. Grossberg, Prof. J. Krustok  
Department of Materials and Environmental Technology  
Tallinn University of Technology  
Ehitajate tee 5, Tallinn 19086, Estonia  
E-mail: reelika.kaupmees@taltech.ee

M. Ney, A. Asaithambi, Prof. A. Lorke  
Faculty of Physics and CENIDE  
University of Duisburg-Essen  
Lotharstr. 1, Duisburg 47057, Germany

Prof. J. Krustok  
Division of Physics  
Tallinn University of Technology  
Ehitajate tee 5, Tallinn 19086, Estonia

 The ORCID identification number(s) for the author(s) of this article can be found under <https://doi.org/10.1002/pssr.201900355>.

DOI: 10.1002/pssr.201900355

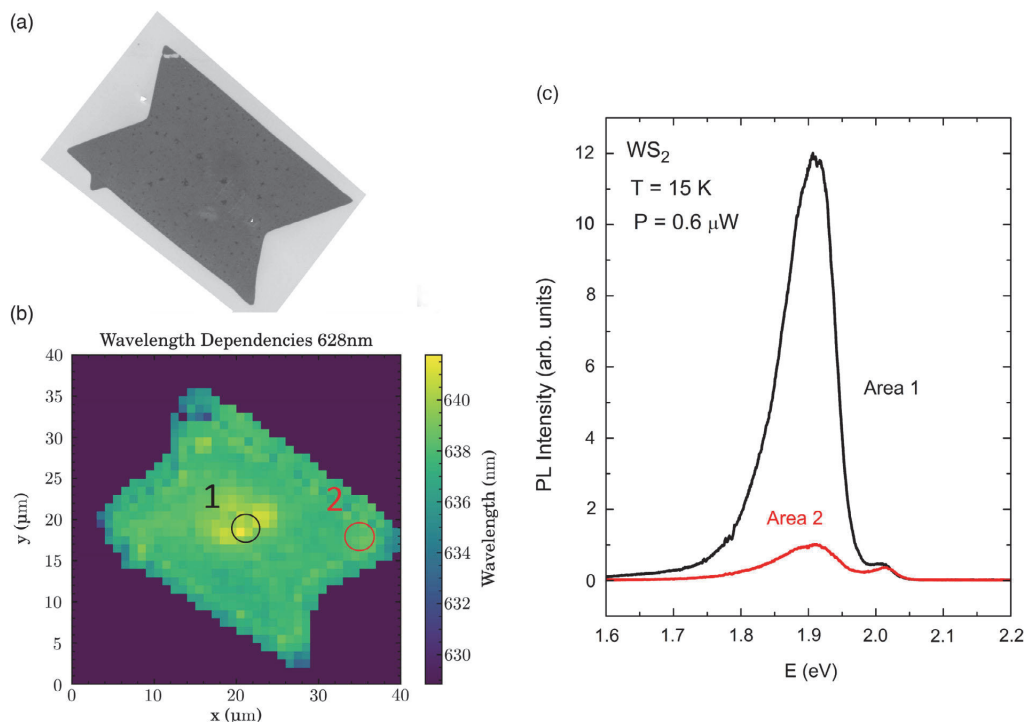


**Figure 1.** a) SEM picture of a butterfly-shaped WS<sub>2</sub> monolayer. b) 2D PL map showing the redshift of the A<sup>0</sup> exciton peak in the middle of the flake. c) Low-temperature ( $T = 15$  K) PL spectra from different WS<sub>2</sub> monolayer areas marked as 1 and 2 in (b).

showing the redshift of the A<sup>0</sup> peak in the middle of the flake. It was shown that the high concentration of defects<sup>[29]</sup> and a possible tensile strain are the main reasons for this kind of peak shift of A<sup>0</sup> excitons in different TMD monolayers.<sup>[14,23,25]</sup> We chose this region with a high-intensity defect-bound exciton PL emission (see Figure 1c) for further studies and the results are presented below.

The room-temperature PL spectrum of this defective region shows only one asymmetrical A<sup>0</sup>-exciton peak at  $E_{\max} = 1.940$  eV (Figure 2a). The peak is shifted to lower energy by about 80 meV when compared with mechanically exfoliated WS<sub>2</sub> monolayers.<sup>[16]</sup> In a previous study,<sup>[25]</sup> we observed an asymmetrical A<sup>0</sup> exciton peak at 1.951 eV in aged CVD-grown WS<sub>2</sub> and showed that, it was redshifted due to tensile strain. The intensity of the A<sup>0</sup> peak from our butterfly-shaped layer was around 100 times higher than the intensity of the A<sup>0</sup> peak from the double-layer WS<sub>2</sub>, confirming that the WS<sub>2</sub> flake studied here is a monolayer.

The Raman spectrum from the CVD-grown WS<sub>2</sub> together with the fitting results is presented in Figure 3a. From the fitting, the positions of the main peaks, the in-plane mode  $E_{2g}^1(\Gamma)$  at  $355.0\text{ cm}^{-1}$  and the out-of-plane mode  $A_{1g}(\Gamma)$  at  $418.3\text{ cm}^{-1}$ , were determined. The separation between these peaks is  $\Delta = 63.3\text{ cm}^{-1}$ . This value is somewhat higher than normally observed in WS<sub>2</sub> monolayers with better quality, where the

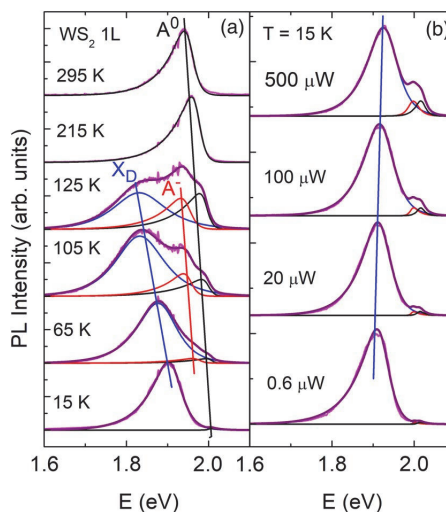


**Figure 2.** Normalized a) temperature and b) laser power dependencies ( $T = 15$  K) of the PL spectrum of a WS<sub>2</sub> monolayer (purple lines). PL-fitting results with asymmetric hyperbolic secant functions are shown. Blue lines show the fitting results for the defect-bound exciton peak X<sub>D</sub>, red lines for the trion peaks A<sup>-</sup>, and black lines for the exciton peaks A<sup>0</sup>.

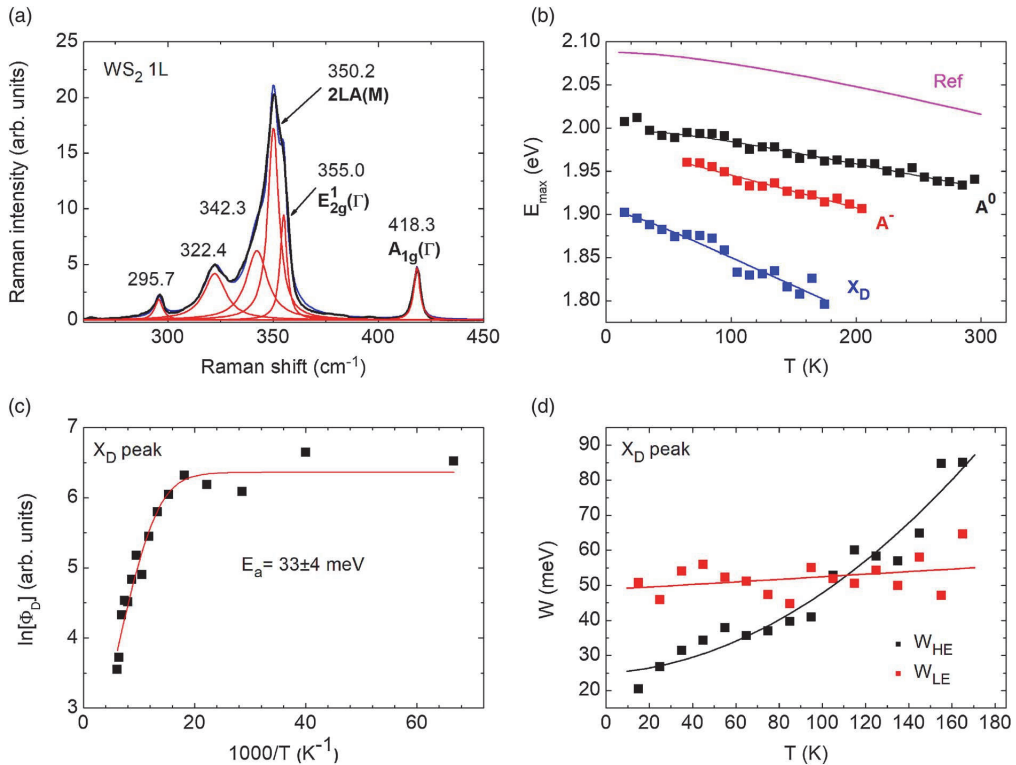


**Figure 3.** a) Raman spectrum from the WS<sub>2</sub> monolayer. Red lines show a result of spectral fitting with Lorentzian curves. The blue line presents the cumulative fitting result. b) Temperature dependence of the PL peak energies. Magenta line represents a temperature dependence of the A<sup>0</sup> peak taken from the study by Plechinger et al.<sup>[16]</sup> c) Arrhenius plot showing the activation energy of the X<sub>D</sub> band. d) The width of high (W<sub>HE</sub>) and low (W<sub>LE</sub>) energy sides of the X<sub>D</sub> band as a function of temperature. The lines are least squares fit to the data.

separation is usually in the range  $\Delta = 61.5\text{--}62.4\text{ cm}^{-1}$  [8,26,30,31]. It is known that the tensile strain in WS<sub>2</sub> monolayers grown on the Si/SiO<sub>2</sub> substrate causes the in-plane Raman mode  $E_{2g}^1(\Gamma)$  to redshift more than the  $A_{1g}(\Gamma)$  peak,<sup>[32]</sup> which increases the separation between these peaks. The dominating mode in Figure 3a is 2LA(M) ( $350.2\text{ cm}^{-1}$ ) that has approximately three times the intensity of the  $A_{1g}(\Gamma)$  mode, which is characteristic for the Raman spectra of WS<sub>2</sub> monolayers, measured with green laser excitation ( $514\text{ nm}$ ,<sup>[30]</sup>  $532\text{ nm}$ <sup>[33]</sup>). This fact and the peak separation value confirm once again that the studied butterfly-like flake is indeed a monolayer. Raman spectra show no dependence on the position on the flake, which indicates the same strain value throughout the flake.

All PL spectra were fitted using an asymmetric hyperbolic secant function:  $I(E) = I_0 / [\exp((E - E_M)/W_{HE}) + \exp(-(E - E_M)/W_{LE})]$ , where  $W_{HE}$  and  $W_{LE}$  are related to the width of high- and low-energy sides of the PL band, respectively, while  $E_M$  is related to the peak position  $E_{max}$ .<sup>[25]</sup> In the case of the symmetrical peak,  $E_M$  is equal to  $E_{max}$ . The asymmetric hyperbolic secant function has been used previously to fit excitonic PL bands in WS<sub>2</sub><sup>[25]</sup> and MoSe<sub>2</sub><sup>[34]</sup> monolayers.

Low laser excitation power ( $5\text{ }\mu\text{W}$ ) was chosen for the temperature-dependent PL measurements ( $T = 15\text{--}295\text{ K}$ ) to have a more pronounced defect-bound exciton band X<sub>D</sub>, compared with the exciton A<sup>0</sup> and trion A<sup>-</sup> peaks. The temperature dependence of some characteristic PL spectra is presented in Figure 2a. An asymmetrical A<sup>0</sup> peak can be seen for the whole temperature range, although at low temperatures, it is relatively weak compared with the X<sub>D</sub> band. The trion peak A<sup>-</sup> appears at  $65\text{ K}$  and disappears above  $205\text{ K}$  (Figure 3b). The X<sub>D</sub> emission band shows an asymmetric lineshape with a sharper high-energy cut-off and an exponential low-energy tail. This band is thermally quenched with increasing temperature and becomes invisible at temperatures above  $180\text{ K}$ , as shown in Figure 3b. Moreover, the X<sub>D</sub> band shows a redshift with increasing temperature and this shift is larger for the exciton and trion peaks, see Figure 3b. The redshift of the A<sup>0</sup> and A<sup>-</sup> peaks with increasing temperature follows the same trend as the exciton peak in strain-free mechanically exfoliated WS<sub>2</sub> monolayers<sup>[16]</sup> shown as a reference in Figure 3b. A similar temperature dependence of the A<sup>0</sup> peak position was found also in the study by Gu et al.<sup>[33]</sup>

The fitting of the PL spectra measured at different temperatures revealed that the width related to the low energy side  $W_{LE}$  of the  $X_D$  band exhibits only a very weak increase with temperature (Figure 3d), whereas the width related to the high energy side  $W_{HE}$  shows a clear temperature dependence. All these features observed for the  $X_D$  band are usually considered as evidence of the disorder-related effects and are also typical for highly doped semiconductors like  $\text{CuInGaSe}_2$ <sup>[35]</sup> or  $\text{Cu}_2\text{ZnSnSe}_4$ .<sup>[36]</sup> As the random fluctuations of defect concentration or strain can cause band gap and electrostatic potential fluctuations, they may smear the band edges and form exponential tails of the density of states extending into the band gap. At low temperatures, excitons can be trapped by the localized states at the band tails, leading to the observed asymmetric lineshape of the PL spectra. In this case, the low-energy tail of the PL band reflects the energy distribution of the density of states within the band tails and has very weak temperature dependence.<sup>[35,37]</sup> At the same time, the high-energy side usually shows typical broadening with increasing temperature,<sup>[35]</sup> see Figure 3d. We therefore conclude that the  $X_D$  band is related to the deep defect states within the band gap and that the PL emission is caused by the excitons bound to these deep defects.

From the temperature dependence of integral intensity, the thermal activation energy  $E_a = 33 \pm 4$  meV was determined for the defect-bound exciton  $X_D$  (Figure 3c) using the following equation<sup>[38]</sup>

$$\Phi(T) = \Phi_0 / [1 + A_1 \exp(-E_a/kT)] \quad (1)$$

where  $\Phi$  is the integral intensity of the PL band,  $A_1$  is the process rate parameter, and  $E_a$  is thermal activation energy. A similar activation energy for the defect-bound exciton has been found not only in  $\text{WS}_2$ <sup>[39]</sup> but also in other TMDs like  $\text{WSe}_2$ <sup>[22,40]</sup> and  $\text{MoS}_2$ .<sup>[41]</sup> When the temperature increases, bound excitons can be thermally activated into delocalized states and captured by the competing nonradiative recombination channels or recombine as free excitons. Therefore, it is expected that the intensity of the bound exciton emission decreases monotonically with increasing temperature. The carriers localized at shallow defect states are first thermally activated to the deeper states, leading to

the redshift of  $X_D$  with increasing temperatures. Correspondingly, at low temperatures, the increasing excitation intensity is expected to cause band filling of the deeper localized energy states, giving rise to a blueshift of the  $X_D$  emission.

The laser excitation power dependence of the PL spectrum was measured at a low temperature ( $T = 15$  K) in the range of  $P = 0.6\text{--}500$   $\mu\text{W}$  to study the nature of radiative recombination processes. In Figure 2b, the power series of the PL spectra are shown and it can be seen that the defect band  $X_D$  strongly dominates over the exciton and trion peaks especially at low laser powers. Furthermore, the  $X_D$  peak energy increases with increasing laser power (a straight blue line in Figure 2b), confirming the expected blueshift, caused by band-filling effects.

The integrated PL intensity  $\Phi$  versus the laser excitation power  $P$  usually follows a power law dependence:  $\Phi \approx P^k$ .<sup>[42]</sup> The integrated PL intensity  $\Phi$  as a function of excitation power  $P$  was investigated for all emission bands at  $T = 15$  K, see Figure 4a. Both, exciton and trion peaks ( $A^0$ ,  $A^-$ ) show nearly linear dependence ( $k \approx 0.9$ ), whereas the emission from the defect-bound exciton band  $X_D$  shows a different dependence and saturates at high excitation powers. It is also observed that the  $X_D$  band blueshifts as the excitation intensity increases and the rate of this shift is about 15 meV per decade of laser power (Figure 4b). This kind of blueshift is usually considered as the evidence of disorder-related effects in semiconductors.<sup>[23,35,43]</sup> We showed before that the random fluctuations of defect concentration or strain can cause band gap and potential fluctuations and form exponential tails in the density of localized states extending into the band gap. At low temperatures, the increasing excitation intensity will cause band filling of the localized energy states, giving rise to the blueshift of  $X_D$  emission.

It was shown theoretically that the PL intensity of the exciton-like transition should follow a power law  $\Phi \approx P^k$  with  $k \approx 1$ . A value  $k \ll 1$  indicates a recombination involving defect states.<sup>[42]</sup> However, the sublinear increase of the intensity of  $X_D$  band with laser power can be explained by the limited concentration of these deep defects leading to the saturation of the intensity of the  $X_D$  band at higher laser powers. A high concentration of deep defects usually leads to steeper increase of the PL intensity reflected by higher values of  $k$ , as reported by different

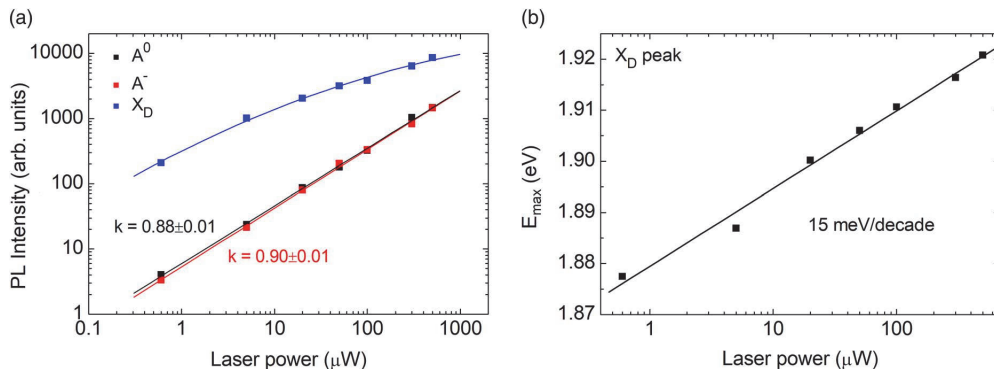


**Figure 4.** a) Integrated PL intensity  $\Phi$  of different PL bands as a function of the laser power, plotted on a log–log scale. The lines are least squares fit to the data. b)  $X_D$  peak position dependence of the laser power. The line is least square fit to the data.

research groups, see for example the study by Shang et al.<sup>[44]</sup> Different  $k$  values for the defect band have been observed also in other materials like  $\text{WSe}_2$ <sup>[22,40]</sup> and  $\text{MoS}_2$ .<sup>[45]</sup> The sublinear dependence of the  $X_D$  band intensity in TMD monolayers was found also in  $\text{WS}_2$ <sup>[25]</sup> and  $\text{MoS}_2$ .<sup>[46]</sup>

The nature of these deep defects is not clear, but our experiments have shown that by using laser annealing, it is possible to reduce the intensity of the  $X_D$  band. The studied  $\text{WS}_2$  monolayer was annealed with a focused laser beam with  $P = 1500 \mu\text{W}$  (power density  $\approx 5 \times 10^8 \text{ W/m}^2$ ) for 5 min at a low temperature ( $T = 15 \text{ K}$ ). To study the effect of annealing, the PL spectra with a laser power of  $0.6 \mu\text{W}$  before and after annealing were compared. Such a low excitation power was used, because the  $X_D$  band was found to be more pronounced when compared with  $A^0$  peak at low laser powers as shown in Figure 2b. Laser irradiation was found to reduce the relative intensity of the defect-bound exciton band about ten times compared with the  $A^0$  exciton peak intensity, indicating that this type of annealing removes some physisorbed gas atoms from the  $\text{WS}_2$  monolayer surface. This effect is rather interesting, suggesting that  $X_D$  band can be sensitive also to other forms of radiation, being useful for some applications. Similar effects have been observed also by other groups.<sup>[47,48]</sup>

The most probable intrinsic defect in the  $\text{WS}_2$  monolayer could be a sulfur vacancy,  $V_S$ , with a reported depth of about  $0.47\text{--}0.6 \text{ eV}$  from the conduction band edge.<sup>[49–51]</sup> At the same time, grain boundaries and adsorbed atoms or molecules on the surface can also play an important role.

In conclusion, the defect-bound exciton band  $X_D$  at  $1.9 \text{ eV}$  was found to dominate the PL spectra of a  $\text{WS}_2$  monolayer at low temperatures. It showed a larger redshift than the  $A^-$  and  $A^0$  peaks with increasing temperature. The width of the low-energy side  $W_{LE}$  of the  $X_D$  band that reflects the energy distribution of the density of the states within the band tails showed a very weak temperature dependence, whereas the high-energy side ( $W_{HE}$ ) demonstrated typical broadening. A thermal activation energy of  $E_a = 33 \pm 4 \text{ meV}$  was found for the  $X_D$  band. The intensity of the  $X_D$  band showed a sublinear dependence with laser power, and a blueshift of about  $15 \text{ meV}$  per decade of laser power was detected for the PL band position. It is proposed that the  $X_D$  band is related to the deep defect-bound excitons and the most probable deep defect could be  $V_S$ , whereas the structural defects and adsorbed atoms could also be the cause of these deep defects.

## Experimental Section

$\text{WS}_2$  monolayers were grown by CVD on a Si substrate with a  $275 \text{ nm}$ -thick  $\text{SiO}_2$  layer using  $\text{WO}_3$  and S precursors. In a two-zone furnace, the temperature in the S zone was  $200^\circ\text{C}$  and in the  $\text{WO}_3$  zone  $850^\circ\text{C}$ . A mix of  $\text{N}_2$  and  $\text{H}_2$  (9%) was used as the carrier gas with a flow rate of  $132 \text{ sccm}$ . The Si/ $\text{SiO}_2$  substrate was placed face down next to the  $\text{WO}_3$  precursor.

Raman measurements were carried out in backscattering configuration using a Horiba LabRAM HR800 Micro-Raman system with a spectral resolution better than  $1 \text{ cm}^{-1}$ , equipped with a cooled multi-channel charge-coupled device (CCD) detection system. A Nd-YAG laser (wavelength:  $532 \text{ nm}$ ) was used for excitation. A  $0.50 \text{ m}$  focal length monochromator ACTON 2500i and an Oxixus - LMX-532 laser (wavelength of  $532 \text{ nm}$ ) with different powers were used for micro-PL measurements. For PL detection, a liquid nitrogen-cooled CCD camera was used. A continuous-flow liquid helium cryostat Janis ST-500 was used for the

temperature-dependent ( $T = 15\text{--}295 \text{ K}$ ) PL measurements. The laser spot size was about  $2 \mu\text{m}$  in diameter for both setups.

The high-resolution SEM HR-SEM Zeiss Merlin was used to study the morphology of monolayers.

## Acknowledgements

This work was supported by institutional research funding IUT (IUT19-28) of the Estonian Ministry of Education and Research and by the European Union through the European Regional Development Fund, Project TK141. A.A. would like to thank the Max Planck Society for providing a doctoral fellowship through IMPRS-SurMat.

## Conflict of Interest

The authors declare no conflict of interest.

## Keywords

chemical vapor deposition, defects, monolayers, photoluminescence,  $\text{WS}_2$

Received: June 19, 2019

Revised: July 17, 2019

Published online: August 14, 2019

- [1] K. S. Novoselov, D. Jiang, F. Schedin, T. J. Booth, V. V. Khotkevich, S. V. Morozov, A. K. Geim, *Proc. Natl. Acad. Sci. USA* **2005**, *102*, 10451.
- [2] H. Tan, Y. Fan, Y. Zhou, Q. Chen, W. Xu, J. H. Warner, *ACS Nano* **2016**, *10*, 7866.
- [3] O. Lopez-Sanchez, D. Lembke, M. Kayci, A. Radenovic, A. Kis, *Nat. Nanotechnol.* **2013**, *8*, 497.
- [4] B. Radisavljevic, A. Radenovic, J. Brivio, V. Giacometti, A. Kis, *Nat. Nanotechnol.* **2011**, *6*, 147.
- [5] S. B. Desai, S. R. Madhupathy, A. B. Sachid, J. P. Llinas, Q. Wang, G. H. Ahn, G. Pitner, M. J. Kim, J. Bokor, C. Hu, H.-S. P. Wong, A. Javey, *Science* **2016**, *354*, 99.
- [6] H. Terrones, F. Lopez-Urias, M. Terrones, *Sci. Rep.* **2013**, *3*, 1549.
- [7] J. Gusakova, X. Wang, L. L. Shiao, A. Krivosheeva, V. Shaposhnikov, V. Borisenko, V. Gusakov, B. K. Tay, *Phys. Status Solidi A* **2017**, *214*, 1700218.
- [8] H. R. Gutiérrez, N. Perea-López, A. L. Elías, A. Berkdemir, B. Wang, R. Lv, F. López-Urías, V. H. Crespi, H. Terrones, M. Terrones, *Nano Lett.* **2013**, *13*, 3447.
- [9] D. W. Latzke, W. Zhang, A. Suslu, T. R. Chang, H. Lin, H. T. Jeng, S. Tongay, J. Wu, A. Bansil, A. Lanzara, *Phys. Rev. B* **2015**, *91*, 235202.
- [10] A. T. Hanbicki, M. Currie, G. Kioseoglou, A. L. Friedman, B. T. Jonker, *Solid State Commun.* **2015**, *203*, 16.
- [11] L. Su, Y. Yu, L. Cao, Y. Zhang, *Nano Res.* **2015**, *8*, 2686.
- [12] Y. Yu, Y. Yu, C. Xu, Y. Q. Cai, L. Su, Y. Zhang, Y. W. Zhang, K. Gundogdu, L. Cao, *Adv. Funct. Mater.* **2016**, *26*, 4733.
- [13] Y. Wang, C. Cong, W. Yang, J. Shang, N. Peimyooy, Y. Chen, J. Kang, J. Wang, W. Huang, T. Yu, *Nano Res.* **2015**, *8*, 2562.
- [14] J. Krustok, T. Raadik, R. Jaanisoo, V. Kiisk, I. Sildos, M. Marandi, H.-P. Komsa, B. Li, X. Zhang, Y. Gong, P. M. Ajayan, *Appl. Phys. Lett.* **2016**, *109*, 253106.
- [15] R. Kaupmees, H. Komsa, J. Krustok, *Phys. Status Solidi B* **2019**, *256*, 1800384.
- [16] G. Plechinger, P. Nagler, J. Kraus, N. Paradiso, C. Strunk, C. Schüller, T. Korn, *Phys. Status Solidi RRL – Rapid Res. Lett.* **2015**, *9*, 457.

- [17] V. Orsi Gordo, M. A. G. Balanta, Y. Galvão Gobato, F. S. Covre, H. V. A. Galeti, F. Iikawa, O. D. D. Couto Jr, F. Qu, M. Henini, D. W. Hewak, C. C. Huang, *Nanoscale* **2018**, *10*, 4807.
- [18] C. Palacios-Berraquero, D. M. Kara, A. R.-P. Montblanch, M. Barbone, P. Latawiec, D. Yoon, A. K. Ott, M. Loncar, A. C. Ferrari, M. Atatüre, *Nat. Commun.* **2017**, *8*, 15093.
- [19] A. Srivastava, M. Sidler, A. V. Allain, D. S. Lembke, A. Kis, A. Imamoglu, *Nat. Nanotechnol.* **2015**, *10*, 491.
- [20] Y. M. He, G. Clark, J. R. Schaibley, Y. He, M. C. Chen, Y. J. Wei, X. Ding, Q. Zhang, W. Yao, X. Xu, C. Y. Lu, J. W. Pan, *Nat. Nanotechnol.* **2015**, *10*, 497.
- [21] P. Tonndorf, R. Schmidt, R. Schneider, J. Kern, M. Buscema, G. A. Steele, A. Castellanos-Gomez, H. S. J. van der Zant, S. Michaelis de Vasconcellos, R. Bratschitsch, *Optica* **2015**, *2*, 347.
- [22] Z. Wu, W. Zhao, J. Jiang, T. Zheng, Y. You, J. Lu, Z. Ni, *J. Phys. Chem. C* **2017**, *121*, 12294.
- [23] Z. Wu, Z. Ni, *Nanophotonics* **2017**, *6*, 1219.
- [24] T. Venanzi, H. Arora, A. Erbe, A. Pashkin, S. Winnerl, M. Helm, H. Schneider, *Appl. Phys. Lett.* **2019**, *114*, 172106.
- [25] J. Krustok, R. Kaupmees, R. Jaaniso, V. Kiisk, I. Sildos, B. Li, Y. Gong, *AIP Adv.* **2017**, *7*, 65005.
- [26] Y. Zhang, Y. Zhang, Q. Ji, J. Ju, H. Yuan, J. Shi, T. Gao, D. Ma, M. Liu, Y. Chen, X. Song, H. Y. Hwang, Y. Cui, Z. Liu, *ACS Nano* **2013**, *7*, 8963.
- [27] Y.-C. Lin, C.-H. Yeh, H.-C. Lin, M.-D. Siao, Z. Liu, H. Nakajima, T. Okazaki, M.-Y. Chou, K. Suenaga, P.-W. Chiu, *ACS Nano* **2018**, *12*, 12080.
- [28] L. Dong, Y. Wang, J. Sun, C. Pan, Q. Zhang, L. Gu, B. Wan, C. Song, F. Pan, C. Wang, Z. Tang, J. Zhang, *2D Mater.* **2019**, *6*, 15007.
- [29] P. K. Chow, R. B. Jacobs-Gedrim, J. Gao, T. M. Lu, B. Yu, H. Terrones, N. Koratkar, *ACS Nano* **2015**, *9*, 1520.
- [30] A. Berkdemir, H. R. Gutiérrez, A. R. Botello-Méndez, N. Perea-López, A. L. Elías, C. I. Chia, B. Wang, V. H. Crespi, F. López-Urías, J. C. Charlier, H. Terrones, M. Terrones, *Sci. Rep.* **2013**, *3*, 1.
- [31] K. M. McCreary, A. T. Hanbicki, G. G. Jernigan, J. C. Culbertson, B. T. Jonker, *Sci. Rep.* **2016**, *6*, 19159.
- [32] A. M. Dadgar, D. Scullion, K. Kang, D. Esposito, E. H. Yang, I. P. Herman, M. A. Pimenta, E. G. Santos, A. N. Pasupathy, *Chem. Mater.* **2018**, *30*, 5148.
- [33] H. Gu, L. Chen, Y. Lu, F. Tian, Z. Zhang, K. Xu, J. Wu, V. D. Botcha, K. Li, X. Liu, *Jpn. J. Appl. Phys.* **2018**, *57*, 60309.
- [34] J. S. Ross, S. Wu, H. Yu, N. J. Ghimire, A. M. Jones, G. Aivazian, J. Yan, D. G. Mandrus, D. Xiao, W. Yao, X. Xu, *Nat. Commun.* **2013**, *4*, 1474.
- [35] J. Krustok, H. Collan, M. Yakushev, K. Hjelt, *Phys. Scr.* **1999**, *T79*, 179.
- [36] M. V. Yakushev, M. A. Sulimov, J. Márquez-Prieto, I. Forbes, J. Krustok, P. R. Edwards, V. D. Zhivulko, O. M. Borodavchenko, A. V. Mudryi, R. W. Martin, *Sol. Energy Mater. Sol. Cells* **2017**, *168*, 69.
- [37] J. Krustok, J. Raudoja, M. Yakushev, R. D. Pilkington, H. Collan, *Phys. Status Solidi A* **1999**, *173*, 483.
- [38] J. Krustok, H. Collan, K. Hjelt, *J. Appl. Phys.* **1997**, *81*, 1442.
- [39] V. Carozo, Y. Wang, K. Fujisawa, B. R. Carvalho, A. McCreary, S. Feng, Z. Lin, C. Zhou, N. Perea-lópez, A. L. Elías, B. Kabius, V. H. Crespi, M. Terrones, *Sci. Adv.* **2017**, *3*, 1602813.
- [40] Z. Wu, Z. Luo, Y. Shen, W. Zhao, W. Wang, H. Nan, X. Guo, L. Sun, X. Wang, Y. You, Z. Ni, *Nano Res.* **2016**, *9*, 3622.
- [41] N. Saigal, S. Ghosh, *Appl. Phys. Lett.* **2016**, *109*, 122105.
- [42] T. Schmidt, K. Lischka, W. Zulehner, *Phys. Rev. B.* **1992**, *45*, 8989.
- [43] A. Jagomägi, J. Krustok, M. Grossberg, M. Danilson, J. Raudoja, *Phys. Status Solidi A* **2006**, *203*, 949.
- [44] J. Shang, X. Shen, C. Cong, N. Peimyoo, B. Cao, M. Eginligil, T. Yu, *ACS Nano* **2015**, *9*, 647.
- [45] J. Shang, C. Cong, X. Shen, W. Yang, C. Zou, N. Peimyoo, B. Cao, M. Eginligil, W. Lin, W. Huang, T. Yu, *Phys. Rev. Mater.* **2017**, *1*, 74001.
- [46] S. Tongay, J. Suh, C. Ataca, W. Fan, A. Luce, J. S. Kang, J. Liu, C. Ko, R. Raghunathanan, J. Zhou, F. Ogletree, J. Li, J. C. Grossman, J. Wu, *Sci. Rep.* **2013**, *3*, 2657.
- [47] Z. He, X. Wang, W. Xu, Y. Zhou, Y. Sheng, Y. Rong, J. M. Smith, J. H. Warner, *ACS Nano* **2016**, *10*, 5847.
- [48] V. Orsi Gordo, M. A. G. Balanta, Y. Galvão Gobato, F. S. Covre, H. V. A. Galeti, F. Iikawa, O. D. D. Couto Jr, F. Qu, M. Henini, D. W. Hewak, C. C. Huang, *Nanoscale* **2018**, *10*, 4807.
- [49] J. Wei, Z. Ma, H. Zeng, Z. Wang, Q. Wei, P. Peng, *AIP Adv.* **2012**, *2*, 42141.
- [50] H. Liu, N. Han, J. Zhao, *RSC Adv.* **2015**, *5*, 17572.
- [51] X. Zhao, X. Dai, C. Xia, T. Wang, *Superlattices Microstruct.* **2015**, *85*, 339.

**Publication IV**

**Kaupmees, R.**, Walke, P., Madauß, L., Maas, A., Pollmann, E., Schleberger, M., Grossberg, M., Krustok, J. (2020). The effect of elevated temperatures on excitonic emission and degradation processes of WS<sub>2</sub> monolayers. *Physical Chemistry Chemistry Physics*, 22, 22609






 Cite this: *Phys. Chem. Chem. Phys.*,  
 2020, 22, 22609

# The effect of elevated temperatures on excitonic emission and degradation processes of WS<sub>2</sub> monolayers

 Reelika Kaupmees,<sup>a</sup> Peter Walke,<sup>a</sup> Lukas Madauß,<sup>b</sup> Andre Maas,<sup>b</sup>  
 Erik Pollmann,<sup>b</sup> Marika Schleberger,<sup>b</sup> Maarja Grossberg<sup>a</sup> and Jüri Krustok<sup>ac</sup>

Controlled heating experiments in an inert environment have been performed on WS<sub>2</sub> monolayers, in order to clarify the conflicting reports on the high-temperature photoluminescent response of 2D TMDs. We find that in contrast to some previous results on both WS<sub>2</sub> and MoS<sub>2</sub>, the photoluminescent intensity shows a consistent reduction above room temperature. This is accompanied by an almost linear redshift of the peak maximum, and a nearly linear increase in the peak width, which is attributed to an enhanced interaction with optical phonons. Moreover, by fitting the photoluminescence integral intensity with an Arrhenius type dependence, we demonstrate that the center of the WS<sub>2</sub> monolayer flake starts to undergo irreversible degradation at a temperature of 573 K in an inert environment. Regions close to flake edges in contrast, with a more intense room temperature PL response, remain stable. The macroscopic PL signal is largely recovered in these regions following subsequent cooling to room temperature.

 Received 17th June 2020,  
 Accepted 21st September 2020

DOI: 10.1039/d0cp03248d

rsc.li/pccp

## Introduction

Two-dimensional (2D) transition metal dichalcogenides (TMDs) have many interesting properties for future flexible optoelectronic and electronic applications.<sup>1,2</sup> These include, but are not limited to, field-effect transistor sensors,<sup>3</sup> field-effect transistors,<sup>4</sup> valley-tronic based devices<sup>5</sup> and photodetectors<sup>6</sup> with the potential for significant performance improvements over the current state of the art. Moreover, specific properties can be tuned by changing the structure, phase or layer-number, whilst phases with mixed stoichiometry and vertical or horizontal heterostructures with other TMDs or 2D materials can all be combined to deliver optimal performance depending on the specific application requirements.

Of the wide variety of TMDs, monolayered WS<sub>2</sub> is particularly promising for many optoelectronic applications as it exhibits the largest direct band-gap<sup>7</sup> and typically the most intense photoluminescence (PL) response.<sup>8</sup> The room temperature PL spectrum of WS<sub>2</sub> is dominated by the so-called A exciton peak, arising from transitions between the lowest conduction and highest valence bands. The peak position of the A exciton of

mechanically exfoliated WS<sub>2</sub> monolayers is found to be at around 2.0 eV.<sup>9</sup> However, the specific position is very sensitive to preparation method and substrate properties. In the case of chemical vapor deposition (CVD) grown WS<sub>2</sub> monolayers on Si/SiO<sub>2</sub>, the built-in strain and altered charge-carrier concentration causes the exciton PL peak to redshift.<sup>10,11</sup> In turn, this strain will usually be relaxed when such monolayers are transferred to another substrate.<sup>12</sup> PL emission intensity is also affected by the defects in monolayers. Their precise influence is complex, and two types of defects, radiative and non-radiative, have been proposed.<sup>13</sup> The radiative defects seem to be concentrated at the edges and at grain boundaries.<sup>14</sup>

An interesting feature of WS<sub>2</sub> and other TMDs is the exceptionally high exciton binding energy,<sup>15</sup> thus making excitonic emission observable at high temperatures. Indeed, Li *et al.*<sup>16</sup> have proposed that MoS<sub>2</sub> monolayers can be used in opto-electronics devices with elevated working temperature. However, a variety of contrasting phenomena have so far been observed through high temperature PL experiments of the A exciton peak. For example, an increase in PL intensity with temperature,<sup>16,17</sup> an increase followed by a subsequent decrease,<sup>16</sup> or a monotonic decrease with increasing temperature,<sup>18</sup> have all been previously reported from temperature dependent PL measurements on monolayer MoS<sub>2</sub>.

Other systems have similarly shown contradictory behavior. PL enhancement at temperatures above 300 K has been observed also in few-layer WSe<sub>2</sub><sup>19</sup> and in multi-layered WS<sub>2</sub>,<sup>20</sup> whilst Chen *et al.*<sup>17</sup> also reported a transient high temperature

<sup>a</sup> Department of Materials and Environmental Technology,  
 Tallinn University of Technology, Ehitajate tee 5, 19086 Tallinn, Estonia.  
 E-mail: reelika.kaupmees@taltech.ee

<sup>b</sup> Faculty of Physics and CENIDE, University of Duisburg-Essen, Lotharstr. 1,  
 Duisburg 47057, Germany

<sup>c</sup> Division of Physics, Tallinn University of Technology, Ehitajate tee 5,  
 19086 Tallinn, Estonia

increase of PL intensity in single-layer WS<sub>2</sub> following an initial decrease above room temperature, although this was then followed again by a subsequent decrease with further increase in temperature. These results are unusual given the typical reduction of PL intensity of semiconductors at elevated temperatures. In contrast Gaur *et al.*<sup>21</sup> have shown a decrease in PL intensity at all stages of temperature increase from 83–473 K for WS<sub>2</sub> flakes grown on sapphire. Similar behavior was also seen by Su *et al.*,<sup>22</sup> who noted a red-shift in peak position and decrease in intensity for both an irregularly shaped film grown on Si/SiO<sub>2</sub> and a monolayer grown on sapphire. Finally, the integrated PL intensity has been observed to decrease in vertically stacked WS<sub>2</sub>/MoS<sub>2</sub> monolayer heterostructures at temperatures above room temperature due to the thermally activated non-radiative recombination mechanism.<sup>23</sup>

Furthermore, high temperature measurements are also necessary for establishing operating conditions in future applications, many of which will practically involve elevated working temperatures, as well as quantifying changes to photophysical parameters beyond intensity that may be incurred in such situations. Moreover, degradation of TMDs has been seen at high temperatures. In monolayered MoS<sub>2</sub>, small triangular holes appear in systems subjected to a hydrogen and argon mixed atmosphere at around 773 K<sup>24</sup> and grain boundary degradation has been seen when heated in air.<sup>25</sup> Still, while the PL properties of WS<sub>2</sub> monolayers at low temperatures have been studied extensively in multiple papers such as ref. 11 and 26, there are only a few studies about high temperature PL measurements and even less information about degradation of flakes at elevated temperatures and in different atmospheres. Taken with the conflicting accounts of the temperature-dependent photoluminescent response of TMD monolayers, this points to a need for further clarification, both to provide greater mechanistic insights and to establish maximal device operating conditions.

Herein, we focus on the properties of WS<sub>2</sub> monolayers using PL measurements at elevated temperatures, and how these temperatures consequently affect the degradation of the flakes. We clarify the high-temperature photoluminescent response of the monolayer, and detail the induced irreversible changes upon return to room temperature. Our work shall serve as a basis for further fundamental and applied studies on 2D TMDs at high temperatures.

## Experimental

### CVD growth

WS<sub>2</sub> monolayers were fabricated using a multi-zone split tube furnace with thermally separated heating zones (ThermConcept, ROK 70/750/12-3z). The substrates were Si/SiO<sub>2</sub> wafers. First, ammonium tungsten oxide hydrate (ATH) was dissolved in deionized water. The solution with 1000 g l<sup>-1</sup> was transferred onto a first substrate in several little droplets of ~1 mm in diameter. Subsequently, the substrate was heated under ambient atmosphere at 500 °C for 30 min to convert ATH into the tungsten source WO<sub>3</sub>. Afterwards, cholic acid sodium salt (CAS) was spin coated as the seeding promoter onto the substrate containing

WO<sub>3</sub> as well as onto a second otherwise clean substrate. The substrate with WO<sub>3</sub> was put into a crucible, the second substrate – only with seeding promoter – was flipped and put upside down onto the first one. The crucible containing the substrate and the tungsten source was put into the center heating zone and a second crucible filled up with 100 mg sulfur was put into the heating zone upstream. After sealing, the tube was purged with Ar gas. For the CVD process the Ar flow rate was set to 50 sccm. The central heating zone was heated to 825 °C in 20 min and the sulfur heating zone to 150 °C in 10 min after a delay of 10 min. After holding the maximum temperatures for 30 min, the furnace was opened for rapid cooling.

### Characterization

Raman, reflectance contrast (RC) and  $\mu$ -PL measurements were carried out using a Horiba LabRAM HR800 Micro-Raman system equipped with a multichannel CCD detection system in the backscattering configuration with a spectral resolution better than 1 cm<sup>-1</sup>. A continuous wave Nd-YAG laser (wavelength 532 nm) was used for excitation. Excitation powers used in the study were 0.03–0.42 mW. Two different objectives were used for measurements: a 10 $\times$  long-working-distance lens (NA = 0.25) with bigger laser spot size (approximately marked as area 1 in Fig. 3(a)) and a 50 $\times$  long-working-distance lens (NA = 0.50) with smaller laser spot size (approximately marked as area 2 in Fig. 3(a)). The used laser beam was linearly polarized and therefore the sample orientation was kept constant during the temperature dependent PL measurements. A Linkam THMS600 heating/cooling stage was used for temperature dependent PL measurements ( $T = 298$ –723 K). Before measurements, the cryostat was flushed with Ar gas for approximately 10 minutes and after that the valves were closed. The pressure at room temperature was around 2 atm. While the sample was heated, the cryostat housing had a water-cooling system. Samples were heated with a 10 K min<sup>-1</sup> rate and were held at desired temperatures for at least 5 min to let the sample temperature to stabilize. Measurements were performed in an argon atmosphere, preventing WS<sub>2</sub> flakes from oxidizing. An atomic force microscope (AFM; Bruker Multimode) with a Nanoscope V controller was used to determine the thickness of the layers. PL imaging was carried out on a microscope unit with a high-power 420 nm light emitting diode (Thorlabs M420L3) for wide-field excitation and for detection through a 50 $\times$  objective a cooled Atik 414EX CCD camera (filters to remove excitation emission were employed).

## Results and discussion

CVD grown WS<sub>2</sub> monolayers exhibited a variety of different shapes with the average domain size around 100  $\mu$ m. An atomic force microscope was used to determine the thickness of the monolayers, which was found to be about 0.8 nm (Fig. 1(a and b)), a typical value for TMD monolayers.<sup>21</sup> This finding was supported by initial optical characterization by Raman spectroscopy. A Raman spectrum was measured from the area 2, in Fig. 3(a) and the results are presented in Fig. 1(c). From the Raman fitting the

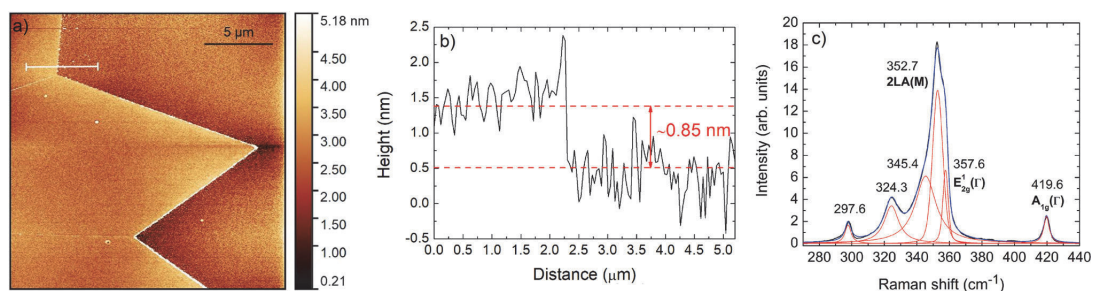


Fig. 1 AFM height image (a) and AFM line profile (b) showing typical  $\text{WS}_2$  monolayer thickness. The line profile was taken along the white line shown in (a). Raman spectrum (c) from the  $\text{WS}_2$  monolayer. Red lines show the result of spectral fitting using Lorentzian curves.

peak positions of the main peaks, the in-plane mode  $E_{2g}^1(T)$  at  $357.6 \text{ cm}^{-1}$  and the out-of-plane mode  $A_{1g}^1(T)$  at  $419.6 \text{ cm}^{-1}$  were determined. The separation of these peaks is  $\Delta = 62.0 \text{ cm}^{-1}$ , which is in the same range ( $\Delta = 61.5\text{--}62.4 \text{ cm}^{-1}$ ) previously found in good quality  $\text{WS}_2$  monolayers.<sup>8,27–29</sup> Additionally, a strong peak assigned to a second-order contribution (2LA(M)) was also seen at  $352.7 \text{ cm}^{-1}$ , as is typical for measurements on  $\text{WS}_2$  monolayers under near-resonance conditions.<sup>29</sup>

Fig. 2(b) shows a PL image of a  $\text{WS}_2$  polycrystalline monolayer flake and Fig. 2(b) shows a PL image of the same flake after it was heated in an Ar atmosphere up to  $T = 643 \text{ K}$ , detailing the formation of cracks along the grain boundaries.  $\text{WS}_2$  flakes started to be thermally unstable at around  $T = 573 \text{ K}$  as was seen in the optical microscope. One reason for this cracking could be the different thermal expansion of the substrate and the  $\text{WS}_2$  monolayer.<sup>12</sup> Although this should not play such a big role, because the CVD growth temperature is  $T = 1073 \text{ K}$  and the material can handle temperature difference between growth and room temperatures, so the stress at  $T = 573 \text{ K}$  should not have such an effect. However, defects at grain boundaries can affect the material loss. This phenomenon has been seen also in  $\text{MoS}_2$  monolayers heated in air.<sup>25</sup>

As shown in Fig. 2(a) grain boundaries and their degradation at higher temperature can have a crucial influence on the PL emission. For further PL studies an equilateral triangular shaped  $\text{WS}_2$  flake was chosen. This type of flake is monocrystalline and

without visible grain boundaries, unlike other shapes, in which original monocrystalline flakes have ripened into a larger irregular structure with internal grain boundaries.<sup>30</sup> The following PL temperature dependence study was carried out with a  $10\times$  objective (NA = 0.25), so the laser spot would cover a maximum area and thus the spatial variations in the flake are averaged with the surrounding region (see area 1 in Fig. 3(a)). To study the PL response of the area where the monolayer is still intact after the temperature dependence study (Fig. 3(b)) a  $50\times$  objective (NA = 0.50) was used (see area 2). The initial room temperature PL image in Fig. 3(a) shows that the PL intensity across the monolayer is non-uniform. As has been previously reported, the center of the crystal shows lower PL intensity than the areas close to the edges,<sup>13</sup> with this region of lower intensity also extending symmetrically from the center towards the vertices.

The temperature dependence of some PL spectra is presented in Fig. 4(a). All temperature dependent PL spectra had an asymmetrical shape and were fitted using Split Pearson VII function,<sup>31</sup> with the fittings also shown in Fig. 4(a). The laser power used for temperature dependent measurements ( $T = 303\text{--}723 \text{ K}$ ) was  $0.42 \text{ mW}$ . Although the asymmetrical A exciton peak can be observed in the whole temperature range, with increasing temperature the peak intensity was seen to decrease in contrast to ref. 16 and 17, whilst the peak position was seen to red-shift and the FWHM to broaden. The temperature dependence of the A exciton peak position is linear with  $dE_{\text{max}}/dT = -0.358 \pm 0.003 \text{ meV K}^{-1}$  (Fig. 4(b)).

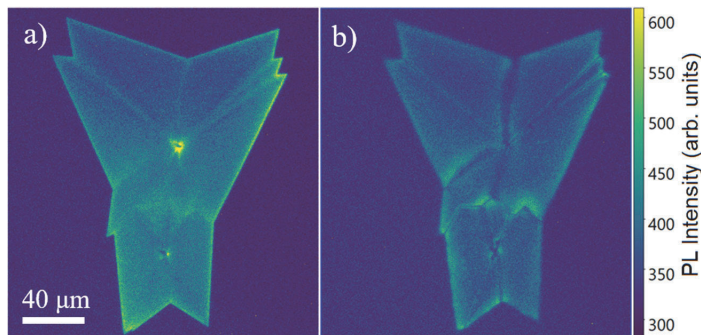


Fig. 2 PL images of the same flake before (a) and after (b) heating the sample up to  $T = 643 \text{ K}$ . Cracking can be observed at the grain boundaries.

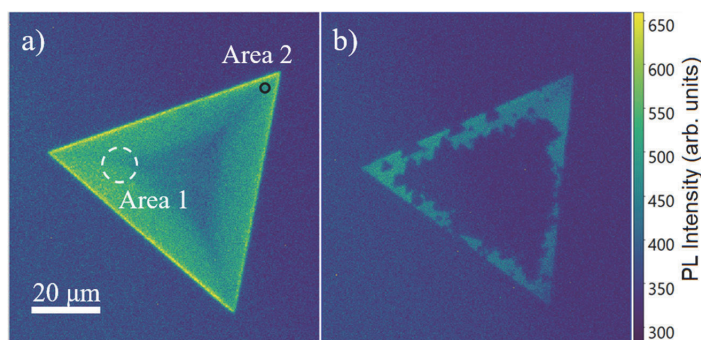


Fig. 3 PL images of the same flake before (a) and after (b) it was used to study temperature dependent PL at elevated temperatures. Area 1 and area 2 are representing the approximate laser spot size and placement of 10× objective and 50× objective, respectively.

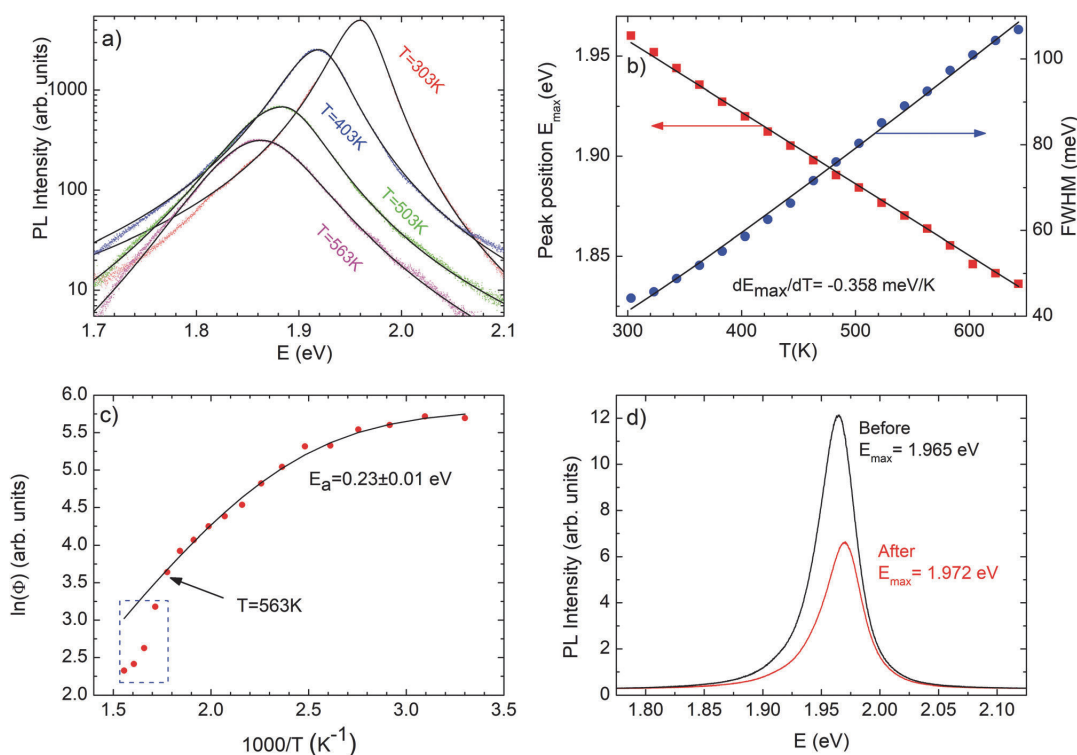


Fig. 4 (a) Temperature dependent PL spectra of  $\text{WS}_2$  monolayer. PL fitting using Split-Pearson-VII function are shown as black lines. (b) Temperature dependence of exciton peak energy (red dots) and FWHM of the exciton peak (blue dots). The exciton peak energy dependence is fitted with linear and FWHM dependence is a result of fitting with eqn (1). (c) Arrhenius style plot showing the thermal activation energy of the A exciton peak. Fitting result using eqn (2) is given as a continuous line. Blue rectangle is showing the additional intensity decrease due to material decomposition. (d) Room temperature PL spectra from area 2 of Fig. 3(a) on the flake before and after heating up to  $T = 723$  K.

Next, the temperature dependence of the full-width at half-maximum (FWHM) was fitted using the relation proposed by Rudin *et al.*<sup>32</sup> given as

$$\text{FWHM}(T) = W_0 + \beta T + \gamma / [\exp(\hbar\omega_{\text{LO}}/kT) - 1] \quad (1)$$

where  $W_0$  is the width at  $T = 0$  K including also inhomogeneous broadening,  $\beta$  is a coefficient for the interaction of excitons with acoustic phonons and the last term represents the interaction with LO (longitudinal optical) phonons,  $\hbar\omega_{\text{LO}}$  is the LO-phonon energy and is taken to be equal to 44.6 meV for  $\text{WS}_2$ .<sup>33</sup>

The interaction with acoustic phonons was neglected because it is usually very small.<sup>34</sup> The fitting result is presented in Fig. 4(b) and fitting parameters are the following  $W_0 = 16.5 \pm 0.8$  meV and  $\gamma = 113.9 \pm 1.6$  meV. The FWHM of the exciton peak increases in the whole temperature range due to interaction with LO phonons.

Subsequently, the thermal activation energy of WS<sub>2</sub> exciton emission was found to be  $E_a = 0.23 \pm 0.01$  eV (Fig. 4(c)), as was determined using the following equation:<sup>35</sup>

$$\Phi(T) = \Phi_0 / \left( 1 + a e^{-\frac{E_a}{kT}} \right) \quad (2)$$

where  $\Phi$  is the integral intensity of the PL band,  $a$  is the process rate parameter and  $E_a$  is the thermal activation energy. Thermal quenching of exciton emission is probably related to activation of non-radiative recombination.<sup>22,36</sup> For the calculation of the thermal activation energy temperatures up to  $T = 563$  K were involved, because when the temperature was higher than  $T = 563$  K we noticed an additional drop of PL intensity due to decomposition of the WS<sub>2</sub> monolayer (marked with the blue rectangle in Fig. 4(c)). Similar activation energies have been found in WS<sub>2</sub> grown on Si/SiO<sub>2</sub> ( $E_a = 0.40$  eV<sup>22</sup> and  $E_a = 0.53$  eV<sup>36</sup>) and on sapphire ( $E_a = 0.20$  eV).<sup>22</sup>

Room temperature PL was measured before and after heating (up to  $T = 723$  K) from area 2 (see Fig. 3(a)), a region that had not undergone apparent thermal decomposition. The results are presented in Fig. 4(d). The PL intensity at room temperature following the high temperature measurements remained in a similar range as before although the intensity has reduced by about a factor of two. This indicates that the remaining WS<sub>2</sub> monolayer is stable against temperature variations and largely maintains its previous properties, suggesting that the temperature does not have some irreversible effect on the monolayer that remains. The Raman spectrum from the same area after heating up to  $T = 723$  K shows a peak separation of  $\Delta = 61.9$  cm<sup>-1</sup> and the shape of the spectrum remained the same, confirming that the quality of remaining monolayer is maintained. Additionally, reflectance contrast measurements can be also used to further study the quality of WS<sub>2</sub> monolayer. It is known that the absorption spectrum is directly related to the reflectance contrast spectrum:<sup>37</sup>

$$\frac{\Delta R}{R}(E) = \frac{R_L - R_S}{R_S} = \frac{4}{n_s^2 - 1} \alpha(E) \quad (3)$$

where  $R_L$  is a reflected light from the monolayer,  $R_S$  is a reflected light from the SiO<sub>2</sub> substrate layer,  $n_s$  is the index of refraction of the SiO<sub>2</sub> layer and  $\alpha$  is the absorption of the sample. RC spectra measured before and after heating ( $T = 723$  K) are presented in Fig. 5. It can be seen that the shape and intensity of A and B exciton bands remain relatively unchanged after thermal treatment.

From Fig. 3(b) it seems that the remaining WS<sub>2</sub> monolayer is concentrated near the edges of a triangle. It is also interesting to note that this part of the flake exhibited a greater room temperature PL intensity compared to the central part of the monolayer. This means that the central part of the triangle, that has lower PL intensity, is also degrading faster at high temperatures than the brighter part of the flake. It may be that

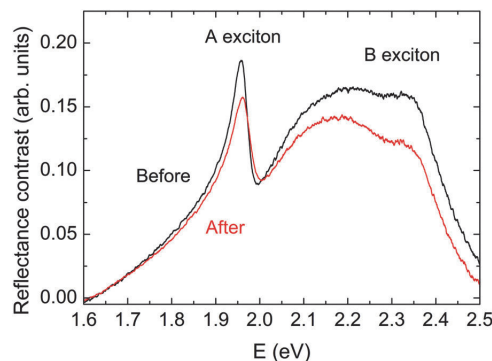


Fig. 5 Room temperature RC spectra from WS<sub>2</sub> flake before and after heating up to  $T = 723$  K.

the middle area of the triangle has more defects, which are non-radiative<sup>13</sup> and that this is the reason for material loss. Moreover, our measurements showed that the PL band from the middle area of the as-grown flake was also red shifted about 4 meV when compared to the edge region of the flake. This red shift of the exciton band in CVD grown monolayers is related to the slightly higher value of tensile strain.<sup>10,26</sup> It is possible that the increased strain is also playing an essential role in more rapid thermal decomposition of the central part of the flake. This is further corroborated by the polycrystalline flake (Fig. 2), which has the most significant material loss starting at the grain boundaries, although this flake was exposed to even lower temperatures ( $T = 643$  K). However, the remaining monolayer does also include some areas of material loss that also exhibit a triangular shape. These triangular holes are probably related to point defects. The intrinsic defects in as-grown MoS<sub>2</sub>, including grain boundaries and point defects, as starting points for degradation are discussed also in ref. 38. Specifically, areas with higher defect density have larger concentrations of dangling bonds and consequently greater reactivity. Moreover, the authors noticed that triangular holes due to point defects have opposite orientation to the parent crystal. This can also be observed in our case (see Fig. 3(b)). The PL peak position after high temperature handling had a small blue-shift of 7 meV, which may be related to strain release,<sup>10</sup> as the material loss and geometry change of the flake can affect the strain inside the flake. The same small blue-shift of the A-exciton can be observed also in the RC spectrum after high-temperature handling, see Fig. 5.

It is also noteworthy that whilst the first apparent material loss was detected in the optical image at  $T = 603$  K, it is evident from the spectroscopy data that initial degradation begins at around  $T = 563$  K. The intensive material loss after high temperature treatment is visible in Fig. 3(b), in which only some areas of the original triangle are still present.

AFM was used to further study the intact monolayer, with the results presented in Fig. 6. The height and phase scans (Fig. 6(a and b) respectively) show that the holes inside the material are indeed of triangular shape. Furthermore, the inside of the triangle (right side of the Fig. 6(a)) includes areas with

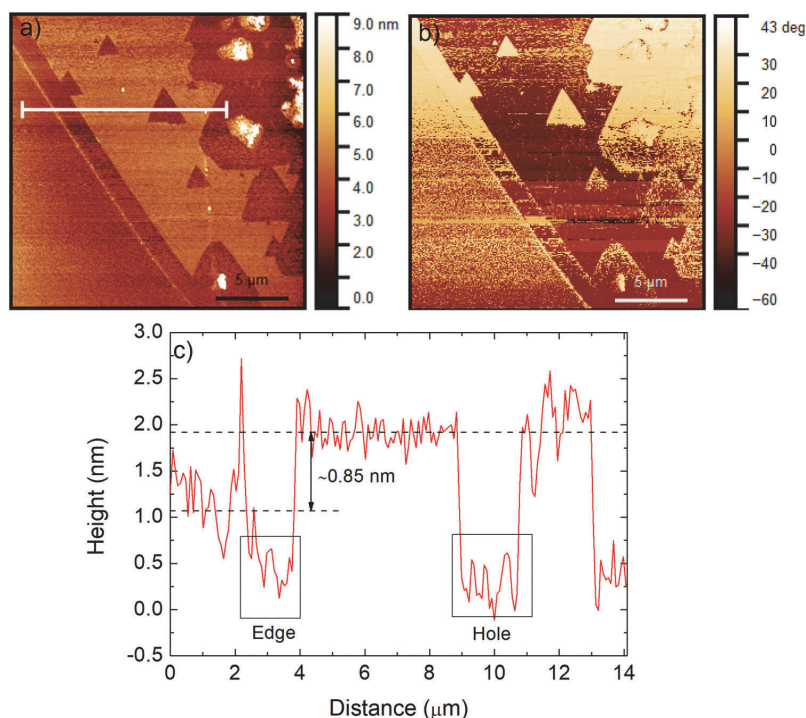


Fig. 6 AFM height (a) and phase (b) image of the studied flake edge after high temperature measurements up to  $T = 723$  K. Line profile (c) is presented in red color (white line from Fig. 6(a)).

large aggregations of material. According to the phase image, these regions are not crystalline  $\text{WS}_2$ , a finding that is further confirmed by Fig. 3(b), as these regions are not seen to emit PL. As such, they may be collections of amorphous material, which consist of decomposed  $\text{WS}_2$  monolayer remnants.

A second change that can be observed from the AFM results is that the  $\text{WS}_2$  monolayer edge has been shifted, whilst there is also a very thin line marking the former edge visible in Fig. 6. Although this shift of the edge is only by about  $1 \mu\text{m}$ , it is still noticeable in Fig. 3, where the size of the triangle is smaller after high temperature measurements. The treatment also seems to have had some effect on the underlying substrate ( $\text{SiO}_2$ ), as evidenced from the black rectangle marked edge in Fig. 6(c). Here, part of the underlying  $\text{SiO}_2$  between the original and new  $\text{WS}_2$  appears to have been eroded. Although we note that an imaging artifact cannot be ruled out, this apparent substrate degradation is also present in the eroded regions within the remaining monolayer (black rectangle marked as hole in Fig. 6(c)). In turn, one possible reason for the shift of the edge may be due to a higher concentration of defects on the edge, as was discussed previously. The intrinsic defects can be located in grain boundaries or at edges, or be present as local point defects and are the starting point for the degradation.

As stated earlier, contradictory reports can also be found regarding the high-temperature photoluminescent response of

other TMDs, such as  $\text{MoS}_2$ . Many of the monolayered TMD materials (including  $\text{MoS}_2$ ) have similar structures and properties to  $\text{WS}_2$ , and similar general trends to those found here could be tentatively expected in such cases. However, we note that the individual materials are distinct, and it is difficult to predict with certainty the behavior of these other systems without further measurements.

## Conclusion

In this report we have detailed the changes in the excitonic emission of monolayer  $\text{WS}_2$  induced by high temperature, as well as described the degradation induced and the extent of recovery upon a return to room temperature. Rather than seeing a transient or consistent enhancement in PL intensity upon raising the temperature, our measurements in a controlled environment show a standard and continuous decrease in intensity. This is allied to a near linear decrease in peak position and to an increase in peak width, and is considered to result from exciton interaction with optical phonons.

We also note degradation of parts of the monolayer following the handling at elevated temperatures, whilst other parts largely maintain their original properties, such as position and shape of Raman peaks and PL intensity. The irreversible changes at high

temperature were first established by an additional reduction in PL intensity prior to any changes being visible in the appearance of the monolayer. Moreover, there is an apparent relation between the areas of lower initial room temperature PL intensity in the center of the flake and the degree of material loss from the monolayer. Additionally, the symmetry of the holes detected in the remaining monolayer by AFM may point to a defect induced mechanism, suggesting that a higher density of defects in the flake center may be responsible for both the weaker PL intensity and enhanced rate of degradation. However, this paints an incomplete picture given the additional loss of material from the very edge of the flake, which shows very high relative PL intensity at room temperature. Hence, further investigations are needed to deepen the understanding of temperature-induced degradation mechanisms. Beyond this, our work can also be extended to look at the role of other micro or macroscopic parameters, such as stoichiometry, flake shape, or substrate, on the high-temperature photo-response of 2D TMDs.

## Conflicts of interest

There are no conflicts to declare.

## Acknowledgements

This work has been supported by the European Regional Development Fund, Project TK141. L. M., A. M., E. P., and M. S. gratefully acknowledge support from DFG by funding SCHL 384/20-1 (project number 406129719).

## References

- W. Choi, N. Choudhary, G. H. Han, J. Park, D. Akinwande and Y. H. Lee, *Mater. Today*, 2017, **20**, 116–130.
- D. Akinwande, N. Petrone and J. Hone, *Nat. Commun.*, 2014, **5**, 5678.
- H. Li, Z. Yin, Q. He, H. Li, X. Huang, G. Lu, D. W. H. Fam, A. I. Y. Tok, Q. Zhang and H. Zhang, *Small*, 2012, **8**, 63–67.
- G. H. Lee, Y. J. Yu, X. Cui, N. Petrone, C. H. Lee, M. S. Choi, D. Y. Lee, C. Lee, W. J. Yoo, K. Watanabe, T. Taniguchi, C. Nuckolls, P. Kim and J. Hone, *ACS Nano*, 2013, **7**, 7931–7936.
- Y. Liu, Y. Gao, S. Zhang, J. He, J. Yu and Z. Liu, *Nano Res.*, 2019, **12**, 2695–2711.
- H. Wang, C. Zhang, W. Chan, S. Tiwari and F. Rana, *Nat. Commun.*, 2015, **6**, 6–11.
- J. Gusakova, X. Wang, L. L. Shiau, A. Krivosheeva, V. Shaposhnikov, V. Borisenko, V. Gusakov and B. K. Tay, *Phys. Status Solidi*, 2017, **214**, 1700218.
- H. R. Gutiérrez, N. Perea-López, A. L. Elías, A. Berkdemir, B. Wang, R. Lv, F. López-Urías, V. H. Crespi, H. Terrones and M. Terrones, *Nano Lett.*, 2013, **13**, 3447–3454.
- I. Paradisianos, N. Pliatsikas, P. Patsalas, C. Fotakis, E. Kymakis, G. Kioseoglou and E. Stratakis, *Nanoscale*, 2016, **8**, 16197–16203.
- Y. Wang, C. Cong, W. Yang, J. Shang, N. Peimyoo, Y. Chen, J. Kang, J. Wang, W. Huang and T. Yu, *Nano Res.*, 2015, **8**, 2562–2572.
- J. Krustok, R. Kaupmees, R. Jaaniso, V. Kiisk, I. Sildos, B. Li and Y. Gong, *AIP Adv.*, 2017, **7**, 065005.
- K. M. McCreary, A. T. Hanbicki, S. Singh, R. K. Kawakami, G. G. Jernigan, M. Ishigami, A. Ng, T. H. Brintlinger, R. M. Stroud and B. T. Jonker, *Sci. Rep.*, 2016, **6**, 1–10.
- M. R. Rosenberger, H. J. Chuang, K. M. McCreary, C. H. Li and B. T. Jonker, *ACS Nano*, 2018, **12**, 1793–1800.
- H. Liu, J. Lu, K. Ho, Z. Hu, Z. Dang, A. Carvalho, H. R. Tan, E. S. Tok and C. H. Sow, *Nano Lett.*, 2016, **16**, 5559–5567.
- A. T. Hanbicki, M. Currie, G. Kioseoglou, A. L. Friedman and B. T. Jonker, *Solid State Commun.*, 2015, **203**, 16–20.
- Y. Li, W. Liu, H. Xu, C. Zhang, L. Yang, W. Yue and Y. Liu, *J. Mater. Chem. C*, 2016, **4**, 9187–9196.
- Y. Chen, W. Wen, Y. Zhu, N. Mao, Q. Feng, M. Zhang, H. P. Hsu, J. Zhang, Y. S. Huang and L. Xie, *Nanotechnology*, 2016, **27**, 445705.
- P. J. Ko, A. Abderrahmane, T. V. Thu, D. Ortega, T. Takamura and A. Sandhu, *J. Nanosci. Nanotechnol.*, 2015, **15**, 6843–6846.
- S. Zhu, D. Li, Y. Hu, J. Wang, X. Wang and W. Lu, *Mater. Res. Express*, 2018, **5**, 066209.
- H. Chen, Y. Li, W. Liu, H. Xu, G. Yang, J. Shi, Q. Feng, T. Yu, X. Liu and Y. Liu, *Nanoscale Horiz.*, 2018, **3**, 598–605.
- A. P. S. Gaur, S. Sahoo, J. F. Scott and R. S. Katiyar, *J. Phys. Chem. C*, 2015, **119**, 5146–5151.
- L. Su, Y. Yu, L. Cao and Y. Zhang, *Nano Res.*, 2015, **8**, 2686–2697.
- Z. Hu, Y. Bao, Z. Li, Y. Gong, R. Feng, Y. Xiao, X. Wu, Z. Zhang, X. Zhu, P. M. Ajayan and Z. Fang, *Sci. Bull.*, 2017, **62**, 16–21.
- G. Ye, Y. Gong, J. Lin, B. Li, Y. He, S. T. Pantelides, W. Zhou, R. Vajtai and P. M. Ajayan, *Nano Lett.*, 2016, **16**, 1097–1103.
- K. Yao, J. D. Femi-Oyetero, S. Yao, Y. Jiang, L. El Bouanani, D. C. Jones, P. A. Ecton, U. Philipose, M. El Bouanani, B. Rout, A. Neogi and J. M. Perez, *2D Mater.*, 2020, **7**, 015024.
- R. Kaupmees, M. Grossberg, M. Ney, A. Asaithambi, A. Lorke and J. Krustok, *Phys. Status Solidi RRL*, 2020, **14**, 1–6.
- K. M. McCreary, A. T. Hanbicki, G. G. Jernigan, J. C. Culbertson and B. T. Jonker, *Sci. Rep.*, 2016, **6**, 19159.
- Y. Zhang, Y. Zhang, Q. Ji, J. Ju, H. Yuan, J. Shi, T. Gao, D. Ma, M. Liu, Y. Chen, X. Song, H. Y. Hwang, Y. Cui and Z. Liu, *ACS Nano*, 2013, **7**, 8963–8971.
- A. Berkdemir, H. R. Gutiérrez, A. R. Botello-Méndez, N. Perea-López, A. L. Elías, C. I. Chia, B. Wang, V. H. Crespi, F. López-Urías, J. C. Charlier, H. Terrones and M. Terrones, *Sci. Rep.*, 2013, **3**, 1–8.
- E. Pollmann, L. Madauf, V. Zeuner and M. Schleberger, *Encyclopedia of Interfacial Chemistry: Surface Science and Electrochemistry*, 2018, **3**, 338–343.
- D. Balzar, *J. Res. Natl. Inst. Stand. Technol.*, 1993, **98**, 321.
- S. Rudin, T. L. Reinecke and B. Segall, *Phys. Rev. B: Condens. Matter Mater. Phys.*, 1990, **41**, 3017–3027.
- A. Molina-Sánchez and L. Wirtz, *Phys. Rev. B: Condens. Matter Mater. Phys.*, 2011, **84**, 1–8.



- 34 S. Helmrich, R. Schneider, A. W. Achtstein, A. Arora, B. Herzog, S. M. de Vasconcellos, M. Kolarczik, O. Schöps, R. Bratschitsch, U. Woggon and N. Owschimikow, *2D Mater.*, 2018, **5**, 045007.
- 35 J. Krustok, H. Collan and K. Hjelt, *J. Appl. Phys.*, 1997, **81**, 1442–1445.
- 36 N. Peimyoo, J. Shang, C. Cong, X. Shen, X. Wu, E. K. L. Yeow and T. Yu, *ACS Nano*, 2013, **7**, 10985–10994.
- 37 K. F. Mak, M. Y. Sfeir, Y. Wu, C. H. Lui, J. A. Misewich and T. F. Heinz, *Phys. Rev. Lett.*, 2008, **101**, 196405.
- 38 X. Chen, S. M. Shinde, K. P. Dhakal, S. W. Lee, H. Kim, Z. Lee and J. H. Ahn, *NPG Asia Mater.*, 2018, **10**, 810–820.

# Curriculum vitae

## Personal data

Name: Reelika Kaupmees  
Date of birth: 04.12.1992  
Place of birth: Tallinn, Estonia  
Citizenship: Estonian

## Contact data

E-mail: reelika.kaupmees@taltech.ee

## Education

2017–2021 Tallinn University of Technology – PhD  
2015–2017 Tallinn University of Technology – MSc, *Cum Laude*  
2012–2015 Tallinn University of Technology – BSc, *Cum Laude*  
2000–2012 Tallinn German Gymnasium – Secondary School, Silver Medal

## Language competence

Estonian Native  
English Fluent  
German Fluent  
Russian Beginner

## Professional employment

2020–2021 Early stage researcher at laboratory of optoelectronic materials physics, Tallinn University of Technology  
2017–2019 Early stage researcher at laboratory of optoelectronic materials physics, Tallinn University of Technology

## Conferences and training courses

09.10.2017 Conference “Progress in photovoltaics in Denmark 2017”, Roskilde, Denmark  
10.10.–13.10.2017 Summer school “Advanced concepts in photovoltaics”, Roskilde, Denmark (oral presentation)  
07.03.–08.03.2018 Scientific conference, Graduate school Functional materials and technologies (GSFMT), Tallinn, Estonia (poster presentation)  
18.06.–22.06.2018 European materials research society (E-MRS) Spring Meeting, Strasbourg, France (poster presentation)  
04.02.–05.02.2019 Scientific conference, Graduate school of Functional materials and technologies (GSFMT), Tartu, Estonia (oral presentation)  
18.03.–22.03.2019 Research visit at University of Duisburg-Essen, Duisburg, Germany  
27.05.–31.05.2019 European materials research society (E-MRS) Spring Meeting, Nice, France (poster presentation)  
04.02.–05.02.2020 Scientific conference, Graduate school “Functional materials and technologies (GSFMT)”, Tallinn, Estonia (poster presentation)

## Awards

- 2017 II prize in National contest for university students on scientific research in the category of master studies, natural sciences and engineering

## Supervised dissertation

Birkan Emrem, Master's Degree, 2019, (sup) Jüri Krustok; Reelika Kaupmees, Phonon properties of  $\text{Cu}_2(\text{Zn,Fe})\text{SnS}_4$  solid solutions, Tallinn University of Technology School of Science, Department of Cybernetics.

## Defended dissertation

Master's Degree (2017), supervisor: Jüri Krustok, Local strain-induced band gap fluctuations and exciton localization in aged  $\text{WS}_2$  monolayers, Tallinn University of Technology School of Science, Department of Cybernetics.

## Publications

1. Krustok, J.; Kondrotas, R.; Nedzinskas, R.; Timmo, K.; **Kaupmees, R.**; Mikli, V.; Grossberg, M. (in press) Identification of Excitons and Biexcitons in  $\text{Sb}_2\text{Se}_3$  Under High Photoluminescence Excitation Density. *Adv. Opt. Mater.* <https://doi.org/10.1002/adom.202100107>
2. Krustok, J.; Raadik, T.; **Kaupmees, R.**; Ghisani, F.; Timmo, K.; Altosaar, M.; Mikli, V.; Grossberg, M. (2021). Broad-band photoluminescence of donor-acceptor pairs in tetrahedrite  $\text{Cu}_{10}\text{Cd}_2\text{Sb}_4\text{S}_{13}$  microcrystals. *Journal of Physics D: Applied Physics*, 54 (10), 105102. DOI: 10.1088/1361-6463/abce29.
3. **Kaupmees, R.**; Grossberg, M.; Ney, M.; Asaithambi, A.; Lorke, A.; Krustok, J. (2020). Tailoring of Bound Exciton Photoluminescence Emission in  $\text{WS}_2$  Monolayers. *Physica Status Solidi (RRL) - Rapid Research Letters*, 14, 1900355.10.1002/pssr.201900355.
4. Grossberg, M.; Volobujeva, O.; Penežko, A.; **Kaupmees, R.**; Raadik, T.; Krustok, J. (2020). Origin of photoluminescence from antimony selenide. *Journal of Alloys and Compounds*, 817, 152716.10.1016/j.jallcom.2019.152716.
5. **Kaupmees, R.**; Walke, P.; Madauß, L.; Maas, A.; Pollmann, E.; Schleberger, M.; Grossberg, M.; Krustok, J. (2020). The effect of elevated temperatures on excitonic emission and degradation processes of  $\text{WS}_2$  monolayers. *Physical Chemistry Chemical Physics*, 22, 22609–22616. DOI: 10.1039/D0CP03248D.
6. **Kaupmees, R.**; Komsa, H.-P.; Krustok, J. (2019). Photoluminescence Study of B-Trions in  $\text{MoS}_2$  Monolayers with High Density of Defects. *Physica Status Solidi (B)*, 256 (3), 1800384.10.1002/pssb.201800384.
7. Spalatu, N.; Hiie, J.; **Kaupmees, R.**; Volobujeva, O.; Krustok, J.; Oja Acik, I.; Krunks, M. (2019). Post-deposition Processing of SnS Thin Films and Solar Cells: Prospective Strategy to Obtain Large, Sintered and Doped SnS Grains by Recrystallization in the Presence of a Metal Halide Flux. *ACS Applied Materials & Interfaces*. DOI: 10.1021/acsami.9b03213.
8. Krustok, J.; Raadik, T.; **Kaupmees, R.**; Grossberg, M.; Kauk-Kuusik, M.; Timmo, K.; Mere, A. (2019). Observation of band gap fluctuations and carrier localization in  $\text{Cu}_2\text{CdGeSe}_4$ . *Journal of Physics D Applied Physics*, 52 (28), 285102.10.1088/1361-6463/ab1afd.

9. Kauk-Kuusik, M.; Li, X.; Pilvet, M.; Timmo, K.; Mikli, V.; **Kaupmees, R.**; Danilson, M.; Grossberg, M. (2019). Nano-scale sulfurization of  $\text{Cu}_2\text{ZnSnSe}_4$  crystal surface for photovoltaic applications. *Journal of Materials Chemistry A*, 7, 24884–24890. DOI: 10.1039/C9TA08020A.
10. Grossberg, M.; Raadik, T.; Krustok, J.; Kauk-Kuusik, M.; Timmo, K.; **Kaupmees, R.**; Mikli, V.; Mere, A. (2018). Optical and structural properties of orthorhombic and tetragonal polymorphs of  $\text{Cu}_2\text{CdGeSe}_4$ . *Thin Solid Films*, 666, 44–47. DOI: 10.1016/j.tsf.2018.09.031.
11. Timmo, K.; Kauk-Kuusik, M.; Pilvet, M.; Altosaar, M.; Grossberg, M.; Danilson, M.; **Kaupmees, R.**; Mikli, V.; Raudoja, J.; Varema, T. (2018).  $\text{Cu}(\text{In,Ga})\text{Se}_2$  monograin powders with different Ga content for solar cells. *Solar Energy*, 176, 648–655. DOI: 10.1016/j.solener.2018.10.078.
12. Krustok, J.; **Kaupmees, R.**; Jaaniso, R.; Kiisk, V.; Sildos, I.; Li, B.; Gong, Y. (2017). Local strain-induced band gap fluctuations and exciton localization in aged  $\text{WS}_2$  monolayers. *AIP Advances*, 7 (6), 065005. DOI: 10.1063/1.4985299.

## Elulookirjeldus

### Isikuandmed

Nimi: Reelika Kaupmees  
Sünniaeg: 04.12.1992  
Sünnikoht: Tallinn, Eesti  
Kodakondsus: eestlane

### Kontaktandmed

E-post: reelika.kaupmees@taltech.ee

### Hariduskäik

2017–2021 Tallinna Tehnikaülikool – PhD  
2015–2017 Tallinna Tehnikaülikool – MSc, *Cum Laude*  
2012–2015 Tallinna Tehnikaülikool – BSc, *Cum Laude*  
2000–2012 Tallinna Saksa Gümnaasium – Keskkharidus, Hõbemedal

### Keelteoskus

Eesti keel Emakeel  
Inglise keel Kõrgtase  
Saksa keel Kõrgtase  
Vene keel Algtase

### Teenistuskäik

2020–2021 doktorant-nooremteadur optoeletronsete materjalide füüsika laboris, Tallinna Tehnikaülikool  
2017–2019 doktorant-nooremteadur optoeletronsete materjalide füüsika laboris, Tallinna Tehnikaülikool

### Konverentsid ja täiendkoursused

09.10.2017 Konverents “Progress in photovoltaics in Denmark 2017”, Roskilde, Taani  
10.10.–13.10.2017 Suvekool “Advanced concepts in photovoltaics” Roskilde, Taani (suuline ettekanne)  
07.03.–08.03.2018 Teaduskonverents Funktsionaalsete materjalide ja tehnoloogiate doktorikool, Tallinn, Eesti (poster ettekanne)  
18.06.–22.06.2018 European materials research society (E-MRS) Spring Meeting, Strasbourg, Prantsusmaa (poster ettekanne)  
04.02.–05.02.2019 Teaduskonverents Funktsionaalsete materjalide ja tehnoloogiate doktorikool, Tartu, Eesti (suuline ettekanne)  
18.03.–22.03.2019 Teadustegevus Duisburg-Esseni Ülikoolis, Duisburg, Saksamaa  
27.05.–31.05.2019 European materials research society (E-MRS) Spring Meeting, Nice, Prantsusmaa (poster ettekanne)  
04.02.–05.02.2020 Teaduskonverents Funktsionaalsete materjalide ja tehnoloogiate doktorikool, Tallinn, Eesti (poster ettekanne)

### Tunnustused

2017 II prize in National contest for university students on scientific research in the category of master studies, natural sciences and engineering

## Juhendatud väitekirjad

Birkan Emrem, magistrikraad, 2019, (juhendajad) Jüri Krustok; Reelika Kaupmees,  $\text{Cu}_2(\text{Zn,Fe})\text{SnS}_4$  tahkete lahuste foonon-omadused, Tallinna Tehnikaülikool, Loodusteaduskond, Küberneetika instituut.

## Kaitsud lõputööd

Magistrikraad (2017), juhendaja: Jüri Krustok, Lokaalsete pingete põhjustatud keelutsooni fluktuatsioonid ja eksitonide lõksustumine vananenud  $\text{WS}_2$  monokihtides, Tallinna Tehnikaülikool, Loodusteaduskond, Küberneetika instituut.

## Publikatsioonid

1. Krustok, J.; Kondrotas, R.; Nedzinskas, R.; Timmo, K.; **Kaupmees, R.**; Mikli, V.; Grossberg, M. (in press) Identification of Excitons and Biexcitons in  $\text{Sb}_2\text{Se}_3$  Under High Photoluminescence Excitation Density. *Adv. Opt. Mater.* <https://doi.org/10.1002/adom.202100107>
2. Krustok, J.; Raadik, T.; **Kaupmees, R.**; Ghisani, F.; Timmo, K.; Altosaar, M.; Mikli, V.; Grossberg, M. (2021). Broad-band photoluminescence of donor-acceptor pairs in tetrahedrite  $\text{Cu}_{10}\text{Cd}_2\text{Sb}_4\text{S}_{13}$  microcrystals. *Journal of Physics D: Applied Physics*, 54 (10), 105102. DOI: 10.1088/1361-6463/abce29.
3. **Kaupmees, R.**; Grossberg, M.; Ney, M.; Asaithambi, A.; Lorke, A.; Krustok, J. (2020). Tailoring of Bound Exciton Photoluminescence Emission in  $\text{WS}_2$  Monolayers. *Physica Status Solidi (RRL) - Rapid Research Letters*, 14, 1900355.10.1002/pssr.201900355.
4. Grossberg, M.; Volobujeva, O.; Penežko, A.; **Kaupmees, R.**; Raadik, T.; Krustok, J. (2020). Origin of photoluminescence from antimony selenide. *Journal of Alloys and Compounds*, 817, 152716.10.1016/j.jallcom.2019.152716.
5. **Kaupmees, R.**; Walke, P.; Madauß, L.; Maas, A.; Pollmann, E.; Schleberger, M.; Grossberg, M.; Krustok, J. (2020). The effect of elevated temperatures on excitonic emission and degradation processes of  $\text{WS}_2$  monolayers. *Physical Chemistry Chemical Physics*, 22, 22609–22616. DOI: 10.1039/D0CP03248D.
6. **Kaupmees, R.**; Komsa, H.-P.; Krustok, J. (2019). Photoluminescence Study of B-Trions in  $\text{MoS}_2$  Monolayers with High Density of Defects. *Physica Status Solidi (B)*, 256 (3), 1800384.10.1002/pssb.201800384.
7. Spalatu, N.; Hiie, J.; **Kaupmees, R.**; Volobujeva, O.; Krustok, J.; Oja Acik, I.; Krunks, M. (2019). Post-deposition Processing of SnS Thin Films and Solar Cells: Prospective Strategy to Obtain Large, Sintered and Doped SnS Grains by Recrystallization in the Presence of a Metal Halide Flux. *ACS Applied Materials & Interfaces*. DOI: 10.1021/acsami.9b03213.
8. Krustok, J.; Raadik, T.; **Kaupmees, R.**; Grossberg, M.; Kauk-Kuusik, M.; Timmo, K.; Mere, A. (2019). Observation of band gap fluctuations and carrier localization in  $\text{Cu}_2\text{CdGeSe}_4$ . *Journal of Physics D Applied Physics*, 52 (28), 285102.10.1088/1361-6463/ab1afd.
9. Kauk-Kuusik, M.; Li, X.; Pilvet, M.; Timmo, K.; Mikli, V.; **Kaupmees, R.**; Danilson, M.; Grossberg, M. (2019). Nano-scale sulfurization of  $\text{Cu}_2\text{ZnSnSe}_4$  crystal surface for photovoltaic applications. *Journal of Materials Chemistry A*, 7, 24884–24890.10.1039/C9TA08020A.
10. Grossberg, M.; Raadik, T.; Krustok, J.; Kauk-Kuusik, M.; Timmo, K.; **Kaupmees, R.**; Mikli, V.; Mere, A. (2018). Optical and structural properties of orthorhombic and tetragonal polymorphs of  $\text{Cu}_2\text{CdGeSe}_4$ . *Thin Solid Films*, 666, 44–47. DOI: 10.1016/j.tsf.2018.09.031.

11. Timmo, K.; Kauk-Kuusik, M.; Pilvet, M.; Altosaar, M.; Grossberg, M.; Danilson, M.; **Kaupmees, R.**; Mikli, V.; Raudoja, J.; Varema, T. (2018). Cu(In,Ga)Se<sub>2</sub> monograin powders with different Ga content for solar cells. *Solar Energy*, 176, 648–655. [10.1016/j.solener.2018.10.078](https://doi.org/10.1016/j.solener.2018.10.078).
12. Krustok, J.; **Kaupmees, R.**; Jaaniso, R.; Kiisk, V.; Sildos, I.; Li, B.; Gong, Y. (2017). Local strain-induced band gap fluctuations and exciton localization in aged WS<sub>2</sub> monolayers. *AIP Advances*, 7 (6), 065005. DOI: [10.1063/1.4985299](https://doi.org/10.1063/1.4985299).

ISSN 2585-6901 (PDF)  
ISBN 978-9949-83-696-3 (PDF)